2020

FUNDAMENTAL UNDERSTANDING AND APPLICATIONS OF NANOEMULSIONS FOR ULTRASENSITIVE ELECTROCHEMICAL ANALYSIS

Shashika Gunathilaka Sabaragamuwe Jayasundarakorale
University of Rhode Island, shashikag@my.uri.edu

FUNDAMENTAL UNDERSTANDING AND APPLICATIONS OF NANOEMULSIONS FOR ULTRASENSITIVE ELECTROCHEMICAL ANALYSIS

BY

SHASHIKA GUNATHILAKA SABARAGAMUWE JAYASUNDARA KORALE

A THESIS SUBMITTED IN PARTIAL FULFILLMENT OF THE

REQUIREMENTS FOR THE DEGREE OF

MASTER OF SCIENCE

IN

CHEMISTRY

UNIVERSITY OF RHODE ISLAND

2020

MASTER OF SCIENCE

OF

SHASHIKA GUNATHILAKA SABARAGAMUWE JAYASUNDARA KORALE

Thesis Committee:

Major Professor Jiyeon Kim

Dugan Hayes

Bonsup Cho

Daniel Roxbury

Nasser H. Zawia

DEAN OF THE GRADUATE SCHOOL

UNIVERSITY OF RHODE ISLAND

2020

ABSTRACT

We demonstrate a new electroanalytical approach for the ultrasensitive electrochemical analysis using nanoemulsions (NEs) uniquely combined with single entity electrochemistry (SEE). First, we investigate the relationship between the structure and relevant electrochemical activity of NEs. We employ SEE to elucidate the interfacial structure of NEs and their corresponding electrochemical activities, which cannot be unequivocally defined by general microscopic techniques. Throughout this work on nanostructural effect of NEs, we could optimize the most suitable composition of NEs, showing facile electron transfer kinetics across the NE interface as well as a high monodispersity. Particularly, the application of SEE for optimized NEs allowed us to in-situ measure the partition coefficient at intact NEs. Although partition coefficient for NEs is a critical physicochemical property determining the uptake of delivery compounds, it has never been explicitly measured by existing ex-situ analytical techniques with intact NEs. Herein, we employ SEE to directly study the partitioned 2-aminobiphenyl (2-ABP) from aqueous bulk media into NEs. The direct electrolysis of 2-ABP in each NE enables us to in situ quantitatively measure the partition coefficient at intact NEs. Our study revealed an unprecedentedly large partition coefficient of 1.9 (± 1.4) × 10^{10} implying intermolecular interaction as well as the thermodynamic distribution, which was validated by molecular simulations. Based on the fundamental understanding of NEs, we finally demonstrated a new electrochemical method for ultra-trace level analysis by combining SEE and NEs. Innovatively, this approach enables to in situ separate, preconcentrate, and even detect analytes with a simple instrumentation. Using ferrocenemethanol (FcMeOH) as

model analytes, we successfully established our method, where FcMeOH partitioned from water, and preconcentrated in each NE was quantitatively analyzed by SEE. Notably, the extraction is efficient to reach about 8 orders of magnitude of preconcentration factor under the true equilibrium, thus leading to a detection limit of 0.2 ppb. Our approach is readily applicable to investigate other aromatic toxicants dissolved in the water, thereby showing a broad applicability for ubiquitous aromatic contaminants and offering great prospects as a sensor for environmental applications.

ACKNOWLEDGMENTS

First and foremost, I would like to convey my deepest gratitude and appreciation to my research supervisor Prof. Jiyeon Kim with great respect for her immense support, guidance, and encouragement in every step of this study. I could not have imagined having a better advisor and mentor for my master's study. Thank you very much for your valuable time, co-operation and generosity which made this work possible as it is till the end.

I would also like to thank my wonderful master's committee members Prof. Dugan Hayes, Prof. Bonsup Cho and Prof. Daniel Roxbury and I am truly grateful to the chair and all the professors of the department chemistry who helped me in numerous ways. I am also thankful to Surendra, Hiranya, Subhashini, and Dylan for their great help and support during this journey. Further, I would like to thank everyone outside my lab who helped me with instruments throughout the past three year.

Finally, I would like to express my very profound gratitude to my parents, my sister and my fiancée Isuri Dammulla for providing me with unfailing support and encouragement throughout my years of study.

PREFACE

This thesis is presented in manuscript format according to the guidelines of the graduate school of the University of Rhode Island.

Chapter 1 published in *ACS Analytical Chemistry* with authors Shashika Sabaragamuwe, Dylan Conti, Surendra Puri, Irene Andrew, and Jiyeon Kim.

Chapter 2 submitted and under review in *ACS Analytical Chemistry* with Authors Hiranya Madawala, Shashika Sabaragamuwe, and Jiyeon Kim.

Chapter 3 submitted and under review in *Analytica Chimica Acta* with Authors Shashika Sabaragamuwe, Hiranya Madawala, Surendra Puri, and Jiyeon Kim.

TABLE OF CONTENTS

LIST OF FIGURES

Chapter 2

Figure number **Page**

Chapter 3

Figure number Page

Chapter 4

Figure number **Page**

Appendix 1

Figure number **Page**

Appendix 2

Figure number **Page**

Appendix 3

Figure number **Page**

LIST OF TABLES

Table **Page**

CHAPTER 01

INTRODUCTION

Fundamental Understanding and Applications of Nanoemulsions for Ultrasensitive Electrochemical Analysis.

Nanoemulsions (NEs) are small oil droplets dispersed in water with mean diameters ranging from 20 to 500 nm, and often stabilized by amphiphilic surfactants.[1] The kinetically stable nature of NEs helps them to retain their size and shape for a long period of time compared to microemulsions.[2] Due to nanometer dimensions, NEs have a high surface area to volume ratio, beneficially leading to a fast mass transfer via 3-dimensional spherical diffusion.[1] Particularly, this fast mass transfer and lipophilic nature endow NEs with a great potential of a delivering vehicle to extract and encapsulate lipophilic compounds from bulk media in an efficient manner.[2] Hence, NEs have emerged as a promising strategy for the efficient delivery of hydrophobic molecules in biomedical analysis, pharmaceutical science, cosmetic and food industry.[1,3-5]

Prior to full utilization of NEs, a profound fundamental understanding about the inner or interfacial-structure, structure-relevant thermodynamic properties and functions of NEs should be prerequisite. For example, the extraction efficiency of NEs depends on an intrinsic partition coefficient of analyte species of interest in the given NE system.[4] This thermodynamic property is determined by inherent chemical structure of NEs.[2] Such a structure-relevant thermodynamic properties, however cannot be unequivocally elucidated by general microscopic approaches, e.g. cryo-transmission electron microscopy,[6] X-ray or neutron scattering.[7] Also, size and polydispersity of NEs play

another vital role in their practical applications. Dynamic light scattering (DLS) method has been widely used to characterize these properties of NEs, which, however, is limited to provide averaged information instead of discrete one of individual NEs.[8] When NEs are used in the analytical approaches, the accuracy and precision in measurements is directly related with the polydispersity and size of NEs. Accordingly, more explicit characterization of discretely distributed properties beyond DLS measurements is necessary for the practical perspectives.

Considering the limitations in currently available techniques and a necessity of profound understanding of fundamentals, we uniquely introduce a single entity electrochemistry (SEE) for the study of NEs. SEE is a modern electrochemical technique enabling to study a single event, e.g., a nano-object at an individual level.[9] In fact, many groups showed successful applications of SEE method in electroanalysis[9] or electrocatalysis[9] by observing collisions of hard particles such as metal nanoparticles or soft particles including vesicle,[10] liposomes,[11] and emulsions[12,13] to a micrometer sized electrode. Bard group and Compton group have lead the application of SEE in emulsion system, whereas their work have been limited to an unpractical system, such as dichloroethane (DCE) droplet.[12,14]

For the first time, we apply SEE to a practically used NE system, i.e., a Pluronic functionalized NE to elucidate the relationship between its interfacial structure and the relevant function. Pluronic based NEs have been utilized for the optical sensing[15] or drug extractors.[16] We will use this NE as a model system in our new electrochemical approach. Pluronic (Poloxamer) is nonionic triblock copolymers composed of a central hydrophobic chain of polyoxypropylene (poly(propylene oxide)) flanked by two hydrophilic chains of polyoxyethylene (poly(ethylene oxide)), and used as surfactants to stabilize NEs. First of all, by varying the amount of Pluronic compounds, we modulate

not only the size but also the interfacial structure of NEs. These two properties, then are experimentally studied by SEE, which enables to scrutinize each NE at an individual level. Correspondingly, Information of discretely distributed size and the valuable implication of interfacial or inner structure of NEs are obtained. Particularly, this single NE approach is more than adequate for our research, because it allows for fast and in-situ measurements of many collisions of individual NEs within a short time, thus attaining quantitative and precise information about the given system.

Secondly, we extend our application of SEE to measure the structure-relevant thermodynamic property, i.e., a partition coefficient of analyte species at intact NEs. A partition coefficient of analytes of interest in NEs is a critical property to determine an uptake of delivery compounds into NEs from environment.[4] Several analytical techniques such as high-performance liquid chromatography (HPLC),[16,17] reverse-phase HPLC,[18] FTIR spectroscopy[17] and UV-Vis spectrophotometry[19] have been commonly used for the measurements of a partition coefficient in NEs. These techniques, however, offer ex-situ and indirect measurements,[16,20] and ambiguously evaluate a partition coefficient. Contrarily, our new application of SEE is capable of in situ and direct measurements at intact NEs at an individual level, thereby promising a highly accurate and precise determination of a partition coefficient.

Finally, based on our new finding of fundamental aspects in the modeled NEs, we develop a new experimental strategy for ultrasensitive analysis of toxicants in water by uniquely combining SEE and NEs. Water is the key element vital for all living organisms on earth. Although earth is mostly covered with oceans, there is only 0.8 % of the total water volume available for use.[21] Unfortunately, human activity and industrialization keep deteriorating this small portion of available water. Specifically, polycyclic aromatic hydrocarbon (PAH) and heavy metals have been identified as a major source of water

pollution.[22,23] These aromatic toxicants are critically harmful to human health due to their carcinogenic nature, and cause severe impacts on the environment and ecosystems even at very low concentration.[23,24] Because of the low solubility of aromatic toxicants in water, they tend to accumulate in sediment, soil and aquatic organisms, finally leading to bioaccumulate in the food chain.[25] Ultimately, it can enter to human bodies via food or water, and cause potential health effects e.g., disruption of pulmonary, gastrointestinal, renal, and dermatologic systems .[26] Further, a long term exposure may cause carcinogenic and mutagenic effects,[27] potentially suppress immune system,[28] and increase a risk of a broad range of cancers.[28-30] Accordingly, a capability of analytical techniques for ultra-trace level detection of aromatic toxicants in water is considered with high significance.

So far, widely accepted techniques such as gas or liquid chromatography coupled with mass spectrometry (MS)[25,31,32] or fluorescence (or UV-Vis) spectroscopy[33] have shown a sufficient sensitivity up to ppm – ppb level. These approaches, however, require high cost resources, i.e. expensive running costs and a skilled operator with laborious and time-consuming work. Thereby, a new experimental strategy with high accessibility as well as ultrahigh sensitivity is significantly demanded.[32]

Herein, we develop a new ultrasensitive analytical method by uniquely combining SEE and NEs, where NEs are employed as an efficient nanoextractor. Notably, our novel approach enables sample separation, preconcentration, and detection in situ. Owing to the fast mass transport at NEs, extremely large partition coefficient of aromatic toxicant in NEs can be fully achieved. This leads to unprecedentedly high preconcentration factors up to 8 orders of magnitudes, thus acquiring a sub ppb level of detection limit. Versatility of this electrochemical approach is further proved by successful detection of another ubiquitous aromatic toxicant in water.

REFERENCES

1. Gupta, A.; Eral, H. B.; Hatton, T. A.; Doyle, P. S., Nanoemulsions: formation, properties and applications. *Soft matter* **2016,** *12* (11), 2826-2841.

2. McClements, D. J., Nanoemulsions versus microemulsions: terminology, differences, and similarities. *Soft matter* **2012,** *8* (6), 1719-1729.

3. Lovelyn, C.; Attama, A. A., Current State of Nanoemulsions in Drug Delivery. *Journal of Biomaterials and Nanobiotechnology* **2011,** *02* (05), 626-639.

4. Lallemand, F.; Daull, P.; Benita, S.; Buggage, R.; Garrigue, J.-S., Successfully improving ocular drug delivery using the cationic nanoemulsion, novasorb. *Journal of drug delivery* **2012,** *2012*.

5. Izquierdo, P.; Esquena, J.; Tadros, T. F.; Dederen, C.; Garcia, M.; Azemar, N.; Solans, C., Formation and stability of nano-emulsions prepared using the phase inversion temperature method. *Langmuir* **2002,** *18* (1), 26-30.

6. Lee, H. S.; Morrison, E. D.; Frethem, C. D.; Zasadzinski, J. A.; McCormick, A. V., Cryogenic electron microscopy study of nanoemulsion formation from microemulsions. *Langmuir* **2014,** *30* (36), 10826-10833.

7. Wilking, J. N.; Chang, C. B.; Fryd, M. M.; Porcar, L.; Mason, T. G., Shear-induced disruption of dense nanoemulsion gels. *Langmuir* **2011,** *27* (9), 5204-5210.

8. Grapentin, C.; Barnert, S.; Schubert, R., Monitoring the stability of perfluorocarbon nanoemulsions by Cryo-TEM image analysis and dynamic light scattering. *PLoS One* **2015,** *10* (6), e0130674.

9. Baker, L. A., Perspective and prospectus on single-entity electrochemistry. *Journal of the American Chemical Society* **2018,** *140* (46), 15549-15559.

10. Lebègue, E.; Anderson, C. M.; Dick, J. E.; Webb, L. J.; Bard, A. J., Electrochemical detection of single phospholipid vesicle collisions at a Pt ultramicroelectrode. *Langmuir* **2015,** *31* (42), 11734-11739.

11. Cheng, W.; Compton, R. G., Investigation of Single-Drug-Encapsulating Liposomes using the Nano-Impact Method. *Angewandte Chemie International Edition* **2014,** *53* (50), 13928-13930.

12. Kim, B. K.; Boika, A.; Kim, J.; Dick, J. E.; Bard, A. J., Characterizing emulsions by observation of single droplet collisions--attoliter electrochemical reactors. *J Am Chem Soc* **2014,** *136* (13), 4849-52.

13. Kim, B.-K.; Kim, J.; Bard, A. J., Electrochemistry of a single attoliter emulsion droplet in collisions. *Journal of the American Chemical Society* **2015,** *137* (6), 2343-2349.

14. Laborda, E.; Molina, A.; Espín, V. F.; Martínez-Ortiz, F.; Garcia de la Torre, J.; Compton, R. G., Single fusion events at polarized liquid–liquid interfaces. *Angewandte Chemie* **2017,** *129* (3), 800-803.

15. Xie, X.; Zhai, J.; Bakker, E., pH independent nano-optode sensors based on exhaustive ion-selective nanospheres. *Analytical chemistry* **2014,** *86* (6), 2853-2856.

16. Varshney, M.; Morey, T. E.; Shah, D. O.; Flint, J. A.; Moudgil, B. M.; Seubert, C. N.; Dennis, D. M., Pluronic microemulsions as nanoreservoirs for extraction of bupivacaine from normal saline. *Journal of the American Chemical Society* **2004,** *126* (16), 5108-5112.

17. Gurpreet, K.; Singh, S., Review of nanoemulsion formulation and characterization techniques. *Indian Journal of Pharmaceutical Sciences* **2018,** *80* (5), 781-789.

18. Singh, K. K.; Vingkar, S. K., Formulation, antimalarial activity and biodistribution of oral lipid nanoemulsion of primaquine. *International Journal of Pharmaceutics* **2008,** *347* (1-2), 136-143.

19. Bhagav, P.; Upadhyay, H.; Chandran, S., Brimonidine tartrate–eudragit long-acting nanoparticles: formulation, optimization, in vitro and in vivo evaluation. *Aaps Pharmscitech* **2011,** *12* (4), 1087-1101.

20. Kontturi, K.; Murtomäki, L., Electrochemical determination of partition coefficients of drugs. *Journal of pharmaceutical sciences* **1992,** *81* (10), 970-975.

21. Revenga, C.; Mock, G., Freshwater biodiversity in crisis. *Earth Trends World Resources Institute* **2000**, 1-4.

22. Manzetti, S., Polycyclic aromatic hydrocarbons in the environment: environmental fate and transformation. *Polycyclic Aromatic Compounds* **2013,** *33* (4), 311-330.

23. Schwarzenbach, R. P.; Egli, T.; Hofstetter, T. B.; Von Gunten, U.; Wehrli, B., Global water pollution and human health. *Annual review of environment and resources* **2010,** *35*, 109-136.

24. Khayatzadeh, J.; Abbasi, E. In *The effects of heavy metals on aquatic animals*, The 1st International Applied Geological Congress, Department of Geology, Islamic Azad University–Mashad Branch, Iran, 2010; pp 26-28.

25. Nieva-Cano, M.; Rubio-Barroso, S.; Santos-Delgado, M., Determination of PAH in food samples by HPLC with fluorimetric detection following sonication extraction without sample clean-up. *Analyst* **2001,** *126* (8), 1326-1331.

26. Pongpiachan, S.; Hattayanone, M.; Pinyakong, O.; Viyakarn, V.; Chavanich, S.; Bo, C.; Khumsup, C.; Kittikoon, I.; Hirunyatrakul, P., Quantitative ecological risk assessment of inhabitants exposed to polycyclic aromatic hydrocarbons in terrestrial soils of King George Island, Antarctica. *Polar Science* **2017,** *11*, 19-29.

27. Jarvis, I. W.; Dreij, K.; Mattsson, Å.; Jernström, B.; Stenius, U., Interactions between polycyclic aromatic hydrocarbons in complex mixtures and implications for cancer risk assessment. *Toxicology* **2014,** *321*, 27-39.

28. Nielsen, T.; Jørgensen, H. E.; Larsen, J. C.; Poulsen, M., City air pollution of polycyclic aromatic hydrocarbons and other mutagens: occurrence, sources and health effects. *Science of the Total Environment* **1996,** *189*, 41-49.

29. Diggs, D. L.; Huderson, A. C.; Harris, K. L.; Myers, J. N.; Banks, L. D.; Rekhadevi, P. V.; Niaz, M. S.; Ramesh, A., Polycyclic aromatic hydrocarbons and digestive tract cancers: a perspective. *Journal of environmental science and health, part c* **2011,** *29* (4), 324-357.

30. Boffetta, P.; Jourenkova, N.; Gustavsson, P., Cancer risk from occupational and environmental exposure to polycyclic aromatic hydrocarbons. *Cancer Causes & Control* **1997,** *8* (3), 444-472.

31. Khalili, N. R.; Scheff, P. A.; Holsen, T. M., PAH source fingerprints for coke ovens, diesel and, gasoline engines, highway tunnels, and wood combustion emissions. *Atmospheric environment* **1995,** *29* (4), 533-542.

32. Aiken, A. C.; DeCarlo, P. F.; Jimenez, J. L., Elemental analysis of organic species with electron ionization high-resolution mass spectrometry. *Analytical Chemistry* **2007,** *79* (21), 8350-8358.

33. Delgado, B.; Pino, V.; Ayala, J. H.; González, V.; Afonso, A. M., Nonionic surfactant mixtures: a new cloud-point extraction approach for the determination of PAHs in seawater using HPLC with fluorimetric detection. *Analytica Chimica Acta* **2004,** *518* (1-2), 165-172.

CHAPTER 2

SINGLE-ENTITY ELECTROCHEMISTRY OF NANOEMULSION: THE NANOSTRUCTURAL EFECT ON ITS ELETROCHEMICAL BEHAVIOUR

Shahsika Gunathilaka Sabaragamuwe[1], Dylan Conti[1], Surendra Raj Puri[1], Irene Andreu[2], Jiyeon Kim[1*]

[1.] Department of chemistry, University of Rhode Island, Kingston, RI, 02881

[2.] RI Consortium of Nanoscience and Nanotechnology, Department of Chemical Engineering, University of Rhode Island, Kingston, RI, 02881

This manuscript has been published in *ACS Analytical Chemistry* journal.

Reprinted with permission from*:*

Single-Entity Electrochemistry of Nanoemulsions: The Nanostructural Effect on Its Electrochemical Behavior. Shahsika Gunathilaka Sabaragamuwe[1], Dylan Conti[1], Surendra Raj Puri[1], Irene Andreu[2], Jiyeon Kim[1]*. *ACS Analytical Chemistry*, *Volume 250*, 1 July 2019, Pages 9599-9607

SINGLE-ENTITY ELECTROCHEMISTRY OF NANOEMULSION: THE NANOSTRUCTURAL EFECT ON ITS ELETROCHEMICAL BEHAVIOUR

Shahsika Gunathilaka Sabaragamuwe[1], Dylan Conti[1], Surendra Raj Puri[1], Irene Andreu[2], Jiyeon Kim[1*]

[1.] Department of chemistry, University of Rhode Island, Kingston, RI, 02881

[2.] RI Consortium of Nanoscience and Nanotechnology, Department of Chemical Engineering, University of Rhode Island, Kingston, RI, 02881

ABSTRACT

New electrochemical approaches have been applied to investigate nanoemulsions (NEs) for their nanostructures and the relevant electrochemical activity by single-entity electrochemistry (SEE). Herein, we make highly monodisperse NEs with ~40 nm diameter, composed of biocompatible surfactants, castor oil as plasticizers, and ion exchangers. Dynamic light scattering (DLS) measurements with periodically varying surfactant to oil ratios provide us with a structural implication about uneven distributions of incorporating components inside NEs. To support this structural insight, we apply SEE and selectively monitor electron-transfer reactions occurring at individual NEs containing ferrocene upon each collision onto a Pt ultramicroelectrode. The quantitative analysis of the nanoelectrochemical results along with DLS and transmission electron microscopy (TEM) measurements reveal nanostructured compartments of incorporating components inside NEs and their effect on the electrochemical behavior. Indeed, a tunneling barrier inside NEs could be formed depending on the NE composition, thus determining an

electrochemical behavior of NEs, which cannot be differentiated by a general morphological study such as DLS and TEM but by our SEE measurements. Furthermore, by employing the nanopipet voltammetry with an interface between two immiscible electrolyte solutions (ITIES) to mimic the NE interface, we could explicitly investigate that the electron-transfer reaction occurring inside NEs is facilitated by the ion-transfer reaction. Overall, these comprehensive electrochemical approaches enable us to elucidate the relation between structures and the electrochemical functionality of NEs and provide quantitative criteria for the proper compositions of NEs regarding their activity in the electrochemical applications. Also, this finding should be a prerequisite for suitable biomedical/electrochemical applications of NEs

INTRODUCTION

Since single-entity electrochemistry (SEE) has been introduced to study single events, the collisions of hard particles such as metal nanoparticles,[1,2] or soft particles[3−9] including emulsions, vesicles, and micelles on an ultramicroelectrode (UME), it has successfully obtained information about the size distribution of particles and the number of molecules loaded inside soft particles. In particular, because of the impact of the size distribution of soft particles on their stability, rheology, optical properties, and sensory attributes,[10,11] SEE has been widely applied to polydisperse micro to submicroemulsions to discretely characterize their size as opposed to ensemble measurements. In fact, owing to their inherent capability in encapsulation, extraction, reactors, and potential delivery vehicles, these emulsions have great potential in electroanalysis as versatile nanocarriers in environmental science, biomedical analysis, pharmaceuticals, and theranostics.[12−14] The

functionality of emulsions, however, tends to be strongly dependent on and determined by their molecular structures because of the sophisticated formulation/manufacturing of emulsions involving various components. Hence, it is critical to understand and characterize their nanostructure and the relevant activity prior to the desired utilization. This characterization of emulsions is a challenging task due to the presence of a variety of structures and components involved in emulsion systems as well as their soft surface and cannot be achieved by a general morphological study such as DLS or electron microscopy.

Herein, we apply SEE uniquely to study the nanostructure inside NEs and their impact on the electrochemical behavior. For this quantitative elucidation of the relations between the nanostructure and the electrochemical activity of NEs, high monodispersity is required in the NE system. Indeed, most SEE studies with polydisperse micro- to submicroemulsions have focused on characterizing their size distribution because the variation in current responses or electrical charges is mainly attributed to the different sizes of emulsions.[3–9,15] Instead, a highly monodisperse NE system allows us to ascribe the variation in the SEE response to its inherent nanostructural effect. Accordingly, we combine high-energy homogenization/ spontaneous-emulsification methods to control the high monodispersity in NEs with ~40 nm diameter, consisting of Pluronic F-127 as a biocompatible surfactant, castor oil as a plasticizer, and hydrophobic borate compounds as ion exchangers.

A series of DLS measurements with periodically varying surfactant to oil ratios (SOR) provide us a distinctive trend in the average size and the relevant zeta (ζ) potential as a measure of the surface charge of NEs, finally showing two characteristic NEs with

similar size but distinctly different ζ potentials. In fact, the morphology of these two types of NEs is nearly identical under the TEM measurements. Only, DLS and TEM studies imply a different inner structure of NEs, leading to an uneven distribution of incorporating components inside NEs. To support our structural insight, we apply SEE, where ferrocene (Fc) incorporated inside NEs is selectively oxidized, thus monitoring electron-transfer (ET) reactions occurring at an individual NE upon its collision onto a Pt UME. The quantitative analysis of these nanoelectrochemical results enables us to attain two novel aspects: (1) estimate an unprecedentedly high concentration of loading molecules (e.g., Fc in this work) inside individual NEs, which is invaluable analytical information for controlling the dose of loads inside NEs as a versatile nanocarrier and (2) relate the ET reaction with electron tunneling across the NE interface. This tunneling-coupled ET reaction is the first trial to explain the ET reaction occurring at the individual soft particles during SEE measurements, where tunneling and ET constitute a serial process leading to the overall current response at a UME.

In fact, most previous SEE studies have generally assumed that the direct contact of intact micro- to submicroemulsions or weakened vesicles by detergents with a UME locally opens up a soft particle upon its collision, thus causing a direct ET.[3–9,15] However, considering the thermodynamic stability governing the micro- to submicroemulsion system, this assumption of a local deformation or structural agitation in emulsions would be thermodynamically implausible because it needs appreciable energy to raise the interfacial tension and/or change the molecular packing in an emulsion system.[11] A more plausible scenario would be that electron tunneling occurs without structural modifications as a soft particle approaches the vicinity of a UME surface. In this case,

any structural factors such as a nanocompartment forming a tunneling barrier inside NEs should have significance when we investigate the emulsion system as a versatile reactor, carrier, or electroanalytical sensor. In that sense, our SEE study with combining DLS and TEM enables us to comprehensively understand nanostructured compartments of incorporating components inside NEs and the relevant electrochemical behavior, thereby elucidating the relation between structures and the respective functionality of NEs. In addition, we apply nanopipet voltammetry using nanopipet-supported interfaces between two immiscible electrolyte solutions (ITIES), which mimics the polarized interface of NEs in SEE measurements. It explicitly confirms that the ET reaction occurring inside NEs is coupled with the ion transfer across NE interfaces. Overall, our electrochemical approach should be a prerequisite and applicable to the adequate utilization of synthesized NEs for this analytical purpose, thus suiting extensive biomedical/ electrochemical applications.

EXPERIMENTAL SECTION

Chemicals.

Pluronic F-127 (F-127), bis(2-ethylhexyl)sebacate (DOS, or castor oil, 97.0%), tetrahydrofuran (THF, 99.9%), ferrocene (Fc, 98%), and potassium tetrakis[3,5-bis (trifluoromethyl)phenyl] borate (KTFPB, 95%) were used as obtained from Sigma-Aldrich. Also, NH_4PF_6 (99.98%), NH_4Cl (99.5%), and tetrabutylammonium chloride (TBA^+Cl^-) (≥97%) were purchased from Sigma-Aldrich and used as obtained. The tetrakis(pentafluorophenyl)borate salt of tetradodecylammonium ($TDDA^+ \cdot TFAB^-$) was obtained by metathesis and used as an organic supporting electrolyte. Nanopure water

(18.2 MΩ·cm, TOC 2 ppb; Milli-Q Integral 5 system, Millipore) was used to prepare all of the aqueous electrolyte solutions as well as in NE synthesis.

Synthesis of Nanoemulsions.

To prepare NEs, 1.8 mg of KTFPB, 3.4 mg of Fc, and 250.0 mg of F127 were dissolved in 3.0 mL of THF in the vial (Fisher Scientific, 8 DR) to form a homogeneous solution. Then, 8.8 μL of DOS was added to this solution. This solution (the so-called THF cocktail) was mixed for 1 h using a vortex mixer (Fisher Scientific, Pittsburgh, PA) with a spinning speed of 3000 rpm. After mixing, a 0.1 mL aliquot from the mixed THF cocktail was forcefully injected into 4.0 mL of nanopure water in the vial (Fisher Scientific, 4 DR) during vortex mixing with a spinning speed of 4000 rpm and continuously vortex mixed for 2 min. This process was immediately repeated for another batch. The resulting 8 mL of nanopure water containing the THF cocktail was then combined and homogenized (Kinematica AG, Polytron system PT 10-35 GT, Switzerland) for 2 min at a rate of 4900 rpm. In this case, 8 mL is the minimum volume used to suppress froth formation during homogenization (with a 4 DR vial). After homogenization, the meniscus level of the resulting mixture was marked. Then, the solution was further purged with N_2 gas to fully evaporate THF for 1 h under a flow rate of 40 psi. Finally, the meniscus level of solution was marked again. A volume reduction of ca. 2 mL was observed after the evaporation step. This final solution is a NE stock solution.

DLS Measurements.

To characterize NEs for the size, size distribution, and ζ-potential, we performed DLS measurements (Malvern Zetasizer Nano ZS, Malvern Instruments Inc., MA). For the sample preparation, 1.0 mL of NE stock solution was diluted with 3.0 mL of nanopure water, and a 1.0 mL aliquot of this diluted solution was taken to fill a DLS cuvette (Malvern DTS 1070, Malvern Instruments Inc., MA). DLS measurements were carried out using a Malvern Nano ZS at 25 °C.

TEM Measurements with the Uranyless Negative Staining Method.

The NEs were visualized with TEM (JEM2100F, JEOL, MA) at 100−200 kV. First, specimens were prepared by depositing 3.0 μL of a NE suspension on the carbon side of a 300 mesh Cu TEM grid with C/Formvar film (FCF-300, Electron Microscopy Sciences, Hatfield, PA) (NE suspension: 1.0 mL of a NE stock sample was diluted in 3.0 mL of nanopure water). After 30 s to allow NE deposition, the solvent was wicked with filter paper. Immediately after, the grid was immersed in a drop of Uranyless negative stain (Delta Microscopies, France) for 30 s. Uranyless negative stain offers a better contrast on the organic molecules by staining a nonradioactive lanthanide mix. The excess stain was wicked using filter paper, and the grid was dried overnight at room temperature and ambient pressure prior to imaging.

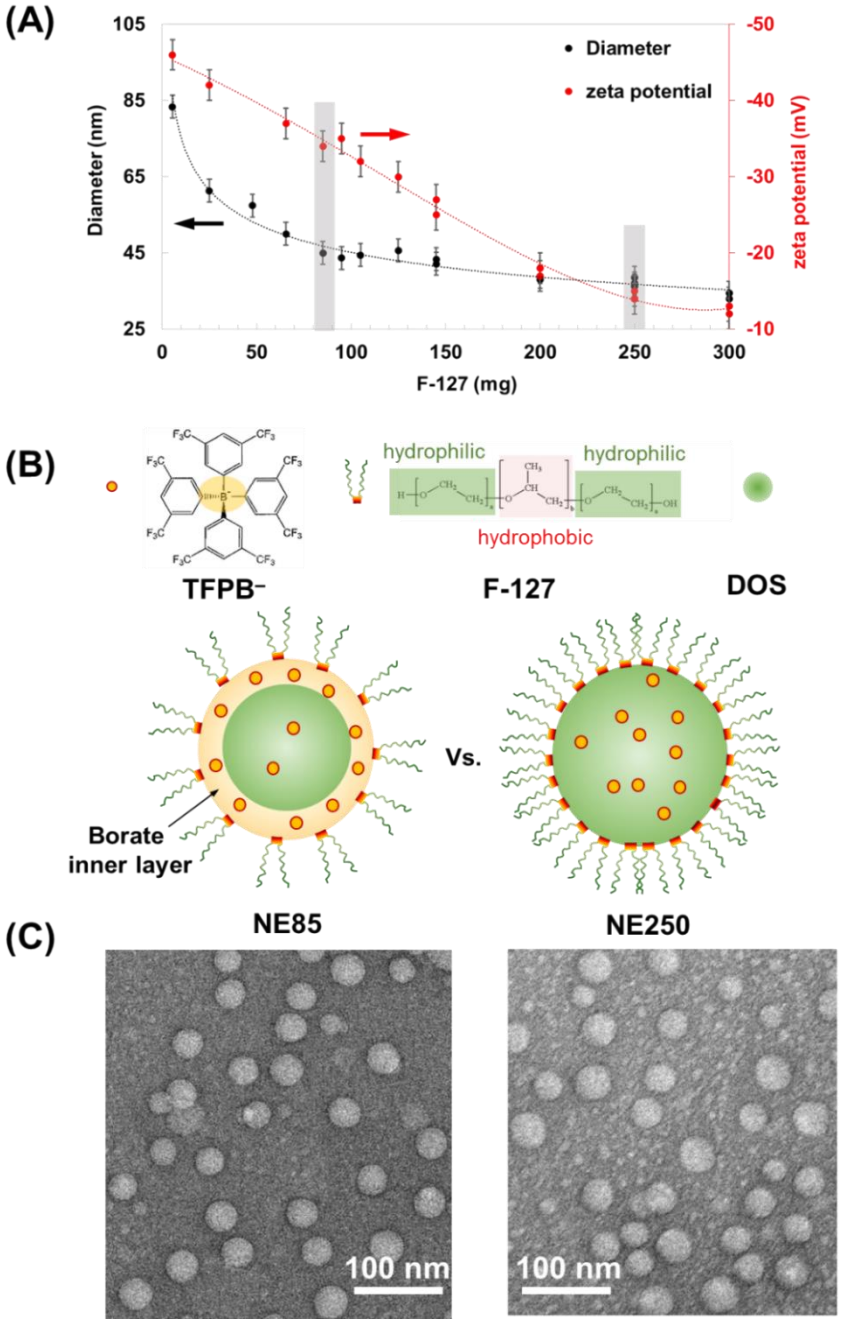

Figure 2.1 (A) NE diameters and ζ-potentials as a function of F-127 amounts, determined by DLS. (B) Schematic illustrations of major components for NE preparation, and hypothesized structures of NE85 (left) and NE250 (right). NE85 has an inner borate layer, while NE250 has randomly distributed borates in it (not in scale). (C) TEM images of NE85 (left) and NE250 (right) obtained at 200 kV by negative staining with 100 pM NE suspensions.

Fabrication of Pt UME and Nanopipet Electrodes.

Pt UME (5 μm diameter) was fabricated by using a CO_2-laser puller, microforge, [16] and then a homemade polisher. Tapered nanopipets with an inner tip radius of ~60 nm were obtained by pulling 10-cm-long quartz capillaries (outer/inner diameter ratio of 1.0/0.7; Sutter Instrument Co., Novato, CA) using a CO_2-laser capillary puller (model P-2000, Sutter Instrument).[17] More detailed information about the fabrication of these electrodes is in the Supporting Information (SI).

SEE Measurements.

SEE was performed in a two-electrode cell using a bipotentiostat (CHI 760E or CHM8022D, CH Instrument, Austin, TX) at ambient temperature (20 °C). Pt UME (5 μm diameter) was immersed in the aqueous solution containing 10 mM NH_4PH_6 or NH_4Cl as a supporting electrolyte. Using the amperometric $i-t$ technique, the current was measured over time by applying a constant potential at 0.85−1.0 V vs the Pt quasi-reference electrode (Pt QRE) to Pt UME.

Nanopipet Voltammetry

Nanopipet voltammetry was carried out in a two-electrode cell at ambient temperature (20 °C). A nanopipet electrode was prepared by using a silanized pipet and filling it with the organic phase containing DOS and 40 mM KTFPB. Using a bipotentiostat (CHI760E, CH Instrument, and Austin, TX), cyclic voltammetry was performed by scanning the potential through a Ni/Cu wire inside the nanopipet against Pt QRE in water. Finally, the

radius and quality of this pipet were characterized by studying the TBA^+ ion transfer. All voltammograms were recorded at a 25 mV/s scan rate. More details are in the SI.

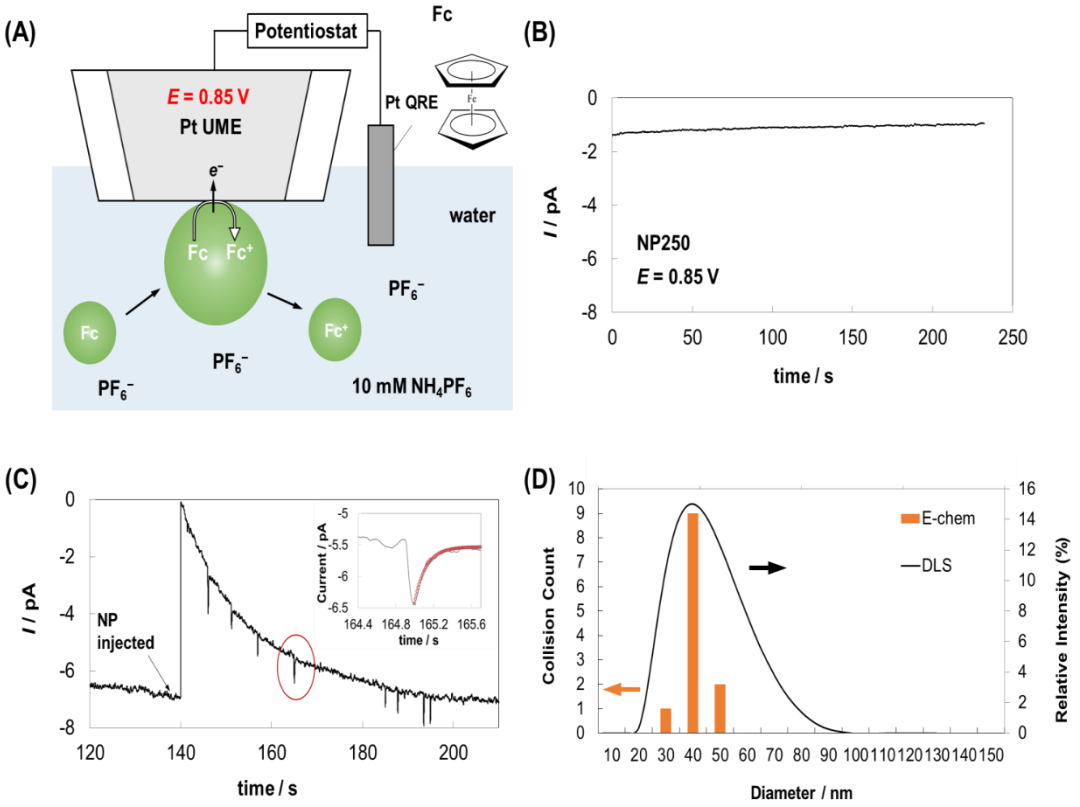

Figure 2.2 (A) Schematic illustration of the SEE measurements in 10 mM NH_4PF_6 with NE250 and Pt UME applied at 0.85 V vs Pt QRE, (B) Background current response at 0.85 V vs Pt QRE in 10mM NH_4PF_6 aqueous solution, (C) *i-t* curves of NE250 collisions at Pt UME under 0.85 V vs Pt QRE. 8 pM NE250 was added at 140 s. Each current spike corresponds to the individual collisions of NE250. The inset is a magnified current spike occurred at t = 165 s, (D) Comparison of calculated NE diameter from the SEE vs. DLS data.

RESULTS AND DISCUSSION

Characterization of Nanoemulsions.

NEs were synthesized by periodically varying the amount of F-127 surfactants from 5.0 to 300.0 mg in 3.0 mL of the THF cocktail. To characterize these NEs, we carried out DLS measurements and monitored the resultant average size, the ζ potential as a measure of NE's surface charges, and the polydispersity index (PDI) as a function of the amount of F-127. Over the wide span of the amount of surfactant, the PDI range was 0.15 ± 0.05, indicating highly monodispersed NEs.[18–20] Unlike the general intuition that elevating the polymer concentration leads to larger NEs, the gradual decrease in the NE diameter was observed with increasing F-127 amount. In fact, it would be more plausible that the smaller NEs have a larger surface area, thus being advantageous with more surfactants to stabilize the smaller NEs. This trend of reduced NE sizes finally reaches a steady-state value of ca. 37 ± 2 nm with a gradual increase in the amount of F-127 to up to 300 mg. Also, the ζ potentials decrease as the amount of F-127 increases. These observed sizes and ζ potentials of NEs are plotted together as a function of the amount of F-127 in Figure 1A. Both sizes and ζ potentials show decreasing trends as the amount of F-127 increases. Notably, NEs with 85 and 250 mg of F-127 (denoted as NE85 and NE250, respectively) have very similar sizes of ∼40 ± 2 nm, whereas the ζ potential, −34 ± 2 mV for NE85, is discernably more negative than −15 ± 2 mV for NE250.

The obvious difference in ζ potentials but similar sizes between NE85 and NE250 inspires us to hypothesize about the inherently different structures of NEs depending on the amount of F-127. With 85 mg of F-127, NE85 would be loosely covered with F-127 surfactants, which might be insufficient to fully stabilize the NEs dispersed in the aqueous phase. In this case, borate compounds ($TFPB^-$) present in NEs as ion exchangers could take on the role of an additional stabilizer. If so, the borate compounds would be preferentially aligned near the exterior surface of NE85. Subsequently, these borate compounds would form an inner layer for the NE85 stabilization. Apparently, the central borate is negatively charged, while it is surrounded by hydrophobic aromatic rings with methyl-fluoro groups. As a result, their contribution to the overall ζ potentials could lead to more negative values. In contrast, NE250 would have enough surfactant to compactly cover the NE surface and be stably dispersed in the aqueous phase, thus the borate compounds do not need to be involved in any structural role. Therefore, a more random distribution of borate compounds is expected inside NE250. Accordingly, the observed ζ potentials of NE250 would be mainly ascribed to the hydroxyl group and the oxide group on the hydrophilic poly (ethylene glycol) chains of F-127.[21] In Figure 2.1B, we schematically illustrate this structural hypothesis of NEs as a function of the amount of F-127.

In good agreement with the DLS findings, TEM visualized uniformly sized particles for both NE85 and NE250 (Figure 1C). TEM images of the NEs were obtained by negative staining and clearly showed the size of NEs, ~40 nm consistent with DLS measurements (more details in the SI). Also, a well-defined spherical shape of NEs in these TEM measurements implies that NEs are robust and kinetically stable even after the dilution of

up to 8−100 pM (Figure S2). Any noticeable difference between NE85 and NE250, however, could not be seen in their morphology by TEM measurements. Certainly, TEM gives us useful information on synthesized NEs, particle sizes, and shapes, but it is limited to the morphological appearance rather than the inner structure of NEs, especially for soft nanoparticles, as a result of the low contrast of the NE components. Additionally, TEM requires the sample to be dried, which can induce changes in the NE morphology due to dehydration. Accordingly, to prove our structural hypothesis and study the electrochemical behavior of two different NEs, we performed SEE. We will explain more details in the next section. The mechanistic aspects in forming monodispersed nanoemulsions with a ~40 nm diameter are further discussed in detail in the SI.

SEE with Nanoemulsions.

To validate our structural hypothesis about NEs and study the relevant electrochemical behavior of NEs, we performed the SEE. Herein, we studied NEs containing Fc as sensing molecules as prepared above. Since Fc is highly lipophilic, it can be dissolved and dispersed only inside NEs bodied with castor oil. When NEs are dispersed in the aqueous solution, they spontaneously diffuse and collide onto a Pt UME, at which an oxidative potential is applied to drive the Fc oxidation reaction (Figure 2.2A). In this case, the applied potential is high enough to instantaneously oxidize Fc inside NE but low enough not to oxidize the water in aqueous bulk solution. Upon the collision of NE onto Pt UME, a current spike is consequently seen, as the Fc in NE is electrolyzed until its depletion. The frequency of the spike response would be dependent on the concentration and diffusion constant of NEs as well as the size of the electrode as below[3]

$$f_{NE} = 4D_{NE}C_{NE}a_{UME}N_A \qquad (1)$$

where D_{NE} and C_{NE} are the diffusion coefficient and concentration of NEs, respectively, a_{UME} is the radius of a Pt UME, and N_A is Avogadro's number. Herein, D_{NE} can be estimated by the Stokes−Einstein relations as[3]

$$D_{NE} = \frac{k_B T}{6\pi\eta r_{NE}} \qquad (2)$$

where k_B is the Boltzmann constant, T is temperature (K), η is the viscosity of water at 25 °C (0.89 mPa·s), and r_{NE} is a radius of NE. For 20 nm of r_{NE}, the calculated D_{NE} is 1.05 × 10^{-7} cm^2/s.

For the SEE measurements, a 5 μm diameter Pt UME was immersed in the aqueous solution containing 10 mM NH_4PF_6 as a supporting electrolyte. A constant potential, 0.85 V vs Pt QRE, was applied to a Pt UME, which is more positive than 0.8 V determined by voltammetry with a THF cocktail solution (SI). A more positive potential is chosen for Fc oxidation diffusion-controlled conditions based on the consideration of the lower dielectric constant (ε = 4.7) of castor oil compared to that of THF (ε = 7.58), thus there is a larger uncompensated resistance inside NEs. At this potential, a mere background current was observed in the aqueous bulk solution, indicating negligible water oxidation at a Pt UME (Figure 2.2B). Once 100 μL of the NE250 aliquot was introduced into 5 mL of the aqueous bulk solution (i.e., the final concentration of NE250 is 8 pM), distinctly sharp current spikes appeared (Figure 2.2C). Interestingly, the current spikes show fairly uniform magnitudes over time, implying monodisperse NE250 as observed in DLS and TEM measurements. Charges (Q) needed to oxidize Fc in NE250 are estimated by integrating each current spike over time. The observed charges range from 24 to 96 fC. Using this charge and the Fc concentration, C_{Fc}, the NE250 diameter, d_{NE} is evaluated by

$$d_{NE} = 2\sqrt[3]{\frac{3Q}{4\pi F C_{Fc}}}$$

where Q is an integrated charge from a current spike (C), F is the Faraday constant (96485 C/mol), and C_{Fc} is the Fc concentration in a NE droplet dissolved in castor oil (15.8 M) predicted in the former section.

The overall distribution of NE250 diameters calculated by eq 3 is illustrated and compared with DLS data in Figure 2D. Notably, the obtained diameter of ~40 nm is consistent with the average diameter measured by DLS methods as well as TEM images. Besides, the distribution from the SEE is narrower by a factor of ~3 than the DLS measurements. This narrow distribution is mainly attributed to the chemical specificity in the electrochemical measurements, where only NEs are selectively monitored by direct Fc oxidation, whereas debris or nanobubbles indistinguishable in DLS measurements would not affect the electrochemical study. Electrochemistry results in good agreement with DLS and TEM observation also indicate that F-127 surfactants do not hinder the electron transfer occurring inside NE250 because all Fc in NE250 could be fully electrolyzed upon the collision, and thus the observed charge matches the predicted value.

With our experimental setup, the limit of detection is ~20 fC for the observable charge in the SEE. To detect a discernible current spike corresponding to 20 fC, NE250 should contain more than 7.2 M Fc if a fixed diameter of 39 nm NE250 is assumed on the basis of the average diameter in DLS measurements. This mathematical speculation already exceeds ~6 M Fe in FuelSpec 118 series colloidal dispersions as reported.[22] Because the experimentally observed charges range from 24 to 96 fC, it should be estimated that Fc

on the order of 10 M is present in NE250. Actually, this estimation is consistent with our original prediction of 15.8 M Fc in NEs via preconcentrating Fc during THF evaporation. Interestingly, when we increase the Fc concentration to 7 mM in the initial THF cocktail, a yellow precipitate of Fc immediately sunk into the final NE stock solution. Considering an ~2600-fold preconcentration of Fc inside NEs during NE synthesis, this slight increase in Fc concentration in the initial THF cocktail reaches ~18.7 M inside NE, causing sharp precipitation. Therefore, ca. 15.8 M Fc in NEs could be under full saturation as a maximum concentration and exist in a colloidal state. The experimental collision frequency was estimated to be 0.13 Hz, where eight nearly uniform current spikes are monitored in ~60 s. Noticeably, this frequency is close to the theoretical one, 0.16 Hz, under the given condition of 8 pM NE250 with $D_{NE} = 1.05 \times 10^{-7}$ cm^2/s and a 2.5 μm radius of a_{UME}, estimated by eq 1. This good agreement between the observed collision frequency and theoretical prediction indicates that our SEE measurement is mainly governed by diffusion without the migration effect.[23] Note that the concentration of supporting electrolyte is 9 orders of magnitude higher than the NE concentration, where the electrostatic effect could be negligible in our SEE measurements.

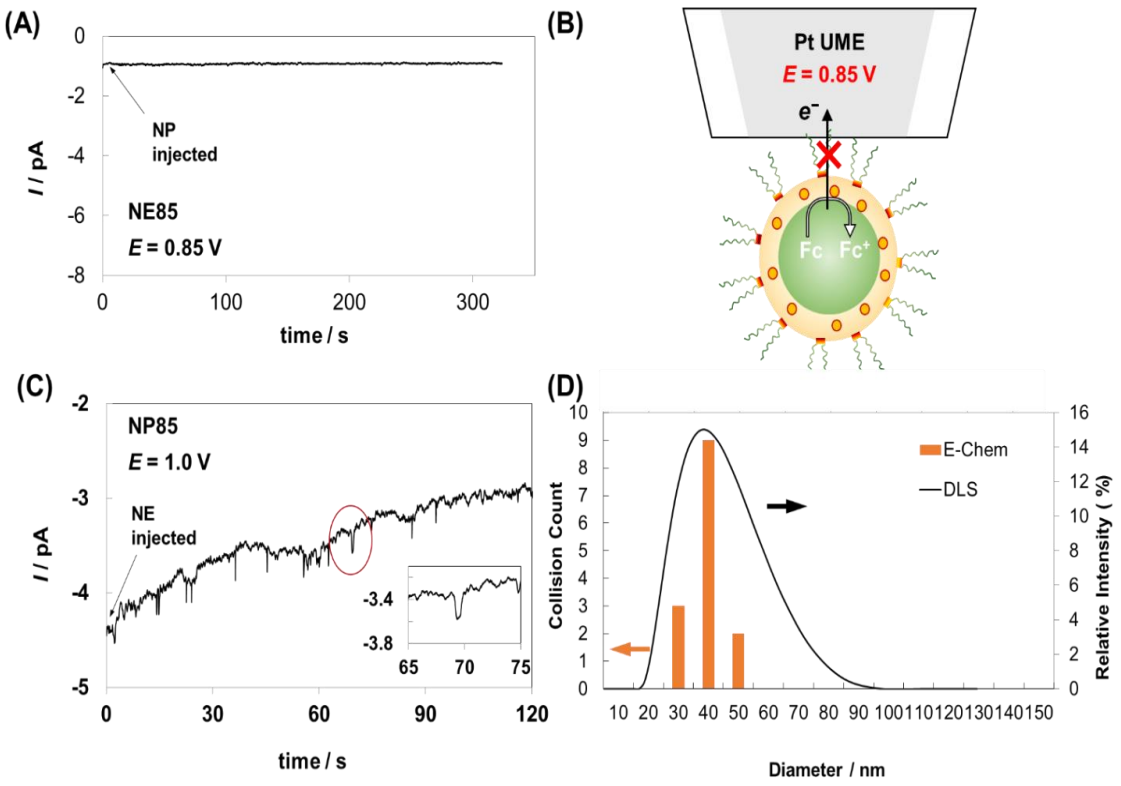

Figure 2.3 (A) *I-t* curves of NE85 collisions at Pt UME under 0.85 V vs Pt QRE. 8 pM NE85 was added at zero time. (B) Schematic illustration of the hypothesized electron transfer reaction at NE85, where the inner borate layer would hinder an electron-tunneling from NE85 to Pt UME. (C) *i-t* curves of NE85 collisions at Pt UME under 1.0 V vs Pt QRE. 8 pM NE85 was added at zero time. The inset is a magnified current spike occurred at t = 70 s. (D) Comparison of calculated NE diameter from the SEE vs. DLS data.

Inner Borate Layer: A Tunneling Barrier.

NE85 was also tested with SEE under the same conditions as for NE250 measurements. Surprisingly, typical current spikes could not be observed, when the constant potential of 0.85 V was applied to the Pt UME (Figure 2.3A). Earlier, we hypothesized that the inner borate layer might exist near the exterior surface of NE85, unlike NE250. If so, would this layer hinder a facile electron transfer occurring inside NE85, thus being a tunneling barrier (Figure 2.3B).

Actually, upon the NE collision onto a Pt UME, we can think of two-stage serial processes: the electron tunneling from the density of states of Fc in NE to the Pt UME across a NE interface and the electrochemical reaction (or electron transfer reaction) in which Fc is oxidized to Fc^+ inside a NE. In this case, the total electrical current under the steady state can be expressed as a reciprocal sum of two-stage serial processes (the tunneling and the electrochemical reaction) as[24-27]

$$\frac{1}{i_{total}} = \frac{1}{i_{tun}} + \frac{1}{i_{echem}}$$

where i_{total}, i_{tun}, and i_{echem} are the total current, tunneling, and electrochemical currents, respectively. Equation 4 means that the smaller term rules the total current. In fact, the sole presence of F-127 as surfactants hardly affected the electron transfer upon the collision of NE250 since not only a distinct current spike is observed upon NE collision, but also charges observed for Fc oxidation are consistent with the theoretical prediction. Hence, for NE250, the observed current could be mainly governed by the electrochemical reaction, implying that the electron tunneling is very facile across the surfactant layer ($i_{tun} \gg i_{echem}$).

For the case of NE85, however, if an additional inner borate layer with the surfactant acts as a tunneling barrier, thus significantly shutting down the electron tunneling, then the overall current could be controlled by tunneling since $i_{tun} \ll i_{echem}$. The tunneling current, i_{tun}, at a small bias voltage can be expressed as[24,28,29]

$$i_{tun} \propto \text{constant} \cdot V \cdot \exp(-2\sqrt{\frac{2m\varphi}{\hbar^2}}d)$$

where V is an electrical voltage applied between an electrode and a sample (i.e., NE inside), m is the electron mass, φ is the height of a tunneling barrier, $\hbar$ is the reduced Plank constant (1.054×10^{-34} J·s), and d is a barrier width. According to eq 5, i_{tun} depends exponentially on the distance d. For example, with φ = 4 eV, i_{tun} is reduced by a factor of 10 for every 0.1 nm increase in d. This means that over a typical atomic diameter of 0.3 nm the i_{tun} value changes by a factor of 1000. Also, if the electron energy is lower than the tunneling barrier, then the probability of electrons tunneling through a barrier would be very low, thus leading to a low i_{tun}. This i_{tun}, however, can be modulated by adjusting V because the current is proportional to the electrical voltage, V. With increasing V, an electron with higher energy can overcome a tunneling barrier and raise the tunneling probability, thereby increasing i_{tun}. Practically, a higher potential applied to a Pt UME can increase the electrical voltage between a Pt UME and a NE inside, thus causing an increase in i_{tun}. When i_{tun} exceeds i_{echem} (i.e., $i_{tun} \gg i_{echem}$), the overall condition for the given electron transfer system can be modulated from a tunneling-controlled to an electrochemical-reaction-controlled regime according to eq 4.

On the basis of this speculation, a higher potential, 1.0 V instead of 0.85 V, was applied to a Pt UME during the SEE. As predicted, in the presence of NE85, distinct current

spikes appeared upon their collisions (Figure 3C). Also, the observed charges ranged from 26 to 93 fC, which is similar to NE250 measurements. Using the integrated charges from the current spikes and eq 3, a narrow distribution curve was constructed (Figure 2.3D). The obtained diameter~40 nm is consistent with the average diameter measured by DLS methods as well as TEM images. This good agreement indicates that Fc in NE85 could be fully electrolyzed by overcoming the tunneling barrier, thereby confirming the presence of a borate inner layer inside NE85 and its electrochemical behavior as a tunneling barrier. Again, the distribution from the SEE is narrower by a factor of ~3 than the DLS measurements owing to the chemical specificity in the electrochemical measurements.

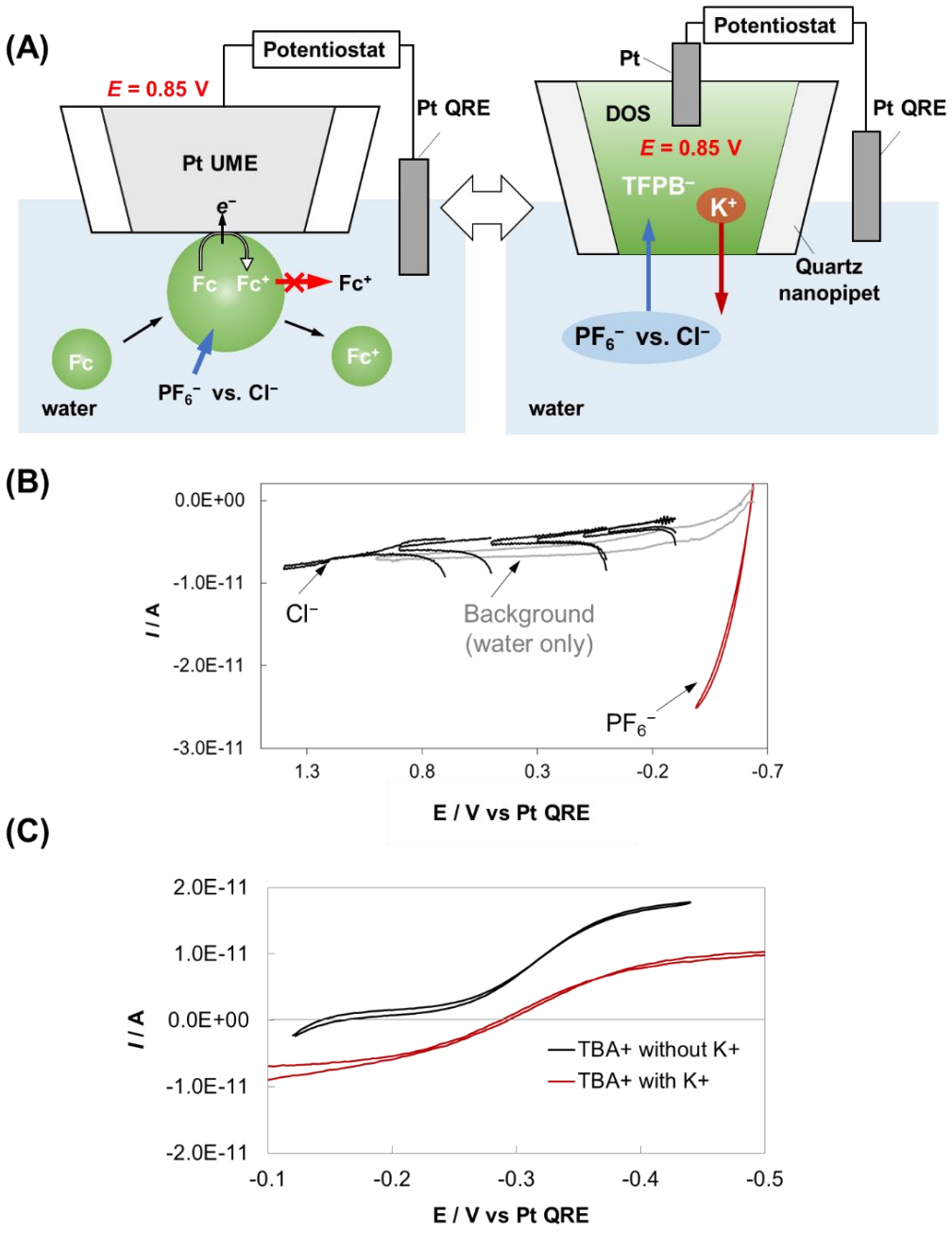

Figure 2.4 (A) Schematic representations (left) of the electron transfer reaction coupled with ion transfer reactions in NE during the SEE, (right) the nanopipet-supported ITIES mimicking NE in the nanopipet voltammetry, (B) Voltammograms of PF_6^- (red curve) and Cl^- (black curves) ion transfers. The background voltammogram was measured in the nanopure water without any anions (gray curve), (C) Voltammograms of TBA^+ transfer with (red curve) and without K^+ ions (black curve) inside the nanopipet. TBA^+ 0.9 mM was dissolved in both aqueous solution.

Electron Transfer Reactions Facilitated by Ion Transfer Reactions: **Nanopipet Voltammetry**.

When we monitor the collisional response of NEs with both NE85 and NE250, the current spikes appear only in the presence of 10 mM NH_4PF_6 in aqueous bulk solution. Interestingly, no current spikes have been observed upon the collision of any NEs in either nanopure water or 10 mM NH_4Cl (data not shown). From these observations, we hypothesize that the ion transfer reaction might be coupled with the electron transfer reaction occurring inside NEs. Bard and co-workers also suggested that the ion transfer must occur to facilitate the electron transfer at a microemulsion droplet.[30] In fact, when Fc is oxidized to Fc^+ in NEs, the charge neutrality should be maintained in NEs during this Faradaic process (Figure 2.4A left panel). This means that when Fc^+ is produced in NEs, either Fc^+ and/or K^+ must leave the NEs or anions in aqueous solution should enter the oil phase inside the NE across the interface. The spontaneous leaving of Fc^+, however, does not seem eligible under our experimental conditions because no current spikes are observed in the nanopure water during the SEE. This indicates that Fc^+ might be too hydrophobic to spontaneously enter the aqueous phase.

Herein, we experimentally prove our hypothesis about the coupling between ion transfer and electron transfer reactions in NE. Using a nanopipet-supported interface between two immiscible electrolyte solutions (ITIES), we mimic the NE and study the ion transfer across ITIES using nanopipet voltammetry. In this work, a nanopipet is filled with castor oil (DOS) and KTFPB and immersed in the aqueous solution containing NH_4PF_6 or NH_4Cl. Under this condition, the organic phase in the nanopipet represents the body of NEs, thereby the ingress of anions such as PF_6^- or Cl^- from aqueous bulk solution to the

organic phase or the egress of cation K^+ from the organic phase to the aqueous bulk solution is studied (Figure 2.4A, right panel).

First, for the study of the anionic transfer from the aqueous to the organic phase, the potential was scanned from the negative to positive direction. Respective voltammograms of 1 mM PF_6^- and Cl^- are shown in Figure 4B. Since PF_6^- is a hydrophobic anion compared to Cl^-, the voltammogram of PF_6^- transfer appears at less positive potentials with $E_{1/2}$= −0.56 V vs Pt QRE, implying facile ion transfer from the aqueous to the organic phase (red curves in Figure 2.4B).[31] Accordingly, a diffusion-controlled current can be obtained even at 0.85 V vs Pt QRE, where SEE is carried out as well. On the contrary, for a hydrophilic anion such as Cl^-, a larger amount of energy is needed to drive interfacial ion transfer from the aqueous to the organic phase. Resulting voltammograms studied from −0.2 to 1.4 V did not show any discernible current compared to the background current (black curves for Cl^- and gray curves for the background in Figure 2.4B). This result clearly indicates that it would be difficult to drive Cl^- transfer to the organic phase of NEs within the available potential window in our SEE. Hence, the charge neutrality in NE cannot be maintained during Fc oxidation upon NE collision, thus Fc oxidation in NE cannot be completed. Therefore, no current spikes are expected upon NE collision during the SEE in the presence of Cl^- in aqueous solution. In contrast, hydrophobic anion PF_6^- can easily accommodate the charge neutrality during Fc oxidation in NEs because of its facile ion transfer across the NE interface, and this enables us to observe the NE collisions with distinct current spikes in the SEE.

Meanwhile, K^+ from ion exchanger KTFPB in the organic phase should be considered in this interfacial ion transfer. In particular, the contribution of K^+ ion transfer would be

nontrivial because of the high concentration of ~1.73 M KTFPB in each NE. Also, the egress of K^+ from the organic to the aqueous phase would be fairly plausible because K^+ is a hydrophilic cation, thus being more stable in the aqueous phase. The nanopipet voltammetry, however, could not show well-resolved voltammograms for K^+ ion transfer (data not shown) because the background current rises at extreme potentials due to the deformation of the pipet interface in that potential range as well.[32] Instead of the direct study of K^+ ion transfer, we compared tetrabutylammonium (TBA^+) ion transfer in the presence of K^+ inside the pipet to TBA^+ transfer in the absence of K^+ (Figure 4C). We could clearly observe that the overall voltammogram of TBA^+ transfer is vertically shifted in the negative direction in the presence of K^+ inside the pipet. This result indicates that the ingress of TBA^+ from the aqueous to the organic phase and the egress of the K^+ ion from the organic to the aqueous phase occur simultaneously in this potential window (−0.1 to −0.5 V). This data, however, is not straightforward enough to estimate $E_{1/2}$ of K^+ ion transfer. Also, even if the egress of K^+ ion transfer occurs within the available potential window in our SEE, thus enabling us to maintain the charge neutrality during Fc oxidation in NE, 1.73 M K^+ is insufficient to accommodate the full oxidation of 15.72 M Fc in NE. In this case, only oxidizing ~11 % of the entire amount of Fc leads to 8.5 fC for ~40 nm diameter NE during the SEE. However, this charge is not detectable with our current instrument.

As a result, the overall charge neutrality in NE should be acquired mainly by the ingress of hydrophobic anion PF_6^- and/or maybe additionally by the egress of K^+. Finally, we can envision that during the SEE with NEs at 0.85−1.0 V, the PF_6^- ion transfers across the polarized NE interface to the organic phase in NE with diffusion control while Fc is fully

oxidized until its depletion in the NE. The nanopipet voltammetry applied here offers a straightforward way to estimate the $E_{1/2}$ of ion transfer at a water/oil interface in lieu of a NE interface and to predict the feasibility of a coupling between ion transfer and electron transfer reactions, thereby experimentally confirming that electron transfer reactions in NEs are facilitated by ion transfer reactions.

CONCLUSIONS

In this work, we could electrochemically characterize the nanostructures inside NEs, which is required to obtain a clear perspective of the relevant electrochemical functionality and the electrochemical applications of NEs. Combining techniques of SEE and nanopipet voltammetry with DLS and TEM enabled us to obtain (1) a mechanistic understanding of the synthesis of monodispersed NEs with ca. 40 nm diameter, (2) the structural understanding of nanostructured compartments inside NEs, (3) the relevant electrochemical behaviors of NEs, and (4) the electron/ion transfer reactions involved in electrochemical measurements with NEs. Therefore, we could elucidate the relation between the structures and respective functionality of NEs, a crucial theme in nanoscience. Our comprehensive electrochemical approach provides us quantitative criteria for proper compositions of NEs in their electrochemical applications. Also, this finding should be a prerequisite for suitable biomedical/electrochemical applications of NEs.

Author Information

Corresponding Author

*Phone: +1 (401) 874-2143. E-mail: jkim25@uri.edu.

ORCID

Jiyeon Kim: 0000-0002-7624-6766

Irene Andreu: 0000-0001-7689-2269

Author Contributions

All authors have given approval to the final version of the manuscript

Notes

The authors declare no competing financial interest.

Supporting Information

Experimental section, Mechanistic Aspects in Forming Monodispersed Nanoemulsions with ~40 nm Diameter, TEM images obtained with 8 pM NE suspension, Picture of synthesized NEs, Characterization of Nanopipets and Pt UMEs, Cyclic voltammetry for Fc oxidation in THF cocktail solution, More electrochemical measurements in SEE.

Acknowledgements

This work was supported by the Research Bridge Funding Initiative, Start up fund from University of Rhode Island, and Medical Research Fund (20174373) from Rhode Island Foundation. This material is based upon work conducted at the RI Consortium for Nanoscience and Nanotechnology, supported by the National Science Foundation EPSCoR Cooperative Agreement #OIA-1655221 and the College of Engineering at URI.

REFERENCES

(1) Zhou, H.; Fan, F.-R. F.; Bard, A. J. J. Phys. Chem. Lett. 2010, 1, 2671−2674.

(2) Kwon, S. J.; Fan, F.-R. F.; Bard, A. J. J. Am. Chem. Soc. 2010, 132, 13165−13167.

(3) Kim, B.-K.; Boika, A.; Kim, J.; Dick, J. E.; Bard, A. J. J. Am. Chem. Soc. 2014, 136, 4849−4852.

(4) Lebegue, E.; Anderson, C. M.; Dick, J. E.; Webb, L. J.; Bard, A. J. Langmuir 2015, 31, 11734−11739.

(5) Toh, H. S.; Compton, R. G. Chem. Sci. 2015, 6, 5053−5058. (6) Nissim, R.; Batchelor-McAuley, C.; Compton, R. G. ChemElectroChem 2016, 3, 105−109.

(7) Cheng, W.; Compton, R. G. Quantifying the Electrocatalytic Turnover of Vitamin B12-Mediated Dehalogenation on Single Soft Nanoparticles. Angew. Chem., Int. Ed. 2016, 55, 2545−2549.

(8) Laborda, E.; Molina, A.; Espín, V. F.; Martínez-Ortiz, F.; de la Torre, J. G.; Compton, R. G. Angew. Chem. 2017, 129, 800−803.

(9) Cheng, W.; Compton, R. G. Investigation of Single-DrugEncapsulating Liposomes Using the Nano-Impact Method. Angew. Chem., Int. Ed. 2014, 53, 13928−13930.

(10) McClements, D. J. Crit. Rev. Food Sci. Nutr. 2007, 47, 611−649.

(11) McClements, D. J. Soft Matter 2012, 8, 1719. (12) Krauel, K.; Davies, N. M.; Hook, S.; Rades, T. J. Controlled.

12) Krauel, K.; Davies, N. M.; Hook, S.; Rades, T. J. Controlled Release 2005, 106, 76−87.

(13) Solans, C.; Izquierdo, P.; Nolla, J.; Azemar, N.; Garcia-Celma, M. J. Curr. Opin. Colloid Interface Sci. 2005, 10, 102−110.

(14) Ali, A.; Ansari, V. A.; Ahmad, U.; Akhtar, J.; Jahan, A. Drug Res. (Stuttgart, Ger.) 2017, 67, 617−631.

(15) Kim, B.-K.; Kim, J.; Bard, A. J. J. Am. Chem. Soc. 2015, 137, 2343−2349.

(16) Kim, J.; Izadyar, A.; Nioradze, N.; Amemiya, S. J. Am. Chem. Soc. 2013, 135, 2321−2329.

(17) Puri, S. R.; Kim, J. Anal. Chem. 2019, 91, 1873−1879.

(18) Badran, M. Digest J. Nanomater. Biostruct. 2014, 9, 83−91.

(19) Chen, M.; Liu, X.; Fahr, A. Int. J. Pharm. 2011, 408, 223−234.

(20) Putri, D. C.; Dwiastuti, R.; Marchaban, M.; Nugroho, A. K. J. Pharm. Sci. Commun. 2017, 14, 79−85.

(21) Suthiwangcharoen, N.; Nagarajan, R. RSC Adv. 2014, 4, 10076−10089.

(22) http://www.fuelspec.com/.

(23) Boika, A.; Thorgaard, S. N.; Bard, A. J. J. Phys. Chem. B 2013, 117, 4371−4380.

(24) Hill, C. M.; Kim, J.; Bard, A. J. J. Am. Chem. Soc. 2015, 137, 11321−11326.

(25) Wei, C.; Bard, A. J.; Mirkin, M. V. J. Phys. Chem. 1995, 99, 16033.

(26) Liu, B.; Bard, A. J.; Mirkin, M. V.; Creager, S. E. J. Am. Chem. Soc. 2004, 126, 1485−1492.

(27) Andrieux, C. P.; Savéant, J.-M. Molecular Design of Surfaces; Murray, R. W., Ed.; John Wiley & Sons: New York, 1992; p 207.

(28) Hill, C. M.; Kim, J.; Nataraju, B.; Bard, A. J. J. Am. Chem. Soc. 2017, 139, 6114−6119.

(29) Hansma, P. K.; Tersoff, J. J. Appl. Phys. 1987, 61, R1.

(30) Deng, H.; Dick, J. E.; Kummer, S.; Kragl, U.; Strauss, S. H.; Bard, A. J. Anal. Chem. 2016, 88, 7754−7761.

(31) Kim, J.; Izadyar, A.; Shen, M.; Ishimatsu, R.; Amemiya, S. Anal. Chem. 2014, 86, 2090−2098.

(32) Perry, D.; Momotenko, D.; Lazenby, R.; Kang, M.; Unwin, P. R. Anal. Chem. 2016, 88, 5523−5530.

CHAPTER 3

IN SITU MEASURING PARTITION COEFFICENT OF NANOEMULSIONS: A NEW APPLICATION OF SINGLE ENTITY ELECTROCHEMISTRY

Hiranya madawala[1], Shahsika Gunathilaka Sabaragamuwe[1],Jiyeon Kim[1*]

[1]. Department of chemistry, University of Rhode Island, Kingston, RI,02881

This manuscript is formatted for publication according *ACS Analytical Chemistry* standards and currently under review.

CHAPTER 03

IN SITU MEASURING PARTITION COEFFICENT OF NANOEMULSIONS: A NEW APPLICATION OF SINGLE ENTITY ELECTROCHEMISTRY

Hiranya madawala[1], Shahsika Gunathilaka Sabaragamuwe[1], Jiyeon Kim[1*]

[1.] Department of chemistry, University of Rhode Island, Kingston, RI, 02881

ABSTRCT

We demonstrate a new application of the single entity electrochemistry to in-situ measure a partition coefficient of intact nanoemulsions (NEs). The partition coefficient of NEs is the most crucial physicochemical property to determine the uptake of delivery molecules. It, however, has not been unequivocally elucidated with intact NEs by currently existing techniques based on ex-situ measurements. Herein, we apply single entity electrochemistry (SEE) to directly and quantitatively measure the partition coefficient of NEs in situ. In this work, we use NEs functionalized with amphiphilic block copolymer (Pluronic-127) as a model system to extract/preconcentrate 2-aminobiphenyl (2-ABP) dissolved in the water, and employ SEE to quantitatively estimate the amounts of 2-ABP distributed into each NE at an individual level in situ. Our SEE measurements reveal that the partitioning is governed by extraction of 2-ABP inside NEs rather than adsorption of 2-ABP on NE surface, and this extraction is markedly efficient to reach ~8 orders of

magnitude for the preconcentration factor, thus leading to the unprecedentedly large partition coefficient of 1.9 (± 1.4) × 10^{10}. This result implies that both the thermodynamic distribution and the intermolecular interaction of extracted compounds in given NEs could play a significant role in the overall partition coefficient (P = 1.9 (± 1.4) × 10^{10}). The experimentally determined partition coefficient was validated by molecular simulations with showing a stabilizing role of intermolecular interaction in the partitioned system. Significantly, our new approach can be readily applicable to investigate practical NEs commercially marketed for drug, food, and cosmetics.

INTRODUCTION

Nanoemulsions (NEs) are oil-in-water (o/w) emulsions with mean droplet diameters ranging from 50 to 500 nm.[1] Owing to this small size and the hydrophobic environment inside NEs, NEs have emerged as a promising strategy for the efficient delivery of hydrophobic molecules e.g. drugs, food, or cosmetics, thus attracting NE applications in personal care, cosmetics and health care.[1,2,3]

This strategy strongly relies on the partition coefficient of NEs, which is the crucial physicochemical property for their applications. The partition coefficient is defined as the ratio of delivery compounds distributed between the organic phase and aqueous phase in equilibrium for a delivery system.[4] It determines the uptake or encapsulation of delivery compounds in NEs,[5,6] and the capacity of NEs to dissolve large quantities of hydrophobes, along with their ability to protect these compounds from hydrolysis and degradation.[1]

In general, the partition coefficient of target compounds at NEs have been determined by common analytical techniques such as high performance liquid chromatography (HPLC),[7,8] reverse-phase HPLC,[9,10] FTIR spectroscopy,[11] UV-Vis spectrophotometry,[12] or scanning electrochemical microscopy.[13] These approaches, however, only offer indirect and ex situ measurements, where the concentrated NEs are ultrafiltrated or centrifuged, then the filtrate is analyzed by the corresponding techniques, or an alternative mimicking system is indirectly studied.[7,8,13,14] Although these measurements provide an important insight about partition coefficient a of NEs, the accuracy, precision, and the relevance of the determined value for intact NEs is equivocal. Even for the commercially marketed NEs, the partition coefficient is vaguely given based on these ex situ measurements.[15] More importantly, understanding whether the partitioning is governed by extraction or adsorption phenomenon, is a prerequisite to fully utilize the extraction efficiency of NEs. The general ex situ approaches, however, cannot explicitly elucidate the partitioning process in NEs.

Herein, we demonstrate the first application of single entity electrochemistry (SEE) to in situ measure the partition coefficient at intact NEs at an individual level. In the earlier work, we have uniquely applied SEE to study the inner-structure of monodisperse NEs and the structural impact on NE's electrochemical behaviors,[16] whereas SEE has been widely applied to polydisperse NEs to discretely characterize their size distribution as opposed to ensemble measurements.[17]

In this study, as a model system, we select NEs practically used for pharmaceutical[7] or photochemical applications,[18,19] and investigate their partition coefficient using 2-aminobiphenyl (2-ABP) as a targeting hydrophobe. Particularly, NEs studied here are

highly monodisperse, which is more than adequate in this work, since responses in SEE measurements would depend on not the size of NEs but the amount of partitioned molecules. Also, we interrogate current-time responses observed in real-time during SEE measurements to clarify the governing process of partitioning. Further, we perform the molecular simulations to validate the experimentally determined partition coefficient of NEs as well as gain the molecular insight in the partitioned system. In the analytical point of view, the combination of SEE and NEs with high monodispersity could offer the high accuracy and precision in the present study.

EXPERIMENTAL SECTION

Chemicals.

Pluronic F-127 (F-127), bis(2-ethylhexyl)-sebacate (DOS, or castor oil, 97.0%), tetrahydrofuran (THF, 99.9%), 2-aminobiphenyl (2-ABP, 97%), and potassium tetrakis[3,5-bis (trifluoromethyl)phenyl] borate (KTFPB, 95%) were used as obtained from Sigma-Aldrich. Also, Ammonium hexafluorophosphate, NH_4PF_6 (99.98%), ferrocenemethanol (97%), ammonium phosphate monobasic (98%) and ammonium phosphate dibasic (98%) were purchased from Sigma-Aldrich and used as obtained. Nanopure water (18.2 MΩ·cm, TOC 2 ppb; Milli-Q Integral 5 system, Millipore) was used to prepare all the aqueous electrolyte solutions as well as NE synthesis.

Solution preparation.

0.0017 g of 2-ABP was dissolved in 2 L of nanopure water and 5 µM stock solution was prepared. From 2-ABP stock solution, a series of diluted solutions ranging from 3 µM to 1 nM were prepared. The aqueous solution contained 10 mM ammonium

hexafluorophosphate with the pH adjusted to pH 7 with 2 mM ammonium monobasic phosphate and ammonium dibasic phosphate.

SEE Measurements.

SEE was performed in a two-electrode cell using a bipotentiostat (CHM8022D, CH Instrument, Austin, TX) at ambient temperature (20 °C). A Pt UME (5 μm diameter) was immersed in the aqueous solution containing 10 mM NH_4PF_6 and 2 mM phosphate buffer. The constant potential optimized to 0.85 V vs the Pt quasi-reference electrode (Pt QRE) was applied for the amperometric *i*−*t* measurements during SEE. More information about synthesis of nanoemulsions, TEM measurements with the Uranyless negative staining method, and fabrication of Pt UMEs is in SI.

RESULTS AND DISCUSSION

Practical Nanoemulsions for a Model System.

We utilized NEs functionalized with amphiphilic block copolymers (Pluronic F-127) and castor oil plasticizer. Similar composition of NEs has been employed in optical nanosensing[18, 19] or pharmaceutical extractor.[7] The optimized synthesis of our NE attained the high monodispersity in size with 40 (± 5) nm diameter through the characterization by TEM (Figure 3.1B and 3.1C). High monodispersity observed in both low and high resolution TEM images is consistent with DLS measurements with 38 nm diameter and 0.15 (± 0.05) polydispersity index (PDI) (Figure S1). These highly monodisperse NEs are more than adequate in this work, since responses in SEE measurements is independent of size of NEs

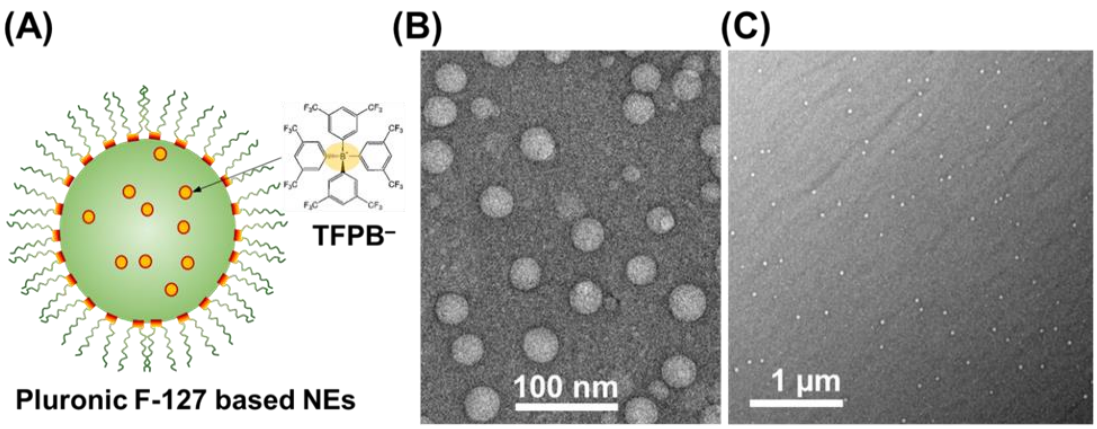

Figure 3.1 (A) Schematic illustration of Pluronic F-127 decorated NEs containing cation exchanger, $TFPB^-$ and castor oil as plasticizer. (B), (C) TEM images at high and low resolutions, respectively. Notably, high monodispersity of NEs is observed over the wide range.

Single Entity Electrochemistry with Individual NEs Partitioned with 2-ABP from Aqueous Bulk Solution.

To estimate a partition coefficient of given NEs, 2-ABP was used as model delivery molecule. 2-ABP is highly hydrophobic with a large partition coefficient of 691.8 between octanol and water.[20] 2-ABP undergoes one electron transfer oxidation reaction to form cationic radical, often followed by polymerization reaction depending on the experimental condition (Figure S2), where the electropolymerization is triggered at extremely positive oxidation potential (more details in SI).[21,22] To avoid any complexity in our SEE measurements, a constant oxidation potential of 0.85 V vs. Pt QRE lower than $E_{1/2}$ (i.e. 1.10 V vs. Pt QRE) was selected. In Figure 2, SEE measurement is schematically illustrated, where a Pt UME applied with a constant potential of 0.85 V vs. Pt QRE is immersed in the aqueous solution containing both 2-ABP at a concentration lower than µM and freshly prepared NEs. This aqueous solution was vortexed for 15 min once NEs were added and left on the benchtop for 2 hrs prior to SEE measurements to

ensure the system under the equilibrium. 2-ABP concentration in the aqueous bulk solution is too low to give any substantial background current in the current-time (i-t) response during SEE measurements. NEs partitioned with 2-ABP spontaneously diffuse and collide onto a Pt UME, where an oxidative potential is applied. Upon a collision of an individual NE to a Pt UME, 2-ABP partitioned in (or, at) a NE is immediately oxidized leading to anodic currents, which decay over time due to the depletion of 2-ABP in (or, at) a NE, thereby showing a current spike upon an individual collision of a NE. The integration of a current spike over time gives charges needed for electrolysis of 2-ABP, thus an amount of 2-ABP partitioned in (or, at) a NE. Particularly, the high monodispersity of NEs allows us to consider their volume constant, and to estimate a concentration of 2-ABP in (or, at) an individual NE.

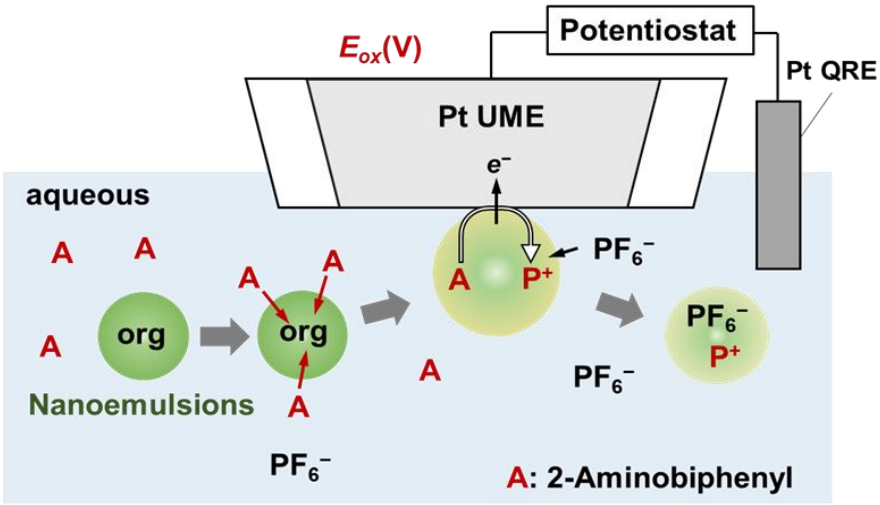

Figure 3.2 A scheme of SEE measurements. NEs partitioned with 2-ABP spontaneously diffuse in the aqueous bulk solution containing a low concentration of 2-ABP, and collide onto a Pt UME applied with a constant oxidative potential, E_{ox} = 0.85 V vs. Pt QRE. Upon a collision of an individual NE,2-ABP partitioned in(or, at a NE) is electrolyzed leading to an anodic current flow, During this electrolysis, an anion, PF_6^- in aqueoss phase is tresferred in to the NE to maintain the electroneutrality inside a NE. Aqueous solution contain 10 mM NH_4PF_6 as a supporting electrolyte.

Herein, we performed three sets of SEE measurements in the presence of three different concentrations of NEs, such as 8.0 pM, 0.8 pM, or 80 fM. In each set of SEE measurements, the concentration of 2-ABP in aqueous solution varied about three orders of magnitudes. The first set of SEE was performed in the presence of 8 pM of NEs with the concentration of 2-ABP at from 5.0 μM to 0.1 μM. For example, with 8 pM of NEs and 5.0 μM 2-ABP in aqueous solution, i-t curve was obtained with a series of current spikes showing nearly uniform current magnitudes (Figure 3.2A). Each current spike showed a characteristic decay with time. This collisional response, i-t decay was fitted with bulk electrolysis model, assuming that 2-ABP is partitioned, diffuses in the castor oil inside a NE, and undergoes an electrolytic reaction at a contact point between a NE and a Pt UME (See SI for more details). In Figure 3A inlets, a good agreement between the experimental i-t curve (black solid lines) and the simulation (red open circles) is obtained, which evidently indicates that partitioned 2-ABP resides in a NE filled with castor oil, not on the surface of a NE. Thereby, the partitioning of 2-ABP with NEs is mainly governed by the extraction process not the adsorption. It should be noted that in situ measurements by SEE uniquely prove this strong evidence of extraction as a governing process in partitioning of delivery compounds with NEs, which cannot be explicitly elucidated by other ex situ techniques such as HPLC or spectrophotometry.

Continuously, charges from integrated current spikes were collected to construct a concentration distribution of 2-ABP partitioned in NEs. Current spikes at least 3 times larger than the background noise signal were counted for this analysis. Note that SEE responses are independent with size of NEs due to the high monodispersity, thereby a variation of charges in SEE measurements is mainly caused by a variation of 2-ABP

amount partitioned in a NE. Using a constant radius, 19 nm of monodisperse NEs (r_{NE}) determined by TEM and DLS, and the integrated charge (Q) from i-t curve, the concentration of 2-ABP partitioned in a NE, C_{ABP}^{NE} is calculated by[17]

$$C_{ABP}^{NE} = \frac{3Q}{4\pi F r_{NE}^3} \quad (1)$$

where *F* is Faraday constant (96485 C/mol).

The overall distribution of C_{ABP}^{NE} estimated from current spikes (Figure 3.3A), is illustrated in Figure 3B. The resultant C_{ABP}^{NE} ranges 14.0 ~ 17.0 M with a peak at 15.5 M, which is consistent with the maximum capacity of given NEs, 15.8 M for ferrocene determined by our previous work. Notably, a narrow distribution of $C_{ABP}^{NE}$was observed, which could be attributed to the fully equilibrated system as well as monodisperse NEs. This equilibrated system along with the unique combination of SEE and the highly monodisperse NEs, is advantageous to attain the high accuracy and precision in our analysis, since repetitive measurements of similar NEs can be made during SEE. This new analytical aspect is distinct compared to the general scope of conventional SEE applications with polydisperse NEs limited to a discrete size distribution of NEs.

Further, 2-ABP concentration in aqueous solution was sequentially decreased up to 0.1 μM in the presence of 8 pM NEs, and the subsequent SEE was performed. The respective C_{ABP}^{NE} values were estimated from each *i-t* curve, and the corresponding concentration distribution curves were constructed in the same manner as aforementioned (data not shown). Overall, as 2-ABP concentration in aqueous solution decreases from 5.0 μM to 0.1 μM under 8 pM NEs, the C_{ABP}^{NE} peak value linearly decreases from 15.5 M to 0.5 M (Figure 4). We will discuss more details in the later section.

Likewise, another set of SEE were performed in the presence of 0.8 pM of NEs with 2-ABP concentration at from 1.0 μM to 10 nM. In Figure 3.3C, a typical *i-t* curve with 0.8 pM NEs and 0.3 μM 2-ABP is illustrated. Current spikes fitted well with bulk electrolysis model indicating a partitioning of 2-ABP via extraction inside a NE (insets in Figure

3.3C). Based on the charges integrated from each current spike and eq (1), the distribution curve of C_{ABP}^{NE} was constructed, narrowly spanning between 12.0 and 18.0 M with a peak at 15.5 M (Figure 3.3D). Note that NEs could hold 2-ABP with a maximum capacity under this given condition as well. In addition, as the concentration of 2-ABP in aqueous solution sequentially decreases from 1.0 μM to 10 nM under 0.8 pM NEs, a linear decrease in C_{ABP}^{NE} peak values is observed ranging from 15.5 M to 0.5 M similar to the case with 8 pM NEs (Figure 3.4).

The final set of SEE measurements was performed in the presence of 80 fM of NEs with 2-ABP concentration at from 0.1 μM to 1.0 nM. As shown in Figure 3E with 80 fM NEs and 30 nM 2-ABP, a characteristic *i-t* curve is observed. Each current spike follows bulk electrolysis model implying a partitioning of 2-ABP via extraction inside a NE as well (insets in Figure 3.3E). The subsequent distribution curve of C_{ABP}^{NE} shows a narrow width between 12.0 and 17.0 M with a peak at 15.5 M (Figure 3.3F). When 2-ABP concentration in aqueous solution decreased up to 1.0 nM in the presence of 80 fM NEs, the respective SEE measurements gave a subsequent C_{ABP}^{NE} peak value, 0.9 (±0.4) M (Figure S4). Overall, a linear decrease in C_{ABP}^{NE} peak values from 15.5 M to 0.9 M is also obtained, as the 2-ABP concentration in aqueous solution sequentially decreases from 0.1 μM to 1.0 nM under 80 fM NEs (Figure 3.4).

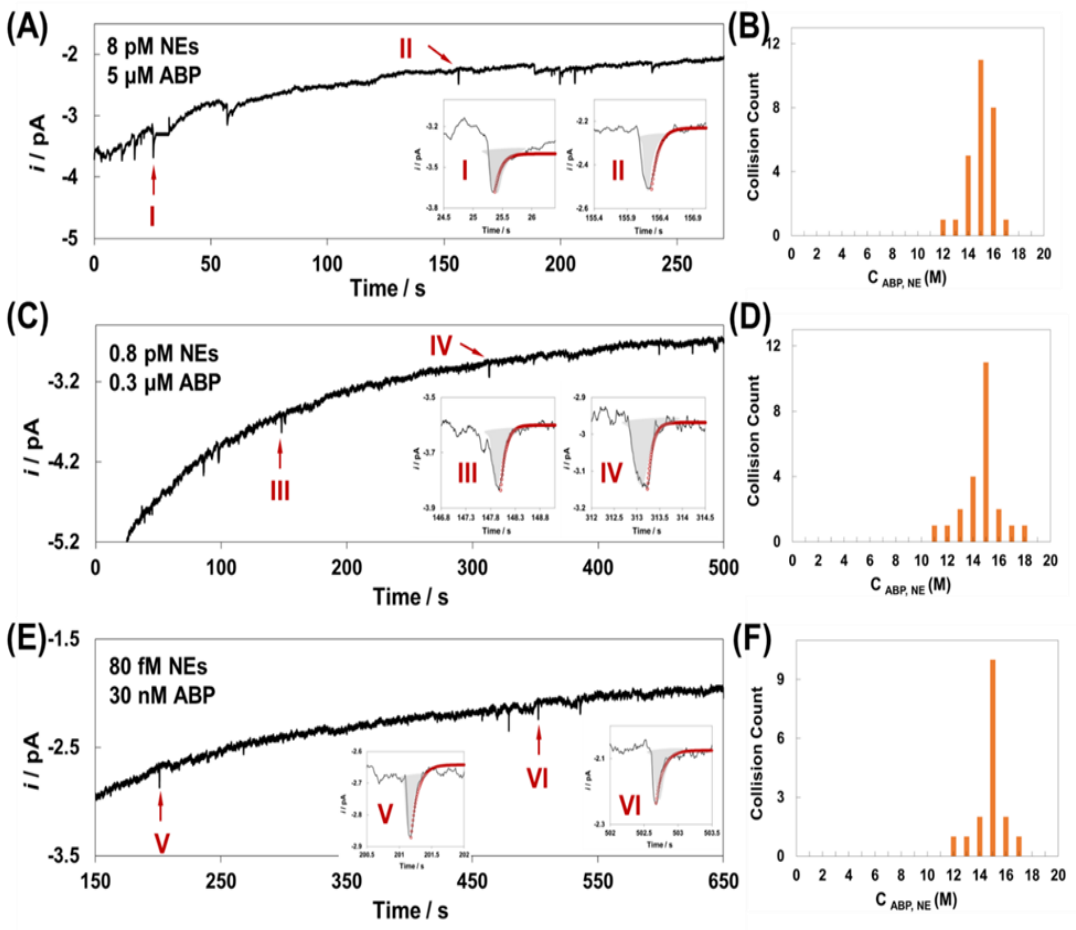

Figure 3.3 (A), (C), (E) *I-t* curves of NE collisions at Pt UME under 0.85 V vs Pt QRE with (8 pM NEs+ 5 μM 2-ABP), (0.8 pM NEs + 0.3 μM 2-ABP), and (80 fM NEs+ 30 nM 2-ABP), respectively. Each inset shows a comparison between experimental current spike (black solid lines) and simulated one (red open circles) based on the bulk electrolysis model. (B), (D), (F) Concentration distribution curves of 2-ABP partitioned in NEs, $\boldsymbol{C_{ABP}^{NE}}$ from the corresponding SEE data.

The Partition Coefficient at NEs and Its Validation by the Molecular Simulation.

Finally, we could construct a plot of C_{ABP}^{NE} vs. total concentration of 2-ABP, C_{ABP}^{tot} by combining all the C_{ABP}^{NE} peak values from three sets of SEE data (Figure 3.4). Three linear curves were obtained with respectively different slopes (determined by the least square regression).

Here, we formulate the relationship between C_{ABP}^{NE} and C_{ABP}^{tot} by considering the following equilibrium constant and the mass balances. When 2-ABP is partitioned from water to organic phase of DOS in NEs,

$$2-ABP\ (aq)\ \rightleftarrows 2-ABP\ (NE) \quad (2)$$

$$P = \frac{C_{ABP}^{NE}}{C_{ABP}^{aq}} \quad (3)$$

where the equilibrium constant (or, partition coefficient) is *P*, C_{ABP}^{NE} is the concentration of 2-ABP partitioned into NE, C_{ABP}^{aq} is the concentration of 2-ABP remaining in aqueous phase.

According to the law of mass conservation,

$$n_{ABP}^{tot} = n_{ABP}^{NE} + n_{ABP}^{aq} \quad (4)$$

where $n_{ABP}^{tot}, n_{ABP}^{NE},$ and n_{ABP}^{aq} are the number of moles of ABP in the total system, in the NE phase, and remaining in the aqueous phase, respectively.

Eq (4) can be reformulated with concentrations of 2-ABP and volumes of the corresponding phases as below,

$$C_{ABP}^{tot}V_{tot} = C_{ABP}^{NE}V_{NE} + C_{ABP}^{aq}V_{aq} \quad (5)$$

Using eq (3) and eq (5), an implicit equation relating C_{ABP}^{NE} with C_{ABP}^{tot} is obtained as below,

$$C_{ABP}^{NE} = \left[\frac{V_{total}}{\frac{V_{aq}}{P}+V_{NE}}\right] \cdot C_{ABP}^{tot} \quad (6)$$

This relationship, eq (6) is readily used to extract the partition coefficient, *P* with experimentally estimated C_{ABP}^{NE} from the readout of SEE measurements under a series of various C_{ABP}^{tot}. Using three slopes in Figure 4, the respective experimental values (i.e. V_{total}, V_{aq}, and V_{NE}), and eq (6), the partition coefficient, *P* could be determined as 1.9 (± 1.4) × 10^{10} (detailed parameters are in SI). In fact, one could evaluate a *P* from one point measurement of SEE under one particular condition, thus estimating C_{ABP}^{NE} value and the corresponding C_{ABP}^{aq} mathematically calculated by eq (3) and eq (5). This one point

measurement, however, provides a *P* with low accuracy. Contrarily, sets of measurements enable to construct an analogy of calibration curves and improve accuracy and precision to determine the *P*, thus attaining the *P* value consistent over wide concentration ranges of 2-ABP as well as NEs.

The *P* determined by SEE measurements is ~7 orders of magnitude higher than the reported partition coefficient of 2-ABP between two phases, octanol and water (*P* = 691.8).[19] Considering similar level of dielectric constants of two organic solvents, octanol and DOS, this *P* determined for NEs is quite surprising. Owing to the unprecedentedly large *P*, the extraction by NEs is markedly efficient to reach ~8 orders of magnitude for the preconcentration factor. This exceptional *P* implies an additional stabilization of partitioned 2-ABP in NEs via the intermolecular interaction between 2-ABP and DOS in NEs. Indeed, the equilibrium constant (e.g. molecular recognition, binding, or catalysis) are often mediated by non-covalent interaction involving aromatic functional groups.[23] Particularly, lone pair–π (or referred to as n to π*) interaction is ascribed to such a stabilizing association between a lone pair of electrons and the face of a π system.[23] Although it is individually expected to quite weak, the significance of the lone pair–π interaction has been noted along with other non-covalent interaction such as hydrogen bonding.[24,25]This interaction energy values are attractive and moderately strong, ranging from −11.3 to −94.5 kJ/mol.[26] In our partitioned system, the carbonyl oxygen of DOS is in close proximity to the aromatic centers of 2-ABP, thereby the interaction between regions of negative (the lone pair) and positive (electron deficient π system on the aromatic ring) can be understood as electrostatic potential (Figure 3.5). We performed the molecular simulation, and calculated the interaction between 2-ABP and DOS molecule (see SI).

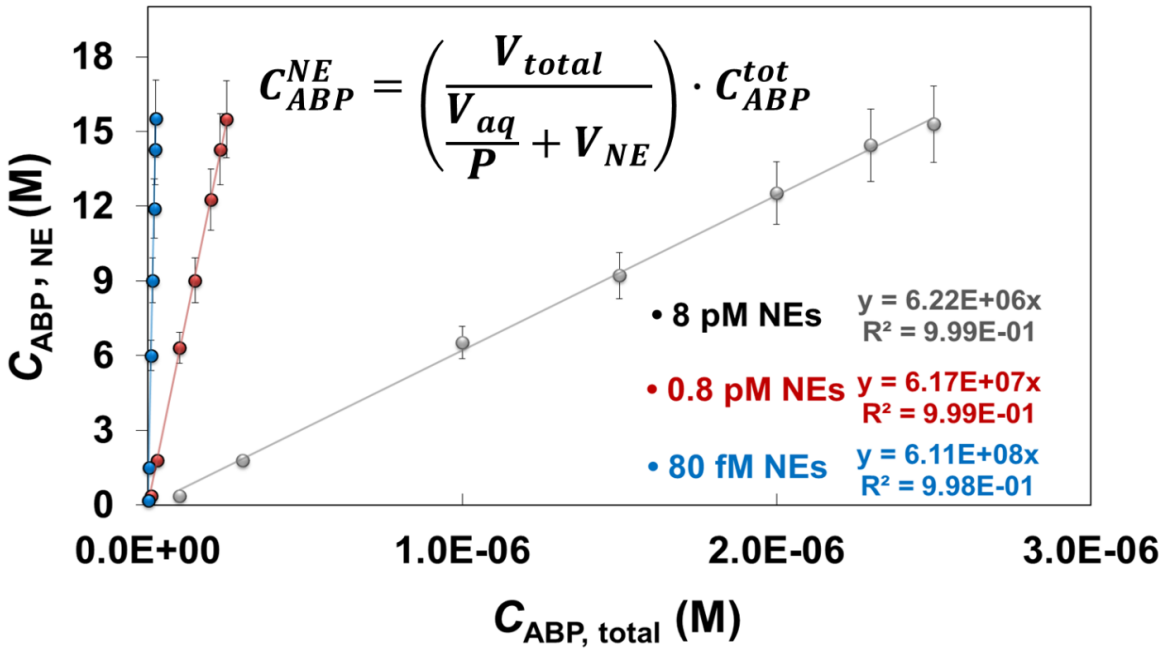

Figure 3.4 A plot of C_{ABP}^{NE} vs. C_{ABP}^{tot} in the presence of various concentration of NEs, 8 pM (black closed circles), 0.8 pM (red closed circles), and 80 fM (blue closed circles). The respective slopes and squared correlation coefficients, R^2 from the least square regression are shown in the bottom right.

Based on our simulation, the interactions from these contacts are found to be favorable and stable with $\Delta G° = -11.7$ kJ/mol. To incorporate this stabilization energy into apparent partition coefficient, we consider a partitioning process of 2-ABP into NEs as two consecutive reactions, where 2-ABP partitioned into a NE undergoes a subsequent complexation with DOS molecules via non-covalent interaction.

$$2-ABP\,(aq) \rightleftarrows 2-ABP\,(NE) \quad (7)$$

$$p2-ABP\,(NE) + qDOS(NE) \longrightarrow (2-ABP)_p \cdot (DOS\,(NE))_q \quad (8)$$

where the equilibrium constant, *K* for eq (7) is expressed by,

$$K = \frac{C_{ABP,NE}}{C_{ABP,aq}} = \sim 691.8 \quad (9)$$

and the complex formation constant, β for eq (8) is

$$\beta = \frac{C_{ABP \cdot DOS}}{C_{ABP,NE}^{p} \cdot C_{DOS}^{q}} \approx \frac{C_{ABP \cdot DOS}}{C_{ABP,NE}^{p}} = \exp(-\Delta G^{0}/RT) \quad (10)$$

where DOS is a pure solvent in NE phase, thus a concentration of DOS, C_{DOS} is considered as unity.

Thereby, the apparent partition coefficient can be expressed by,

$$P_{app} = \frac{total\ concentration\ of\ ABP\ in\ NE}{total\ concentration\ of\ ABP\ in\ aq} = K \cdot \beta \quad (11)$$

To obtain P_{app} consistent with the experimentally determined P (=1.9 (± 1.4) × 10^{10}), β should be at least 3.0 × 10^{7}. Using eq (10) and (11), the anticipated $\Delta G°$ for the stabilized complex in NEs would be −42.6 kJ/mol. Although it is not clear to know the exact stoichiometry ratio of *p*/*q*, this anticipated $\Delta G°$ is in the reasonable range between −11.3 and −94.5 kJ/mol.[26] Since 1:1 interaction between 2-ABP and DOS molecule results in $\Delta G°$ = −11.7 kJ/mol, a collective contribution from the interaction between multiple molecules could be considered rationally (see more details in SI). Therefore, our calculations support the idea that the intermolecular interaction between the carbonyl oxygens in DOS and the aromatic center of 2-ABP as well as hydrogen bonding could play a stabilizing role in partitioned structures inside NEs, thus leading to a remarkably high partition coefficient.

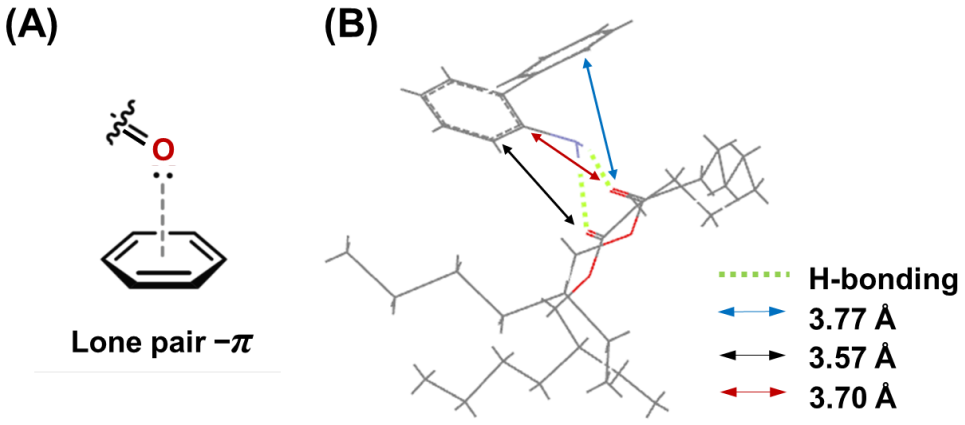

Figure 3.5 (A) Interaction of lone pair and π system. (B) Geometry optimized structure of 2-ABP with DOS molecule: lone pair–π interaction (red, blue and black arrows) with hydrogen bonding (green dotted line).

CONCLUSIONS

In conclusions, we could successfully employ SEE to measure the partition coefficient at intact NEs in situ, thus exhibiting a practical insight in SEE. The direct and in-situ measurements of extracted 2-ABP from water to Pluronic F-127 based NEs were enabled via electrochemical oxidation upon the collision of each individual NE onto Pt UME. The unprecedentedly large preconcentration factor as ~8 orders of magnitude could be obtained, thus resulting in partition coefficient of 1.9 (± 1.4) × 10^{10}. This large partition coefficient could be attributed to the intermolecular interaction in NEs, which was quantitatively validated by the molecular simulations. It should be noted that the high monodispersity of NEs in this study allows for high precision and accuracy in our measurements. Significantly, our approach is readily applicable to investigate practical NEs commercially available for drug, food, and cosmetics.

REFERENCES

1. Lovelnm C.; Attama, A. A., "Current state of Nanoemulsions in Drug Delivery", *J. Biomater. Nanobiotechnol.,* **2011**, 2, 626-639.

2. Tadros, T.; Izquierdo, P.; Esquena, J.; Solans, C., "Formation and Stability of Nanoemulsions", *Advances in Colloids and Interface Science*, **2004**, V108-109, 303-318.

3. Abooofazeli, R., "Nanometric Scaled Emulsions (Nanoemulsions)", *Iran. J. Pharm. Res.,* **2010**, 9, 325-326

4. Lucy, C. A.; Harris, D. C., Quantitative Chemical Analysis, 9th Ed., 2016, W. H. Freeman and Company.

5. Ganra, S.; Talejar, M.; Singh, A.; Coleman, T. P.; Amiji, M. M., "Nanoemulsions in Translational Research – Opportunities and Challenges in Targeted Cancer Therapy", *AAPS PharmaSciTech*, **2014**, 15, 694-708.

6. Lallenmad, F.; Daull, P.; Benita, S.; Buggage, R.; Garrigue, J-S., "Successfully Improving Ocular Drug Delivery Using the Cationic Nanoemulsion, Novasorb", *J. Drug Delivery*, **2012**, 1-16.

7. Varshney, M.; Morey, T. E.; Shah, D. O.; Flint, J. A.; Moudgil, B. M.; Seubert, C. N.; Dennis, D. M., " Pluronic Microemulsions as Nanoreserviors for Extraction of Bupivacaine from Normal Saline", *J. Am. Chem. Soc*., 2004, 126, 5108-5112.

8. Liu, C-H.; Lai, K-Y.; Chen, Y-J.; Lee, W-S.; Hsu, C-Y., "In Vitro Scleral Lutein Distribution by Cyclodextrin Containing Nanoemulsions", *Chem. Pharm. Bull*., **2015**, 63, 59-67.

9. Singh, K. K.; Vingkar, S. K., "Formulation, Antimalarial Activity and Biodistribution of Oral Lipid Nanoemulsion of Primaquine", *Int. J. Pharm.*, **2008**, 347, 136-143.

10. Ahmad J, F.; Ali, M.; Shekel, F.; Talegaonakr, C.; Khar K, R.; Shafig, S., "Investigation of Nanoemulsion System for Transdermal Delivery of Domperidone: Ex-vivo and in vivo Studies", **2008**, *Current Nanoscience*, 4, 381-390.

11. Srilatha, R.; Aparna, C.; Srinivas, P.; Sadanandam, M., "Formulation, Evaluation and Characterization of Glipizide Nanoemulsions", *Asian J. Pharm. Clin. Res.*, **2013**, 6, 66-71.

12 . Bhagav, P.; Upadhay, H.; Chandra, S., "Brimonidine Tartrate Eudragit Long-acting Nanoparticle: Formulation, Optimization, *in vitro* and *in vivo* Evaluation", *AAPS PharmSciTech,* **2011**, 12, 1087-1101.

13 . Barker, A. L.; Macpherson, J. V.; Slevin, C. J.; Unwin, P. R., "Scanning Electrochemical Microscopy (SECM) as a Probe of Transfer Processes in Two-Phase Systems: Theory and Experimental Applications of SECM-Induced Transfer with Arbitrary Partition Coefficients, Diffusion Coefficients, and Interfacial Kinetics", *J. Phys. Chem. B,* **1998**, 102, 1586-1598.

14 . Knotturi, K.; Murtomäki, L., "Electrochemical Determination of Partition Coefficients of Drugs", *J. Pharmaceutical Sci.,* **1992**, 81, 970-975.

15. https://ascendiapharma.com/technologies/emulsol/

16 . Sabaragamuwe, S. G.; Conti, D.; Puri, S. R.; Andreu, I.; Kim, J, "Single-Entity Electrochemistry of Nanoemulsions: The Nanostructrual Effect on Its Electrochemical Behavior", *Anal. Chem.,* **2019**, 91, 9599-9607.

17 . Kim, B-K.; Boika, A.; Kim, J.; Dick, J. E.; Bard. A. J.," Characterizing Emulsions by Observation of Single Droplet Collisions: Attoliter Electrochemical Reactors", *J. Am. Chem. Soc.,* **2014**, 136, 4849-4852.

18 . Xie, X.; Zhai, J.; Crespo, G.; Bakker, E., "Ionophore-Based Ion Sensitive Optical NanoSensors Operating in Exhaustive Sensing Mode", *Anal. Chem.,* **2014**, 86, 8770-8775.

19 . Xie, X.; Zhai, J.; Bakker, E., "pH Independent Nano-Optode Sensors Based on Exhaustive Ion-Selective Nanospheres", *Anal. Chem.,* **2014**, 86, 2853-2856.

20 . Hansch, C., Leo, A., D. Hoekman. Exploring QSAR - Hydrophobic, Electronic, and Steric Constants. Washington, DC: American Chemical Society., **1995**, p. 98

21 R. N. Adams, Electrochemistry at Solid Electrodes, Marcel Dekker, New York, NY (1969).

22. V. Vyskocil, J. Barek, Curr. *Org. Chem.*, **2001**, 15, 3059.

23. Neel, A. J.; Hilton, M. J.; Sigman, M. S.; Tosste, F. D., "Exploiting Non-Covalent π Interactions for Catalyst Design", *Nature*, **2017**, 543, 637-646.

24 . Singh, S. K.; Kumar, S.; Das, A., "Competition between n□π(Ar)* and Conventional Hydrogen Bonding (N−H···H) Interactions: an ab initio Study of the Complexes of 7-azaindole and fluorosubstituted pyridines", *Phys. Chem. Chem. Phys*., **2014**, 16, 8819-8827.

25. Ao, M-Z.; Tao, Z-Q.; Liu, H-X.; Wu, D-Y.; Wang, X., "A Theoretical Investigation of the Competition between Hydrogen Bonding and Lone Pair···π Interaction in Complexes of TNT with NH3", *Comput. Theor. Chem.*, **2015**, 1064, 25-34.

26. Frontera, A.; Bauzá, A., "Concurrent Aerogen Bonding and Lone Pair/Anion−π Interactions in the Stability of Organoxenon Derivatives: a Combined CSD and ab initio Study", *Phys. Chem. Chem. Phys.*, **2017**, 19, 30063-30068.

CHAPTER 4

TOWARDS ULTRALOW DETECTION LIMITS OF AROMATIC TOXICANTS IN WATER USING PLURONIC NANOEMULSIONS AND SINGLE-ENTITY ELECTROCHEMISTRY

Shashika Gunathilaka Sabaragamuwe[1], Hiranya Madawala[1], Surendra Raj Puri[1], Jiyeon Kim[1]*

[1]. Department of Chemistry, University of Rhode Island, Kingston, RI, 02881

This manuscript is formatted for publication according *Analytica Chimica Acta* standards and currently under review.

CHAPTER 04

TOWARDS ULTRALOW DETECTION LIMITS OF AROMATIC TOXICANTS IN WATER USING PLURONIC NANOEMULSIONS AND SINGLE-ENTITY ELECTROCHEMISTRY

Shashika Gunathilaka Sabaragamuwe[1], Hiranya Madawala[1], Surendra Raj Puri[1], Jiyeon Kim[1]*

[1]. Department of Chemistry, University of Rhode Island, Kingston, RI, 02881

ABSTRCT

We demonstrate a new electroanalytical technique using nanoemulsions (NEs) as a nanoextractor combined with single entity electrochemistry (SEE) to separate, preconcentrate analytes from bulk media, and even detect them in situ, enabling ultratrace level analysis. This approach is based on our hypothesis that the custom-designed NEs would enable to effectively scavenge compounds from bulk media. Herein, we use Pluronic F-127 functionalized NEs to extract, preconcentrate target analytes e.g. ferrocene derivatives as a model aromatic toxicant dissolved in the water, and employ SEE to in situ detect and quantitatively estimate analytes extracted in individual NEs. Extraction was markedly efficient to reach ~8 orders of magnitude of preconcentration factor under the true equilibrium, thereby enabling ultratrace level analysis with a detection limit of ~0.2 ppb. The key step to attain high sensitivity in our measurements was to modulate the total amount of added NEs respect to the total volume of bulk

solution, thereby controlling the extracted amount of analytes in each NE. Our approach is readily applicable to investigate other aromatic toxicants dissolved in the water, thus detecting hazardous carcinogen, 2-aminobiphenyl in the water up to ~0.1 ppb level. Given the excellent detection performance as well as the broad applicability for ubiquitous aromatic contaminants, the combination of NEs with SEE offers great prospects as a sensor for environmental applications.

INTRODUCTION

The global concern about the water quality and its contamination in the environment has been drastically growing as industrialized nations and developing countries have exploded with abundance in recent years.[1] Particularly, water contamination by aromatic toxicants (or polycyclic aromatic hydrocarbons, PAH) is critical, since they are ubiquitous as byproducts of combustion process as well as a natural component of fossil fuels.[2] Despite low concentration in water due to the low solubility, aromatic toxicants accumulate in sediment, soil and aquatic organisms, thus leaching out and finally leading to bioaccumulate / biomagnify in the food chain.[3] Indeed, PAH have been found at the level of 0.17 μM in the breast milk of nursing mothers living in oil spill affected regions.[4] The potential health effects of aromatic toxicants include the disruption of pulmonary, gastrointestinal, renal, and dermatologic systems, ending to a cancer.[5] Currently, the U.S. Environmental Protection Agency (EPA) declares 0.2 − 0.4 ppb PAH in drinking water. [6] Due to the carcinogenicity, the ultratrace level analysis of aromatic toxicants in water is significant for a public health perspective. Gas[7] or liquid chromatography[8] combined with either mass spectrometry (MS)[9] or fluorescence (or UV-Vis) spectroscopy[10] is commonly

used techniques with high sensitivity, [2] whereas they require high purchase / running costs, and a skilled operator with laborious and time consuming work.[11] Considering the importance of high throughput assays with an easy access, the advancement in analytical system offering high sensitivity, rapidity, miniaturizability (or portability), and accessibility within reasonable costs is ultimately demanded. For the advancement in these analytical processes, we introduce nanoemulsions (NEs) as a new turning point. NEs are oil-in-water (o/w) emulsions with mean droplet diameters ranging from 50 to 500 nm.[12] Owing to the small size and the hydrophobic environment inside NEs, NEs can be a suitable strategy for an efficient extractor of lipophilic analytes. We recently studied NEs functionalized with triblock copolymer, Pluronic F-127 having c.a. 40 nm diameter with a high monodispersity,[13] and measured a partition coefficient at intact NEs in situ, which is remarkably large as ~1.9×10^{10} as a result of both thermodynamic distribution and intermolecular interaction of extracted compounds in the partitioned system.[14] The resultant extraction was markedly efficient to reach ~8 orders of magnitude for the preconcentration factor. Herein, we utilize these key physicochemical properties to make an attractive attempt that NEs are used for both separation of analytes from environments and preconcentration in situ. Additionally, the fast mass transport of analytes to NEs is anticipated due to a small size of NEs, leading to true equilibrium in the given system. In fact, the ability of nanoparticles to remove or separate toxic compounds from subsurface or environments in situ, rapidly, and efficiently at a reasonable price has been extensively explored.[15] Such attempts have been only focused on solid nanoparticles with high adsorption capacity as such or chemically functionalized.[16] And yet, these nanoparticles are combined with conventional analytical methods, e.g. inductively coupled plasma

atomic absorption (or emission) spectrometry (ICP-AAS, or ICP-AES), ICP-MS, or high performance liquid chromatography (HPLC), while effective, very often costly and time consuming.[15]

Innovatively, we combine Pluronic F-127 functionalized NEs with single entity electrochemistry (SEE) to in situ separate, preconcentrate, and even detect analytes at ultratrace level. This unique combination provides distinct analytical merits. First, NEs as an efficient nanoextractor enable ultrasensitive analysis with ultralow detection limit via extraction and preconcentration in situ without additional sample treatment. Second, the application of SEE allows for in situ detection of discrete NEs preconcentrating analytes using a simple instrumentation. Thereby, we can attain ultrahigh sensitivity, rapidity, miniaturizability, and easy accessibility in this analysis.

Herein, we systematically vary the concentrations of ferrocenemethanol (FcMeOH) as a model aromatic toxicant and NEs in aqueous bulk solution, perform SEE measurements to construct a calibration curve, thus quantitatively establishing a new analytical method. Throughout blind sample tests, the analytical capability of this method is further validated. Also, our ultrasensitive analysis is readily applicable to other aromatic toxicants such as 2-aminobiphenyl (2-ABP), a typical carcinogen.[17] Notably, this demonstrated application of NEs and SEE opens up a new route to ultratrace level analysis for environmental pollutants in water, whereas SEE has been widely applied to study single events, and discretely characterize size distribution of polydisperse soft particles including NEs as opposed to ensemble measurements.[18]

EXPERIMENTAL SECTION

Chemicals.

Pluronic F-127 (F-127), bis(2-ethylhexyl)- sebacate (DOS, 97.0%), tetrahydrofuran (THF, 99.9%), Ferrocene Methanol (FcMeOH, 97.0%), potassium tetrakis (pentafluorophenyl) borate (KTHPB, 97.0%), ammonium hexafluorophosphate (NH4PF6, 99.98%), ammonium chloride (NH4Cl, 99.5%) and potassium nitrate (KNO_3, 99.0%) were purchased from Sigma-Aldrich used as obtained. Uranyless negative stain, and glass vials were purchased from Fisher Scientifics. Nanopure water (18.2 MΩ·cm, TOC 2 ppb; Milli-Q Integral 5 system, Millipore) was used to prepare all the aqueous electrolyte solutions as well as in NE synthesis.

Synthesis of Nanoemulsions.

NEs were synthesized by dissolving 1.8 mg of KTHPB and 250.0 mg of F127 in 3.0 mL of THF to form a homogeneous solution. Then, 8.8 μL of DOS was added to this solution. Resulting solution was vortexed for 1 hour using a vortex mixer (Fisher Scientific, Pittsburgh, PA) at a spinning speed of 3000 rpm. After mixing, 0.1 ml of the solution was forcefully injected into 4.0 mL of deionized water on a vortex with a spinning speed of 4000 rpm for 2 minutes. This process was repeated for another batch. The resulting 8 mL solution was then combined, and further homogenized for 2 min at a rate of 4900 rpm using homogenizer (Kinematica AG, Polytron system PT 10-35 GT, Switzerland). Finally, the resulting solution was purged with N2 gas to fully evaporate

THF for 1 hour under a flow rate of 40 psi. After evaporation, the final solution was used as a NE stock solution.

Measuring the Size and Zeta Potential of Nanoemulsions.

NEs were characterized by the dynamic light scattering (DLS) to measure the size distribution and ζ-potential (Malvern Zetasizer Nano ZS, Malvern Instruments Inc., MA). Measurements were taken at 90◦ angle for NEs. For the DLS sample preparation, 1.0 mL of NE stock solution was diluted with 3.0 mL of nanopure water, and a 1.0 mL aliquot of this diluted solution was taken to fill a DLS cuvette (Malvern DTS 1070, Malvern Instruments Inc., MA). DLS measurements were performed at 25 °C.

Fabrication of a Pt UME.

Pt UME (5 μm diameter) was fabricated using CO_2−laser capillary puller (model P-2000, Sutter Instrument). First, 25 μm dia. Pt wire (Goodfellow, annealed) was inserted in a borosilicate capillary (I.D. 0.2 mm, O.D. 1mm, item No 9-000-2000, Drummond scientific company, Broomall, PA) and was pulled together with CO_2−laser puller. An as pulled Pt UME was milled by a homemade polisher to expose Pt disk resulting in an inlaid disk-shaped electrode. Then, the Pt UME was cleaned in piranha solution for 10s, followed by through rinsing in water. Prepared Pt UMEs were also used under 30 % or higher relative humidity at 22~23 °C.

SEE Measurements.

SEE was performed in a two-electrode cell using a bipotentiostat (CHI 760E or CHM8022D, CH Instrument, Austin, TX) at ambient temperature (20 °C). Pt UME (5 μm diameter) was immersed in the aqueous solution containing 10 mM NH_4PF_6 as the supporting electrolyte. Prior to SEE measurements, aqueous solution with added NEs was

vortexed for 15 min at 1000 rpm, and left on the benchtop for 2 hrs. Amperometric current was measured over time under a constantly applied potential of 0.40 V or 0.85 V vs a Pt quasi-reference electrode (Pt QRE) to oxidize FcMeOH or 2-ABP extracted inside NEs from the bulk media, respectively. The time interval for data acquisition was 5−10 ms.

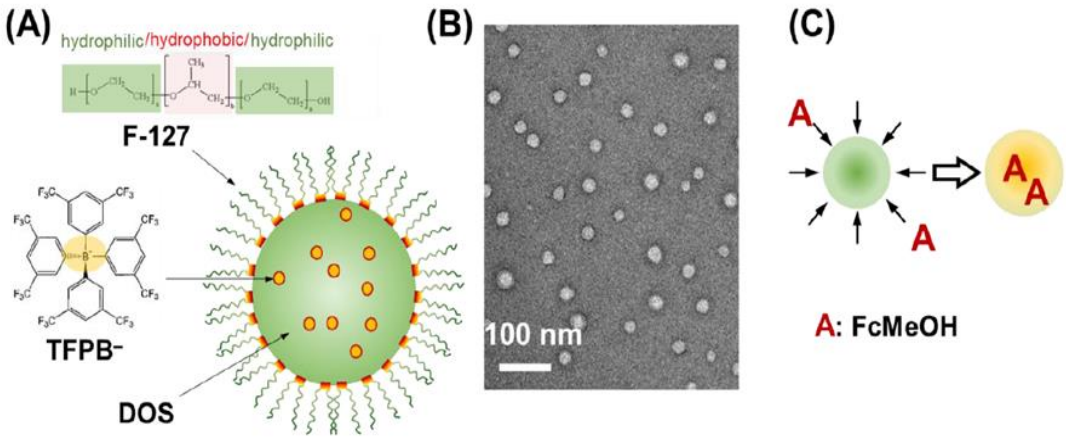

Figure 4.1 (A) A schematic illustration of NE composed of triblock polymer (F-127), ion exchanger ($TFPB^-$), and dioctyl sebacate oil (DOS). (B) TEM image of monodispersed NEs with 40 nm diameter. (C) Diffusion-limited loading of a NE with analytes, e.g. FcMeOH.

RESULTS AND DISCUSSION

Nanoemulsions with High Monodispersity and a Large Partition Coefficient.

We utilized NEs functionalized with amphiphilic block copolymer (Pluronic F-127) and castor oil plasticizer (Figure 4.1A). In earlier works, we elucidated important physicochemical properties of these NEs such as size, electrochemical activity relevant to the intrinsic inner structure, and the partition coefficient. Here, we selected NEs with the optimized composition showing 40 (± 5) nm diameter with high monodispersity, high electroactivity, and high partition coefficient.[13,14] As shown in Figure 1B, the high monodispersity was observed by TEM measurements consistent with dynamic light scattering (DLS) measurements with 38 nm diameter and 0.17 (± 0.05) polydispersity index (PDI) (Figure S1).

Previously, a partition coefficient at intact NEs could be determined as $P = 1.9 \times 10^{10}$ by in situ SEE measurements. The large P for aromatic compounds promises a potential application of NEs as efficient nanoextractors, thereby enabling in situ separation of analytes from environments, and preconcentration inside NEs. In combination with SEE, all three steps of separation by extraction, preconcentration, and even detection of analytes can be studied in situ with a simple instrumentation. Herein, we explore the ability of NEs to remove aromatic toxicants from water, preconcentrate them, thus enabling ultratrace level analysis. FcMeOH is studied as a model aromatic toxicant dissolved in the water, which undergoes extraction, preconcentration, and the electrolysis inside NEs during the electrochemical detection.

Efficient and Rapid Extraction by Nanoemulsions.

The feasibility of new applications of NEs in preconcentration and ultratrace level analysis from the environmental sources relies on how efficiently and rapidly NEs can

extract the target compounds. Owing to the large partition coefficient of NEs, FcMeOH can be effectively partitioned and extracted into a NE from the aqueous bulk solution. The mass transfer of FcMeOH followed by extraction into the NEs readily occurs due to the small dimension of NEs, thereby the extremely short loading time is expected from the high diffusional flux of FcMeOH to a NE (Figure 4.1C). At a steady state, the diffusional flux of FcMeOH to the surface of a spherical NE, *J*, can be estimated as,[19]

$$J = \frac{D_{FcMeOH} C_{FcMeOH}}{r_0} \qquad (1)$$

where D_{FcMeOH} and C_{FcMeOH} are the diffusion coefficient and concentration of FcMeOH in the aqueous sample solution and r_0 is radius of a NE. Assuming that FcMeOH at the NE/solution interface is instantaneously partitioned and extracted, the time required for the diffusion-limited loading of NEs, τ, is given by,[13]

$$\tau = \frac{C_{fill} r_0^2}{3 D_{FcMeOH} C_{FcMeOH.aq}} \qquad (2)$$

where C_{fill} is the filling capacity in a NE with varying from 0.0 to 15.7 M, $C_{FcMeOH,aq}$ is the concentration of FcMeOH in aqueous solution The filling capacity varies depending on the concentration of FcMeOH in aqueous phase and the amount of NEs added in the aqueous bulk solution.

Under the equilibrium, the filling capacity is determined by, [14]

$$C_{fill} = \left[\frac{V_{total}}{\frac{V_{aq}}{P} + V_{NE}}\right] \cdot C_{FcMeOH}^{tot} \approx \left[\frac{V_{total}}{V_{NE}}\right] \cdot C_{FcMeOH}^{tot} \qquad (3)$$

where V_{aq}, V_{NE}, and V_{total} are the volume of aqueous phase, NE phase, and their sum, respectively (Table S1 in SI), and *P* is the partition coefficient at NEs. In our earlier work, the maximum filling capacity of an individual NE was empirically estimated as

15.7 M.[13] Also, our recent work evaluated P (=1.9 × 10^{10}) of intact NEs for aromatic compounds. Due to the large P, the C_{fill} is mainly determined by the volume ratio between V_{total} and V_{NE}, and the total concentration of FcMeOH present in the total solution, C_{FcMeOH}^{tot} under $V_{aq} / P << V_{NE}$. Hence, this implicit eq (3) linearly relates C_{fill} with C_{FcMeOH}^{tot}. Overall, based on the eq (2) and (3), with a diffusion coefficient of FcMeOH as 6 × 10^{-6} cm^2/s, 0.1 to 3.0 μM FcMeOH in the presence of 8 pM NEs in the aqueous solution can be accumulated into each NE to yield ~0.30 to 15.7 M in 600 to 1000 ms, respectively. The expected loading times would be fast enough to perform SEE measurements under the true equilibrium, thereby supporting the feasibility of in situ separation, preconcentration, and detection of analytes (e.g. FcMeOH) from the aqueous bulk solution.

Single Entity Electrochemistry with Individual Nanoemulsions.

In Figure 4.2A, SEE measurement is schematically illustrated, where a Pt UME applied with a constant potential of 0.40 V vs. Pt QRE is immersed in the aqueous solution containing both FcMeOH at a concentration lower than 10 μM and freshly prepared NEs. This aqueous solution was vortexed for 15 min once NEs were added, and left on the benchtop for 2 hrs prior to SEE measurements to ensure the system under the equilibrium. FcMeOH concentration in the aqueous bulk solution is too low to give any substantial background current in the current-time (*i*-*t*) response during SEE measurements. NEs extracting/preconcentrating FcMeOH spontaneously diffuse and collide onto a Pt UME, where an oxidative potential is applied. Upon a collision of an individual NE to a Pt UME, FcMeOH preconcentrated in a NE is immediately oxidized leading to anodic currents, which decay over time due to the depletion of FcMeOH in a NE, thereby showing a current spike upon an individual collision of a NE. The integration of a current spike over time gives charges needed for electrolysis of FcMeOH, thus an amount of FcMeOH extracted/preconcentrated in a NE.

Herein, we performed three sets of SEE measurements in the presence of three different concentrations of NEs, such as 8.0 pM, 0.8 pM, or 80 fM. In each set of SEE measurements, the concentration of FcMeOH in aqueous solution varied about three

orders of magnitudes. The first set of SEE was performed in the presence of 8 pM of NEs with the concentration of FcMeOH at from 10.0 μM to 0.1 μM. For example, with 8 pM of NEs and 10.0 μM FcMeOH in aqueous solution, *i-t* curve was obtained with a series of current spikes showing nearly uniform current magnitudes (Figure 2B). Each current spike showed a characteristic decay with time. This collisional response, *i-t* decay was fitted with bulk electrolysis model,[19] assuming that FcMeOH is extracted, diffuses in the castor oil inside a NE rather than adsorption on NE surface, and undergoes an electrolytic reaction at a contact point between a NE and a Pt UME (See SI for more details). In Figure 4.2B insets, a good agreement between the experimental *i-t* curve (black solid lines) and the simulation (red open circles) is obtained, which evidently indicates that extracted (and preconcentrated) FcMeOH resides in a NE filled with castor oil, not on the surface of a NE.

Continuously, charges from integrated current spikes were collected to construct a size distribution curve of NEs preconcentrating FcMeOH. Current spikes at least 3 times larger than the background noise signal were counted for this analysis. Using the concentration of FcMeOH extracted in a NE determined by eq (3), 15.7 M, and the integrated charge (*Q*) from *i-t* curve, diameter of a NE, *d* is calculated by [13]

$$d = 2\sqrt[3]{\frac{3Q}{4\pi F C_{fill}}} \qquad (4)$$

where *F* is Faraday constant (96485 C/mol).

The discrete size distribution estimated from current spikes in Figure 2B, is illustrated in Figure 4.2C. The resultant *d* ranges 30 ~ 60 nm with a peak at 40 nm, which is consistent with the DLS data. This consistency validates C_{fill} determined by eq (3). Notably, a narrow distribution of *d* could be attributed to the fully equilibrated system as well as intrinsically monodisperse NEs. In addition, this equilibrated system along with the unique combination of SEE and the highly monodisperse NEs, is advantageous to attain the high accuracy and precision in our analysis, since repetitive measurements of similar NEs can be made during SEE.

Further, FcMeOH concentration in aqueous solution was sequentially decreased up to 1.0 μM in the presence of 8 pM NEs, and the subsequent SEE was performed (Figure 4.2D). The respective C_{fill} value, 6.0 M from eq (3) was used to estimate diameter of NEs from each *i-t* curve result and eq (4), and the corresponding size distribution curve was constructed (Figure 4.2E). The resultant *d* ranging 30 ~ 50 nm with a peak at 40 nm showed good consistency with the DLS data, which validates C_{fill} determined by eq (3) as well.

Likewise, another SEE was performed in the presence of 8 pM of NEs with FcMeOH concentration at 0.1 μM. In Figure 4.2F, a typical *i-t* curve with 8 pM NEs and 0.1 μM FcMeOH is illustrated. Current spikes fitted well with bulk electrolysis model indicating an extraction of FcMeOH inside a NE (insets in Figure 4.2F). Based on the charges integrated from each current spike and eq (4) as well as the C_{fill} as 0.60 M using eq (3), the size distribution curve was constructed, narrowly spanning between 40 and 70 nm with a peak at 50 nm (Figure 4.2G). Since the current spikes under this condition are close to the limit of detection in our measurements, charges integrated from *i-t* curve tend to be slightly overestimated, thus leading to the larger mean diameter of NEs, 50 nm. Overall, as FcMeOH concentration in aqueous solution decreases from 10.0 μM to 0.1 μM in the presence of 8 pM NEs, the C_{fill} validated by SEE measurements linearly decreases from 15.7 M to 0.6 M as expected under the fully equilibrated system.

Two more sets of SEE measurements were performed under 1 μM − 10 nM FcMeOH with 0.8 pM NEs, and 0.1 μM − 1.0 nM FcMeOH with 80 fM of NEs, respectively. We could observe the same trends of SEE results as the case with 8 pM NEs aforementioned. Hence, a linear decrease in C_{fill} from 15.7 M to 0.6 M is also seen, as FcMeOH concentration in aqueous solution sequentially decreases under each 0.8 pM and 80 fM NEs, respectively. A characteristic *i-t* curve and the corresponding size distribution curve of NEs under 1.0 nM FcMeOH with 80 fM of NEs is shown in SI (Figure S2.1).

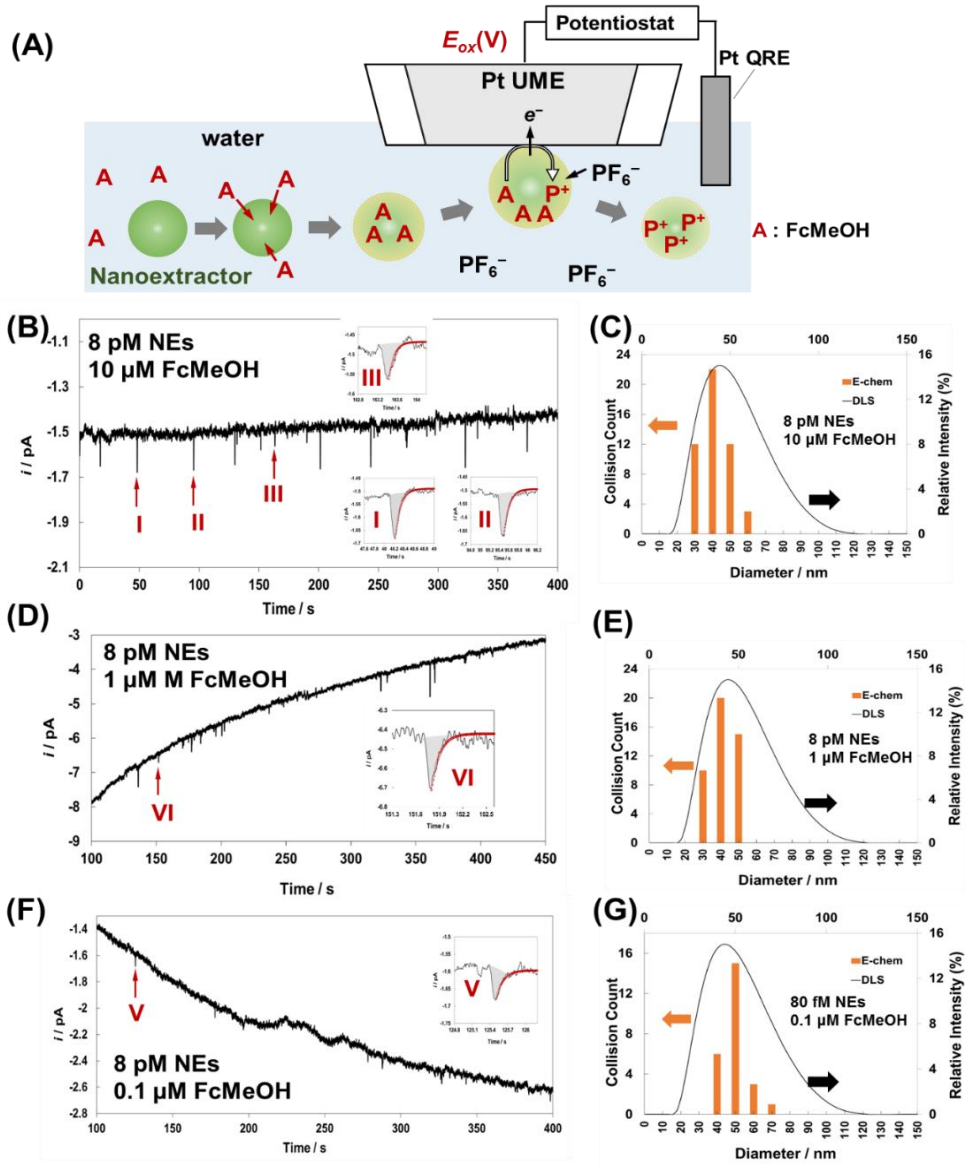

Figure 4.2 (A) A schematic illustration of SEE measurements using NEs as nanoextractor to effectively scavnage target compounds, A from water to NEs, and electrochemically sense them by oxidation (E_{tip} = 0.4 V vs Pt QRE) upon the collision of NE, (B) *i-t* curves in the presence of 10 μM FcMeOH with 8 pM NEs. The insets magnified typical current spikes fitted with bulk electrolysis model (red open circles), (D), (F) *i-t* curves in the presence of 1 μM FcMeOH with 8 pM NEs, and 0.1 μM FcMeOH with 8 pM NEs, respectively. The insets show magnified current spikes fitted with bulk electrolysis model (red open circles) as well. (C), (E) and (G) Size distribution curves of NEs based on the electrochemical measurements (orange bars) from (B), (D) and (F), and compared with DLS measurements (black solid lines), respectively.

Construction of Calibration Curves and the Analytical Validation with a Blind Sample.

We estimated a charge density at individual NEs using the integrated charges and the electrochemically determined diameter of NEs from three sets of SEE measurements, and finally constructed a plot of charge density vs. total concentration of FcMeOH (Figure 4.3A). In this plot, three curves for each NE concentration are depicted with showing sigmoidal trends. This plot is analytically useful, since it can be utilized as a calibration curve for the quantitative analysis of unknown samples. Once excluding the saturated region, each three curve was fitted with exponential function (Figure 4.3B). The respective exponential equations and R^2 correlation coefficients ($\geq$ 0.99) are given in Figure 3B. Note that three curves are almost identical, only laterally shifted, indicating that the amount of FcMeOH in individual NEs extracted from aqueous bulk solution can be modulated by varying the volume ratio between total NEs and the total solution. Every an order of magnitude decrease in the volume ratio lowers the limit of detection (LOD) with an order of magnitude as well. Hence, 0.2 ppb LOD could be achieved in 1 nM FcMeOH solution in the presence 80 fM NEs.

The analytical merit of this charge density plot is validated by testing a blind sample. A blind sample of FcMeOH solution was provided to the researchers without any information in advance. Three sets of SEE measurements were performed in the presence of 8 pM, 0.8 pM, and 80 fM NEs, separately (Figure 4.4). Each *i-t* curve shows characteristic current spikes, where a current decay is fitted with bulk electrolysis model implying the extraction/preconcentration of FcMeOH inside NEs. We repeated each set of SEE three times (data not shown). From each set of SEE data, average current densities were determined as 12.5 ($\pm$ 0.5) $\times 10^{-4}$, 2.5 ($\pm$ 0.2) $\times 10^{-4}$, and 3.0 ($\pm$ 0.2) $\times 10^{-4}$ fC/nm^3 for 80 fM, 0.8 pM, and 8 pM NEs respectively. Using a goal-seek function in Excel and the exponential equations obtained from each NE concentration, the corresponding concentrations of FcMeOH in the blind sample were estimated as 22 ($\pm$ 2) nM, 34 ($\pm$ 3) nM, and 430 ($\pm$ 50) nM FcMeOH for 80 fM, 0.8 pM, and 8 pM NEs, respectively.

In the charge density plot (Figure 3B), we defined an accuracy range as 30 – 95 % of maximum charge density (15.5 × 10^{-4} fC/nm^3), where the slope of a curve is steep enough to sensitively correlate the total analyte concentration with the charge density in NEs. If the estimated charge density is outside the accuracy region, i.e., less than 30 % or higher than 95 %, it would give only upper limit or lower limit of analyte concentration, respectively. Based on this definition of accuracy range, we could accept the estimated FcMeOH concentration, 22 (± 2) nM determined by the curve with 80 fM NEs, which is close to the true value of the blind sample concentration, 20 nM. So, unknown sample concentration was accurately determined within 10 % of error range. This successful blind sample test validates our quantitative analysis using SEE combined with NEs as a nanoextractor via separation, preconcentration, and detection in situ.

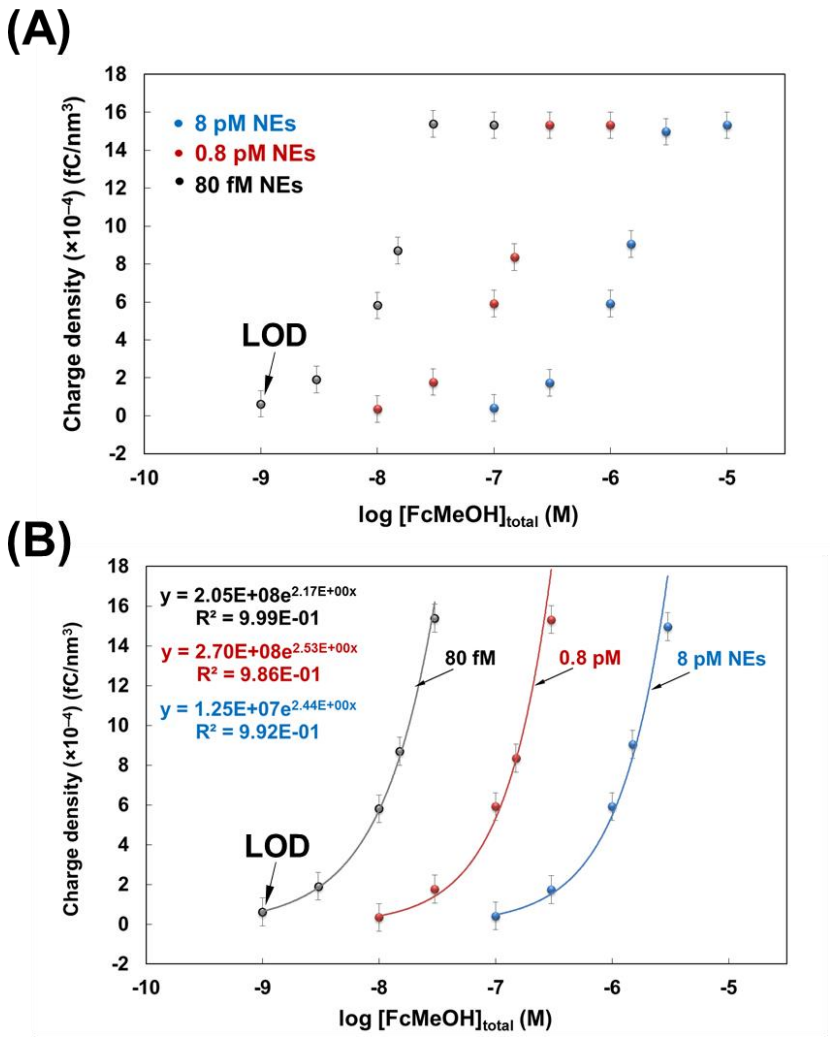

Figure 4.3 (A) Charge density curves vs. logarithm of total FcMeOH concentration in the presence of 8 pM (blue circles), 0.8 pM (red circles), and 80 fM NEs (grey circles), respectively. The charge density varies from 1.0×10^{-4} to 15.5×10^{-4} fC/nm^3 within ~2 orders of magnitude of FcMeOH concentration, showing a sigmoidal trend. The LODs under each 8 pM, 0.8 pM, and 80 fM NEs are 100 nM, 10 nM, and 1 nM (i.e. 20, 2, and 0.2 ppb) FcMeOH, respectively. (B) Calibration curves for corresponding three concentrations of NEs. Calibration curves are plotted within the dynamic range in (A), where calibration equations are obtained by fitting with exponential functions.

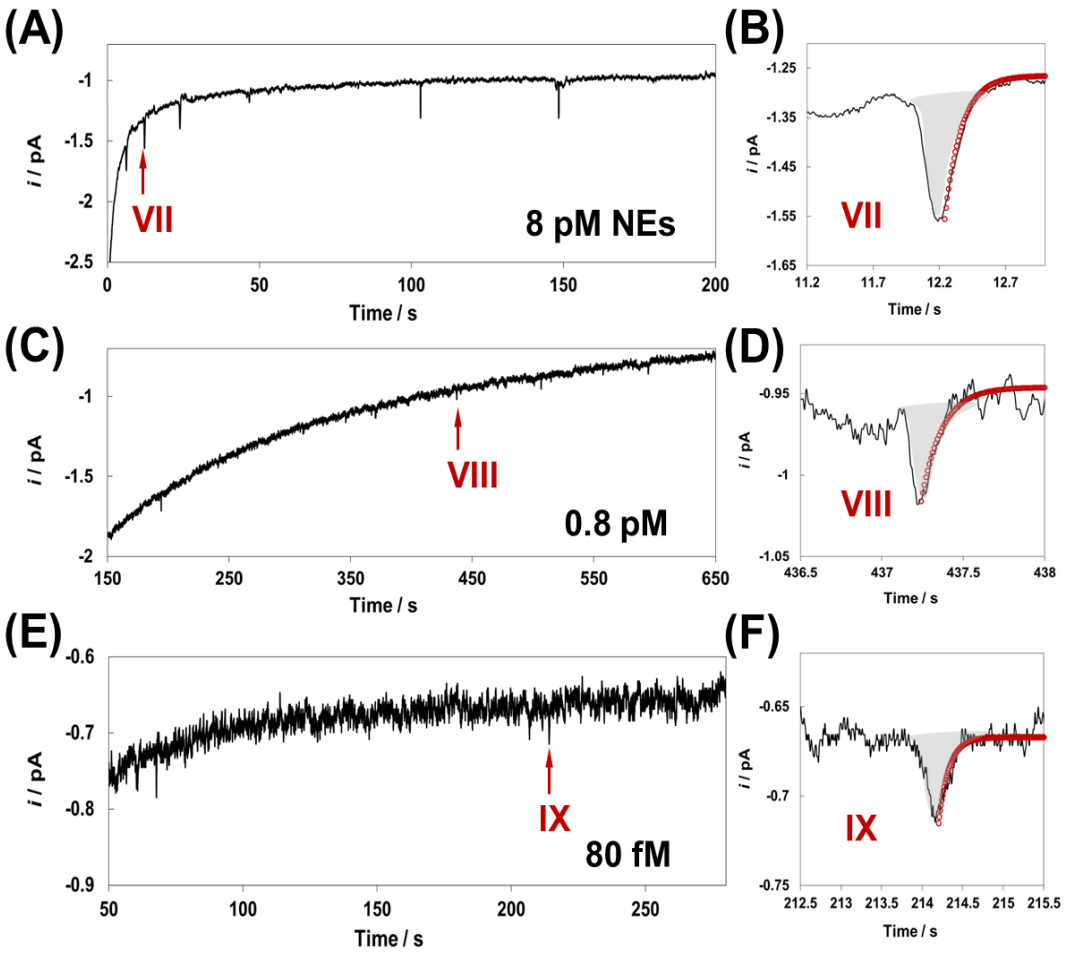

Figure 4.4 (A), (C), (E) *I-t* curves with a blind sample containing FcMeOH in the presence of 8 pM, 0.8 pM and 80 fM NEs, respectively. (B), (D), (F) Magnified current spikes fitted with bulk electrolysis model (red open circles).

Ultratrace Level Detection of Ubiquitous Aromatic Toxicants in Water.

Our ultrasensitive analysis is readily applicable to other aromatic toxicants. As typical carcinogen, 2-Aminobiphenyl (2-ABP) was studied with SEE combined with NEs. As aforementioned, three sets of SEE measurements under a constant potential (E_{tip} = 0.85 V vs Pt QRE) were performed in the presence of 8 pM, 0.8 pM, and 80 fM NEs, separately (more details in SI). We could observe similar trends in SEE data to the case of FcMeOH. For example, a typical *i-t* curve is illustrated with 1 nM 2-ABP in the aqueous bulk solution in the presence of 80 fM NEs (Figure 4.5A). Current spikes were well fitted with the bulk electrolysis model, implying the extraction/preconcentration of 2-ABP inside each NE. Based on the integrated charges from this *i-t* curve, eq (3) (i.e. C_{fill} = 0.6 M) and eq (4), the corresponding size distribution curve of NEs was constructed as shown in Figure 4.5B. A narrow range within 40 nm − 70 nm with a peak at 60 nm diameter was obtained, which is fairly consistent with DLS measurement. Since the current spikes under this condition are close to the limit of detection in our measurements, charges integrated from *i-t* curve could be slightly overestimated, thus leading to the larger mean diameter of NEs, 60 nm than DLS or TEM data.

Finally, using the integrated charges and the electrochemically estimated size of NEs from all sets of SEE data, the charge density plot vs. total concentration of 2-ABP could be constructed (Figure 4.5C, a numerical fitting with exponential function is depicted in SI). The resultant plot shows not only the LOD up to 1 nM, i.e. 0.17 ppb of 2-ABP, but also nearly identical trends to those for FcMeOH. Notably, this trend indicates that the extraction/preconcentration behavior of NEs as a nanoextractor can be universal for ubiquitous aromatic compounds, which are common as environmental pollutants. Given

the excellent detection performance as well as the broad applicability for ubiquitous aromatic toxicants, the combination of NEs with SEE offers great prospects as a sensor for environmental applications. Further, this remarkable sensitivity will be synergized by

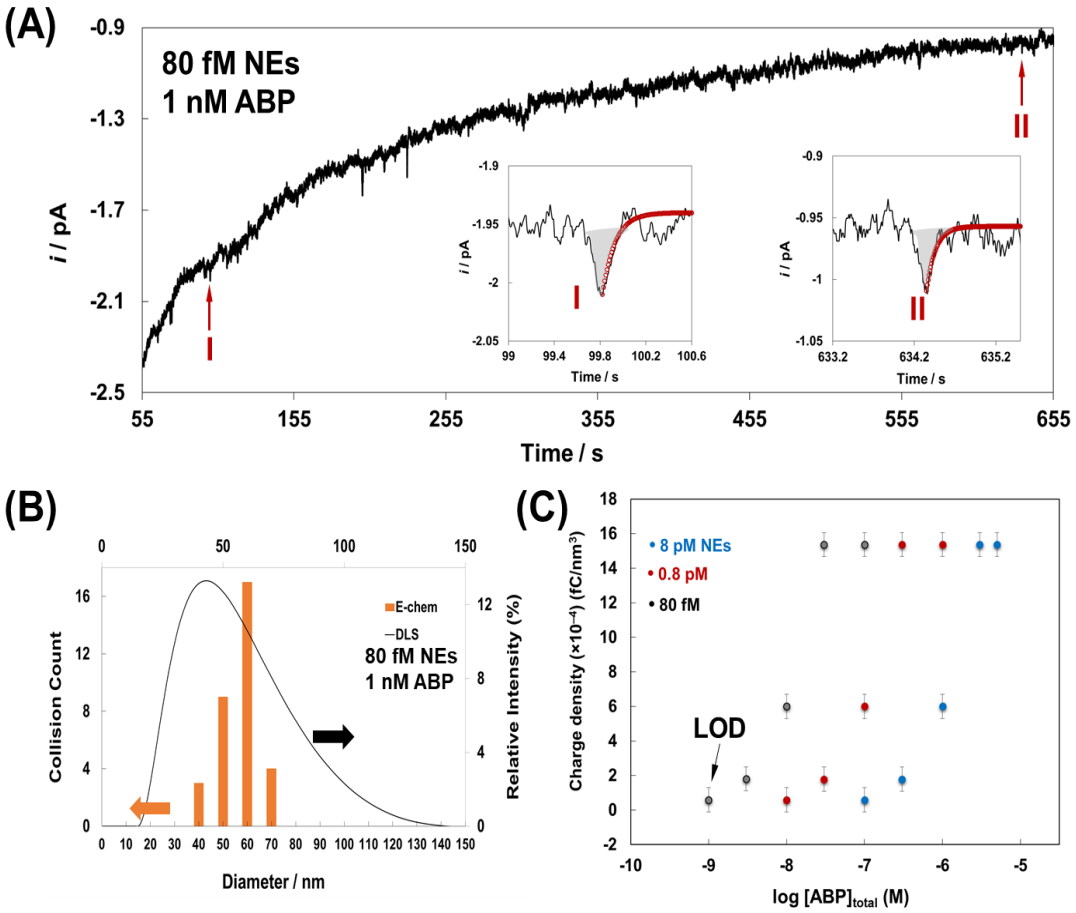

Figure 4.5 (A) *I-t* curves in the presence of 1 nM 2-ABP with 80 fM NEs ((E_{tip} = 0.85 V vs Pt QRE). The insets magnified typical current spikes fitted with bulk electrolysis model (red open circles). (B) Size distribution curves of NEs based on the electrochemical measurements (orange bars) from (A) and DLS measurements (black solid lines). (C) Charge density curves vs. logarithm of 2-ABP concentration in aqueous bulk solution in the presence of 8 pM (blue circles), 0.8 pM (red circles), and 80 fM NEs (grey circles), respectively.

incorporating selectivity factors such as a chelator inside NEs.

CONCLUSIONS

In conclusions, we could successfully employ NEs as nanoextractors, and explored the ultra-trace level sensing of aromatic toxicants from water using the stochastic electrochemistry, SEE. The direct and in-situ measurements of analytes extracted from water into NEs were enabled via electrochemical oxidation upon the collision of each individual NE to Pt UME. This new analytical approach exhibited a detection limit of ~0.1 ppb level for aromatic compounds dissolved in water owing to the unprecedentedly high partition coefficient of intact NEs. The extraction efficiency of NEs was remarkable to reach the preconcentration factor up to ~8 orders of magnitude, which is considered superior to previously reported analytical sensing. Given its excellent detection performance as well as the broad applicability for ubiquitous aromatic contaminants, the combination of NEs with SEE offers great prospects as a sensor for environmental applications.

Author Information

Corresponding Author

*Phone: +1 (401) 874-2143. E-mail: jkim25@uri.edu.

ORCID

Jiyeon Kim: 0000-0002-7624-6766

Author Contributions

All authors have given approval to the final version of the manuscript

Notes

The authors declare no competing financial interest.

Supporting Information

Characterization of NEs by Dynamic Light Scattering, Fitting *i-t* Decay with Bulk Electrolysis Model, Electrochemistry of 2-ABP in THF Cocktail Solution, Calibration curves for 2-ABP with 8 pM, 0.8 pM, 80 fM NEs

Acknowledgements

This work was supported by the Research Bridge Funding Initiative, Start up fund from University of Rhode Island, and Medical Research Fund (20174373) from Rhode Island Foundation. We acknowledge Irene Andreu for TEM characterization conducted at the RI Consortium for Nanoscience and Nanotechnology, supported by the National Science Foundation EPSCoR Cooperative Agreement #OIA-1655221 and the College of Engineering at URI.

REFERENCES

1. https://www.un.org/waterforlifedecade/quality.shtml

2. Mojiri, A.; Zhou, J. L.; Ohashi, A.; Ozaki, N.; Kindaichi, T., "Comprehensive review of polycyclic aromatic hydrocarbons in water sources, their effects and treatments", *Sci. Total Environ.*, **2019**, 696, 133971.

3. Manzetti, S., "Polycyclic aromatic hydrocarbons in the environment: Environmental fate and transformation", *Polycycl. Aromat. Comp.*, **2013**, 33, 311–330.

4. DiScenzaa, D. J.; Lyncha, J.; Verderamea, M.; Seriob, N.; Prignanoc, L.; Gareaud, L.; Levine, M., "Efficient Fluorescence Detection of Aromatic Toxicants and Toxicant Metabolites in Human Breast Milk", *Supramol Chem.*, **2017**, 30, 267–277.

5. Pongpiachan, S.; Hattayanone, M.; Pinyakong, O.; Viyakarn, V.; Chavanich, S. A.; Bo, C.; Khumsup, C.; Kittikoon, I.; Hirunyatrakul, P., "Quantitative ecological risk assessment of inhabitants exposed to polycyclic aromatic hydrocarbons in terrestrial soils of King George Island, Antarctica", *Polar Science*, **2017**, 11, 19-29.

6. https://www.atsdr.cdc.gov/csem/csem.asp?csem=13&po=8

7. Khalili, N.R.; Scheff, P.A.; Holsen, T.M., "PAH source fingerprints for coke ovens, diesel and gasoline engines, highway tunnels, and wood combustion emissions." *Atmosphere. Environ.* **1995**, 29, 533–542.

8. Nieva-Cano, M.J.; Rubio-Barroso, S.; Santos-Delgado, M.J., "Determination of PAH in food samples by HPLC with fluorimetric detection following sonication extraction without sample clean-up." *Analyst*, **2001**, 126, 1326–1331.

9. Aiken, A.C.; DeCarlo, P.F.; Jimenez, J.L., "Elemental analysis of organic species with electron ionization high-resolution mass spectrometry." *Anal. Chem.*, **2007**, 79, 8350–8358.

10. Delgado, B.; Pino, V.; Ayala, J.H.; González, V.; Afonso, A.M., "Nonionic surfactant mixtures: a new cloud-point extraction approach for the determination of PAHs in seawater using HPLC with fluorimetric detection." *Anal. Chim. Acta*, **2004**, 518, 165–172.

11. Frysinger, G.S.; Gaines, R.B.; Xu, L.; Reddy, C.M., "Resolving the unresolved complex mixture in petroleum-contaminated sediments." *Environ. Sci. Technol.*, **2003**, 37, 1653–1662.

12. Lovelnm, C.; Attama, A. A., "Current state of Nanoemulsions in Drug Delivery", *J. Biomater. Nanobiotechnol.*, **2011**, 2, 626-639.

13. Sabaragamuwe, S. G.; Conti, D.; Puri, S. R.; Andreu, I.; Kim, J, "Single-Entity Electrochemistry of Nanoemulsions: The Nanostructrual Effect on Its Electrochemical Behavior", *Anal. Chem.*, **2019**, 91, 9599-9607.

14. Madawala, H.; Sabaragamuwe, S. G.; Kim, J., "In Situ Measuring Partition Coefficient of Nanoemulsions: A New Application of Single Entity Electrochemistry", *submitted,* **2020**.

15. Kaur, A.; Gupta, U., "A review on applications of nanoparticles for the preconcentration of Environmental pollutants", *J. Mater. Chem.*, **2009**, 19, 8279–8289

16. (a) Maier, M.; Fritz, H.; Gerster, M.; Schewitz, J.; Bayer, E., *Anal. Chem.*, **1998**, 70, 2197. (b)

Mangun, C. L.; Yue, Z. R.; Economy, J.; Maloney, S.; Kemme, P.; Croprk, D., *Chem. Mater.*, **2001**, 13, 2356. (c) Deng, S.; Bai, R., *Environ. Sci. Technol.*, **2003**, 37, 5799. (d) Bembnowska, A.; Pelech, R.; Milchert, E., *J. Colloid. Interface. Sci.*, **2003**, 265, 276. (e) Yue, Z.; Economy, J.;

Rajaopalan, K.; Bordson, G.; Piwoni, M.; Ding, L.; Snolyink, V. L.; Marinas, B. J., *J. Mater. Chem.*, **2006**, 16, 33. (f) Yuan, G., *J. Environ. Sci. Health A*, **2004**, 39, 2661. (g) Cheng, X.; Kan, A. T.; Tomson, M. B., *J. Chem. Eng. Data*, **2004**, 49, 675. (h) Hashizume, H., *J. Ion-Exchange*, **2003**, 14, 2615. (i) Liu, Y.; Majetich, S. F.; Tilton, R. D.; Lowry, G. U., *Environ. Sci. Technol.*, **2005**, 39, 1338. (j) Xu, Y.; Zhang, W., *Ind. Eng. Chem. Res.*, **2009**, 39, 2238. (k) Zhang, W., *J. Nanopart. Res*, **2003**, 5, 323. (k) Cao, J.; Elliot, D.; Zhang, W., *J. Nanopart. Res.*, **2005**, 7, 499. (l) Lien, H.; Zhang, W., *J. Environ. Eng.*, **1999**, 125, 1042. (m) Kumbhar, A.; Chumanov, G., *J. Nanopart. Res.*, **2005**, 7, 489. (n) Wu, L.; Shamuzzoha, M.; Ritchie, S. M. C., *Environ. Sci. Technol.*, **2005**, 7, 469. (o) Zhao, X.; Cai, Y.; Mou, S., *Environ. Sci. Technol.*, **2008**, 42, 120. (p) Paknikar, K. M.; Nagpal, V.; Pethkar, A. V.; Rajwade, J. M., *Sci. Technol. Adv. Mat.*, **2005**, 6, 370. (q) Zhou, Q.; Ding, Y.; Xiao, J.; Liu, G.; Guo, X., *J. Chromatogr. A*, **2007**,

1147, 10. (r) Katsumata, H.; Matsumoto, T.; Kaneco, S.; Suzukki, T.; Ihta, K., *Microchem. J.*, **2008**, 88, 82. (s) Zhou, Q.; Xiao, J.; Wang, W., *J. Chromatogr. A.*, **2006**, 1125, 152. (t) Cui, Y. Q.; Jiang, G. B.; Liu, J. F.; Zhou, Q. X., *Anal. Chem.*, **2003**, 75, 2517. (u) Niu, H.; Cai, Y.; Shi, Y.; Wei, F.; Liu, J., *Anal. Chim. Acta*, **2007**, 594, 81. (v) Yang, K.; Xing, B., *Environ. Pollut.*, **2007**, 145, 529. (w) Cai, Y. Q.; Jiang, G. B.; Liu, J. F.; Zhou, Q. X., *Anal. Chim. Acta*, **2003**, 494, 149. (x) Zhou, Q.; Wang, J.; Liu, W.; Shi, G.; Shi, Q.; Wang, J., *Talanta*, **2006**, 68, 1309. (y) Zhou, Q.; Xiao, J.; Wang, W., *Anal. Sci.*, **2007**, 23, 189. (z) Ramesh, A., www.cipac.org, applications of certain nanoparticles in preconcentration of herbicide residue in water, **2007**.

17. Miller, E. C.; Sandin, R. B.; Miller, J. A.; RUSCH, A. P., "The Carcinogenicity of Compounds Related to 2-Acetylaminofluorene, III. Aminobiphenyl and Benzidine Derivatives", *Cancer Res.*, **1956**, 16, 525-534.

18. Kim, B-K.; Boika, A.; Kim, J.; Dick, J. E.; Bard. A. J.," Characterizing Emulsions by Observation of Single Droplet Collisions: Attoliter Electrochemical Reactors", *J. Am. Chem. Soc.*, **2014**, 136, 4849-4852.

19. Bard, A. J.; Faulkner, L. R., "Electrochemical Methods: Fundamental and Applications", **2004**, 2nd Ed., John Wiley & Sons INC.

APPENDIX 1: CHAPTER 2 SUPPORTING INFORMATION

SINGLE-ENTITY ELECTROCHEMISTRY OF NANOEMULSIONS: THE NANOSTRUCTURAL EFECT ON ITS ELETROCHEMICAL BEHAVIOUR

Shashika Gunathilaka Sabaragamuwe[1], Dylan Conti[1], Surendra Raj Puri[1], Irene Andreu[2], Jiyeon Kim[1]*

[1.] Department of Chemistry, University of Rhode Island, Kingston, RI, 02881

[2.] RI Consortium of Nanoscience and Nanotechnology, Department of Chemical Engineering, University of Rhode Island, Kingston, RI, 02881

1. Experimental Section

Fabrication of Pt UME and Nanopipet Electrodes.

5μm dia. Pt UME was fabricated by using a CO_2-laser puller, microforge,[S1] and then, a homemade polisher. Briefly, 25 μm dia. Pt wire (Goodfellow, annealed) inserted in the borosilicate capillary (I.D. 0.2 mm, O.D. 1mm, item No 9-000-2000, Drummond scientific company, Broomall, PA) was pulled together with CO_2 laser puller (P-2000, Sutter). Continuously, Pt UME was further annealed by microforge (MF-0P, Narishige, Japan) for a smaller RG (a ratio between glass sheath and Pt radii) as well as a better sealing. The annealed Pt UME was milled by a homemade polisher (adhesive diamond lapping film is attached on the 3.5" hard disk drive equipped with an external enclosure and external power, adhesive diamond lapping film 0.1μm, 50-30155,

Alliedhightech.com) to expose Pt disk resulting in an inlaid disk shaped electrode. To avoid any damage of electrode caused by a potentiostat, "cell on between run" function was activated during electrochemistry with a bipotentiostat (CHI 760E, CH Instrument, Austin, TX). Prepared Pt UME was also used under 30 % or higher relative humidity at 22~23 °C.

Tapered nanopipets with an inner tip radius of ~60 nm were obtained by puling 10 cm long quartz capillaries (outer/inner diameter ratio of 1.0/0.7; Sutter Instrument Co., Novato, CA) using a CO_2-laser capillary puller (model P-2000, Sutter Instrument).[S2] In details, A quartz capillary was cleaned by compressed-air blowing and pulled in CO_2 laser puller with pulling parameters (heat= 710, filament= 4, velocity= 30, delay= 130 and pull= 130). The pipets were then cleaned with UV plasma cleaner for 3 min under pursing with Ar gas before the silanization. The pulled nanopipets were dried for 1.5 hours under vacuum (~70 m Torr) in a desiccator (Mini-vacuum desiccator, Bel-Art Products, Pequannock, NJ) and then silanized by introducing 50 μL of N, N-dimethyltrimethylsilylamine into round bottom flask connected to the desiccator. Silanization was performed for 40 min under a constant relative humidity 16% at 20 °C controlled in a N_2 purged glove bag. After silanization, the desiccator was vacuumed for 10 min followed by purging with N_2 for 5 min to remove extra silanization reagent. The silanized pipets were further filled with 10 uL of a DOS solution containing 40 mM of the organic supporting electrolytes ($K^+ \cdot TFAB^-$) right before electrochemical measurements.

Nanopipet Voltammetry.

Nanopipet voltammetry was carried out in a two-electrode cell at ambient temperature (20 °C). A nanopipet electrode was prepared by using a silanized pipet andfilling it with the organic phase containing DOS and 40 mM KTFPB. An electrochemically etched Ni/Cu wire was inserted inside the nanopipet to control the interfacial potential. This pipet was further immersed in the aqueous solution containing 10 mM NH_4PH_6 or NH_4Cl as a supporting electrolyte. Using a bipotentiostat (CHI760E, CH Instrument, Austin, TX), cyclic voltammetry was performed by scanning the potential through a Ni/Cu wire inside the nanopipet against Pt QRE in water. Finally, the radius and quality of this pipet were characterized by studying the TBA^+ ion transfer. All voltammograms were recorded at 25 mV/s scan rate.

Cell 1 (buffer only in aqueous phase):

Ni/Cu | 40 mM KTFPB + DOS || water | Pt

Cell 2 (buffer + anions in aqueous phase):

Ni/Cu | 40 mM KTFPB + DOS || 10 mM NH_4PF_6 or NH_4Cl | Pt

Cell 3 (buffer + anions + TBA^+ in aqueous phase):

Ni/Cu | 40 mM KTFPB + DOS || 0.9 mM TBA^+ 10 mM NH_4PF_6 or NH_4Cl | Pt

Cell 4 (buffer + TBA+ in aqueous phase for K+ egress study):

Ni/Cu | 40 mM KTFPB + DOS || 0.9 mM TBA^+ | Pt

or, Ni/Cu | 40 mM TDDA+·$TFAB^-$ + DOS || 0.9 mM TBA^+ | Pt

2. Mechanistic Aspects in Forming Monodispersed Nanoemulsions with ~40 nm Diameter. To reproducibly form NEs with average sizes of ~40 nm as well as small PDI value, a combination of high-speed homogenization method with spontaneous

emulsification method was utilized. The schematic view of synthesis procedure is illustrated in Figure S2.1.

First, a THF cocktail containing KTFPB as ion exchangers, castor oil (*i.e.* DOS) as plasticizer, and F-127 as surfactants was prepared as a continuous oil phase. Vortex at 3000 rpm for 1 hr was carried out to thoroughly dissolve all the components in THF for a homogenous solution. 0.1 mL aliquot of the homogenous THF solution was quickly and forcefully injected into 4 mL nanopure water using a syringe under vortex at a spinning speed of 4000 rpm, and the overall solution was kept vortexing for 2 min (Figure S2.1A). During this process, the oil phase is immediately precipitated in the aqueous phase and forms droplets with wide size distribution.

Higher vortex rate affords high collision frequency between the oil and aqueous phases, thus causing efficient precipitation with smaller droplet sizes. Continuously, another batch of 4 mL was prepared. Right after 2 min vortex for each batch, two batches were combined and the overall solution (*i.e.* 8 mL) was subsequently homogenized under 4900 rpm for 2 min (Figure S2.1B). High-speed homogenization mainly provides the shearing force required to break up the oil and water phase, thereby forming the nanometer-sized emulsions.[S3] And yet, emulsions produced by this rotor device always have large particle sizes and wide particle size distribution as well.

To control the mono-dispersity as well as the stability of NEs, spontaneous emulsification method was further combined. Here, we blew N_2 gas over the meniscus of NE solution for 1 hr to evaporate THF at a rate of 2 mL/hr, and accelerate the spontaneous emulsification (Figure S2.1C). In this spontaneous emulsification step, water-miscible THF with containing castor oil, surfactants, and borate compounds moves from the

organic phase into the aqueous phase. Due to this movement, a large turbulent force at the oil-water interface is generated, and subsequently the oil-water interfacial area is increased, thus causing the spontaneous formation of nanometer-sized emulsions surrounded by the aqueous phase.[S4] At the same time, the evaporation of THF induces spontaneous nucleation of oil droplet composed of castor oil, surfactants, and borate compounds, thereby forming the final state of NEs dispersed in the aqueous phase (Figure S2.1D).[S5] This final step is critical to obtain NEs of ~40 nm diameter with small PDI value. Due to a small size of NEs below 50 nm diameter, the prepared solution of NEs is transparent without blur or opaqueness. At any steps, the formation of froth should be avoided for reproducible outcomes. Based on the assumption that all added castor oil in the aqueous phase forms NEs with 40 nm diameter (determined by DLS), the concentration of NE stock solution could be estimated to ~390 pM.

It should be noted that all the hydrophobic components dissolved in 0.2 mL of the original THF cocktail are finally concentrated in the castor oil (DOS, 76.9 nL) via solvent evaporation step, thus ~2600 fold of the preconcentration factor can be achieved. For example, 6 mM ferrocene (Fc) in the initial THF cocktail solution can be concentrated 2600-fold in NE, thus the Fc concentration, *CFc* is expected to be 15.8 M in 50 zL volume of each NE droplet. In fact, this concentration is unprecedentedly high even compared to FuelSpec® 118 series containing ~6 M of Fe, colloidal dispersions developed by SFA for the combustion catalysts.[S6] We validate this hypothesis about the high Fc concentration in NEs using SEE via the direct oxidation of Fc in individual NEs.

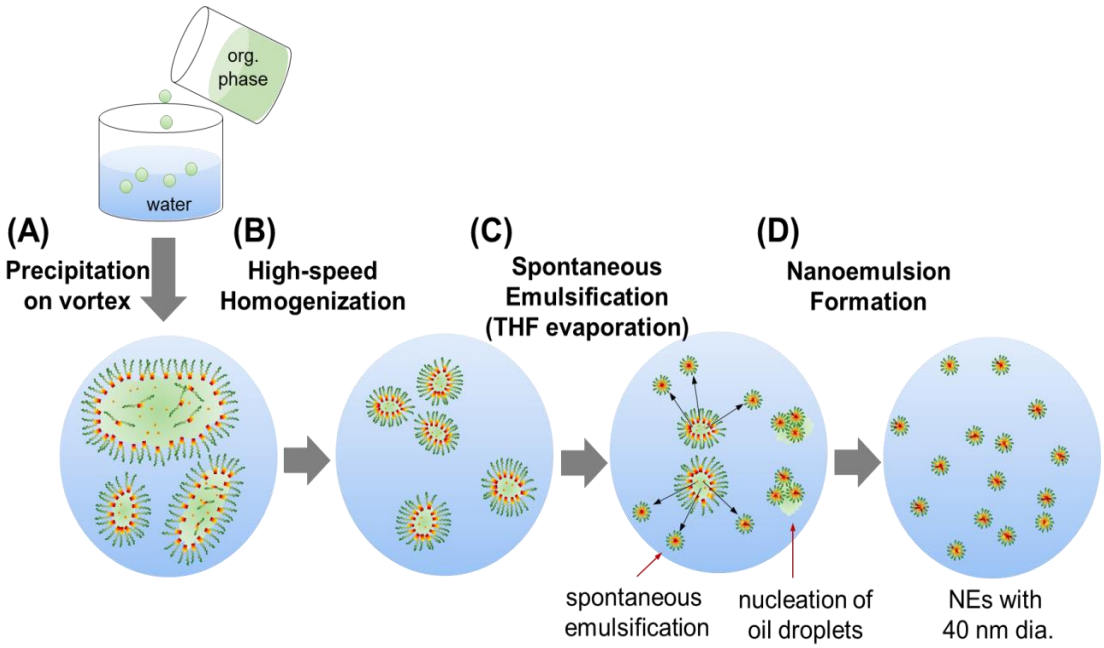

Supplementary Figure 2.1. Schematic representation of proposed mechanism for monodispersed NE formation. (A) Precipitation of oil droplets in aqueous phase during vortex, (B) High-speed homogenization for breaking up the oil/water phase to form nanometer sized emulsions, (C) THF evaporation for both spontaneous emulsification and spontaneous nucleation of oil droplets, (D) Final states of monodispersed NEs (not in scale).

3. TEM Images obtained with 8 pM NE suspension.

To confirm the intactness of NEs at a highly diluted concentration, we visualized the NEs by TEM images prepared with 8 pM NE250 suspension, the same concentration as studied for the SEE. We could observe that the highly monodispersed NE250 in Figure S2.2A and S2.2B. The smaller than 50 nm in diameter observed in TEM images are burning artifacts from the negative staining solution (see Figure S2.2C and S2.2D) and were not considered for evaluations of size and size distribution of the NEs.

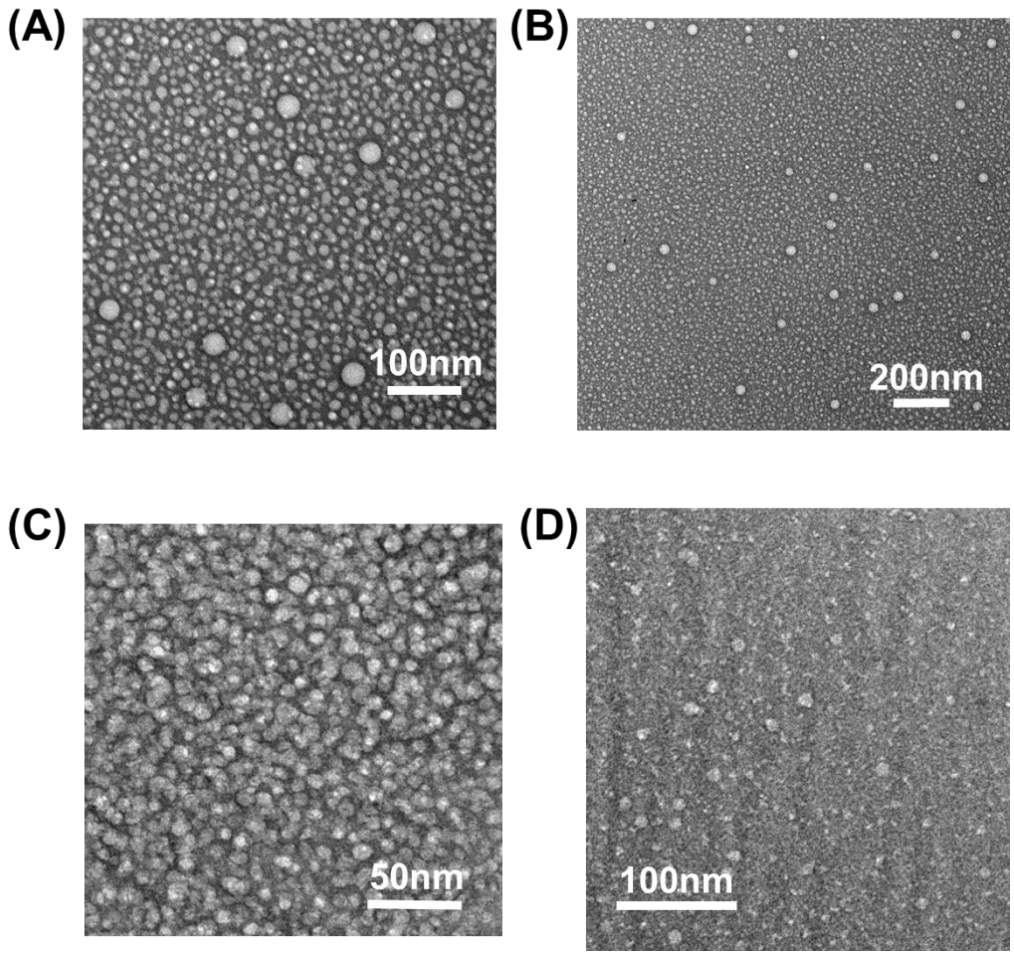

Supplementary Figure 2.2**.** TEM images obtained at 100 kV of (A), (B) NE250 with 8 pM NE250 suspension, (C), (D) TEM grid treated only by Uranyless negative staining solution without NE250 suspension.

4. Characterization of Nanopipets and Pt UMEs

Nanopipet used for the nanopipet voltammetry were characterized by SEM and cyclic voltammetry with TBA^+ transfer. In Figure S2.3A, the as pulled nanopiet was observed by SEM after Au sputtering, which shows 121 nm inner diameter with ~170 nm outer diameter. Further, the pipets were electrochemically characterized after each nanopipet voltammetry measurements by adding TBA^+ in the aqueous solution. The limiting current at the nanopipet is given by, [S7]

$$i_{lim} = 4xz_iFD_iC_ia \qquad \text{eq S1}$$

where F is the Faraday constant (96485 C/mol), and z_i, D_i, and C_i are the charge of the transferred drug ion i, its diffusion coefficient, and bulk concentration in the aqueous boric acid buffer solution, respectively, and x is a function of outer radius (r_g) / inner radius (a) of a nanopipet. Silanized pipet with r_g/a = 1.4 determined by SEM measurements has x = 1.18.

a was determined as 63 nm from the limiting current of a TBA+ transfer using eq s1 with z TBA^+ = 1, C_{TBA+} = 0.9 mM, and D_{TBA+} = 6.0 × 10−6 cm_2/s.[S8] The inner radii from this electrochemical characterization and SEM measurements are nearly identical indicating an inlaid-disk shaped geometry of ITIES owing to a well-controlled silanization of a nanopipet (Figure S2.3A,B). The prepare Pt UME was electrochemically characterized by performing voltammetry in 1 mM FcMeOH, 0.1 M KNO_3 solution (Figure S2.3C). According to eq S1 with n (transferred electron number, n = 1 for Fc) instead of z_i, the radius of Pt UME is estimated as 2.5 μm.

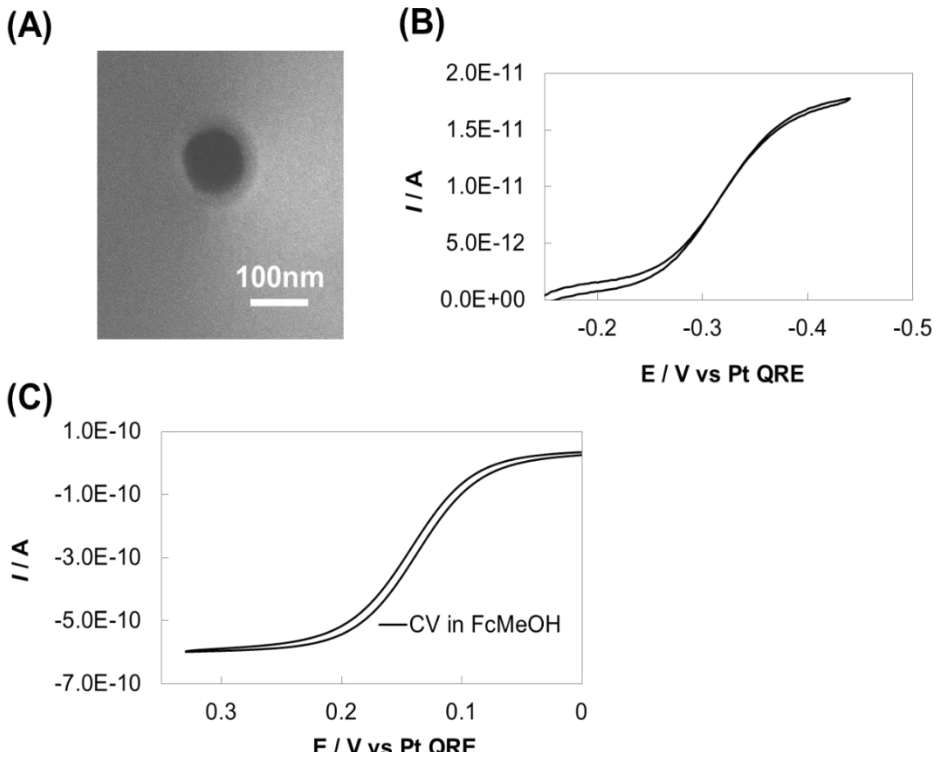

Supplementary Figure 2.3. (A) SEM image of an orifice of a nanopipet with 3 nm thick Au layer coated by Au sputter coater. SEM image was obtained using an accelerating voltage 5 kV to minimize charging-up. (B) Voltammogram of TBA^+ transfer with 0.9 mM TBA^+ dissolved in the aqueous solution. (C) Voltammogram of FcMeOH oxidation using 2.5 µm radius Pt UME in 1 mM FcMeOH, 0.1 M KNO_3 solution. Scan rate was 25 mV/s.

5. Pictures of Synthesized NEs.

In Figure S2.4, we show all the pictures during the NE synthesis: (A) an initial THF cocktail containing 6 mM Fc, (B) vortexing of THF cocktail for complete dissolution, (C) forceful injection of THF cocktail into water during vortex (precipitation step), (D) continuous homogenization after precipitation step, (E) THF evaporation with N_2 gas, (F) a transparent NE stock solution, (G) an initial THF cocktail containing 7 mM Fc, and (H) a resulting final NE stock solution with yellowish Fc precipitations on the bottom.

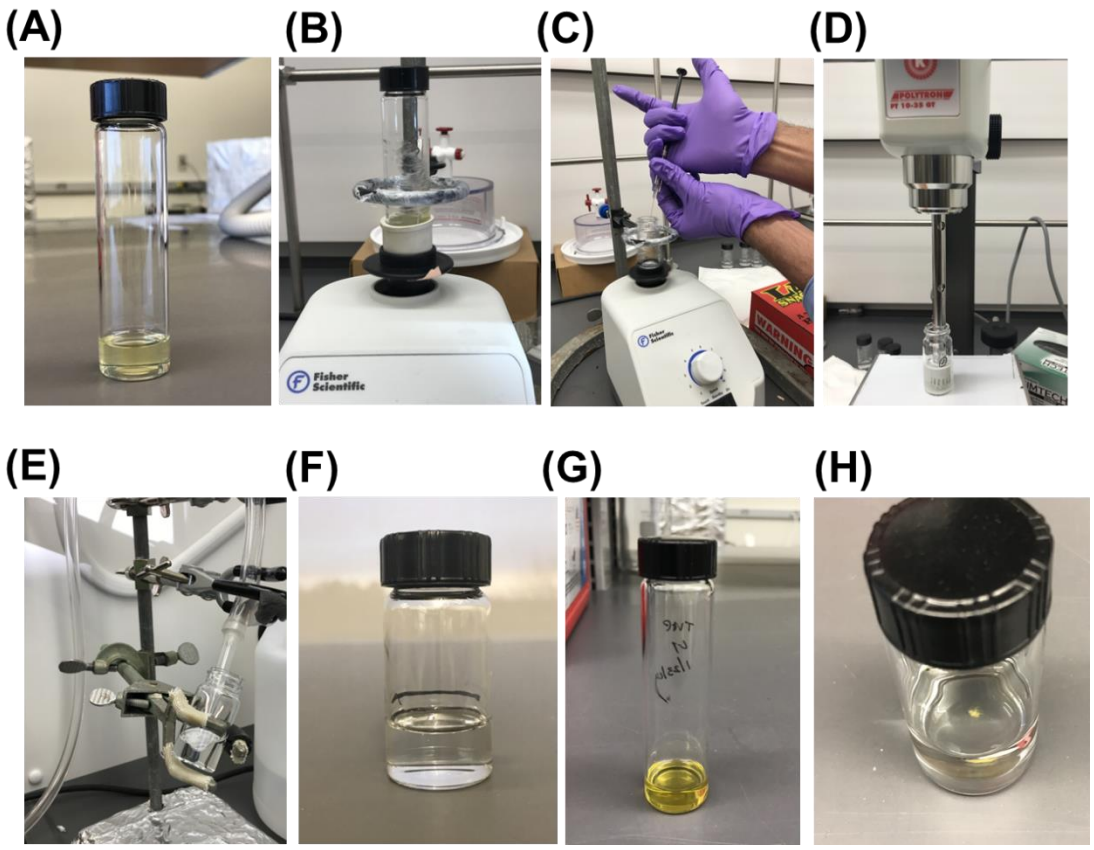

Supplementary Figure 2.4**.** (A) a THF cocktail containing 6 mM Fc, (B) dissolution of THF cocktail with vortex, (C) precipitation of organic phase during vortex, (D) continuous homogenization, (E) THF evaporation with blowing N_2 gas, (F) a final NE stock solution, (G) a THF cocktail containing 7 mM Fc, (H) a final NE stock solution with yellowish Fc precipitations.

6. Cyclic Voltammetry for Fc oxidation in THF Cocktail Solution.

To determine the diffusion limiting potential for Fc oxidation in NE for stochastic electrochemistry, we performed the voltammetry with THF cocktail solution containing Fc (Figure S2.5A). Due to a low dielectric constant, 7.58 of THF, a large uncompensated resistance has been observed even with borate compounds as supporting electrolytes. Under this condition, we could see a diffusion limiting current at ~0.80 V vs Pt QRE. Since castor oil used for a body of NEs has even lower dielectric constant, ε of 4.7, the presence of borate compounds in NE is necessary as a supporting electrolyte to reduce

the uncompensated resistance and drive electrochemical reaction.The Pt UME tested here was also electrochemically characterized by voltammetry in 1 mM FcMeOH, 0.1 M KNO_3 solution (Figure S2.5B). According to eq S1, the radius of Pt UME is estimated as 6.5 μm.

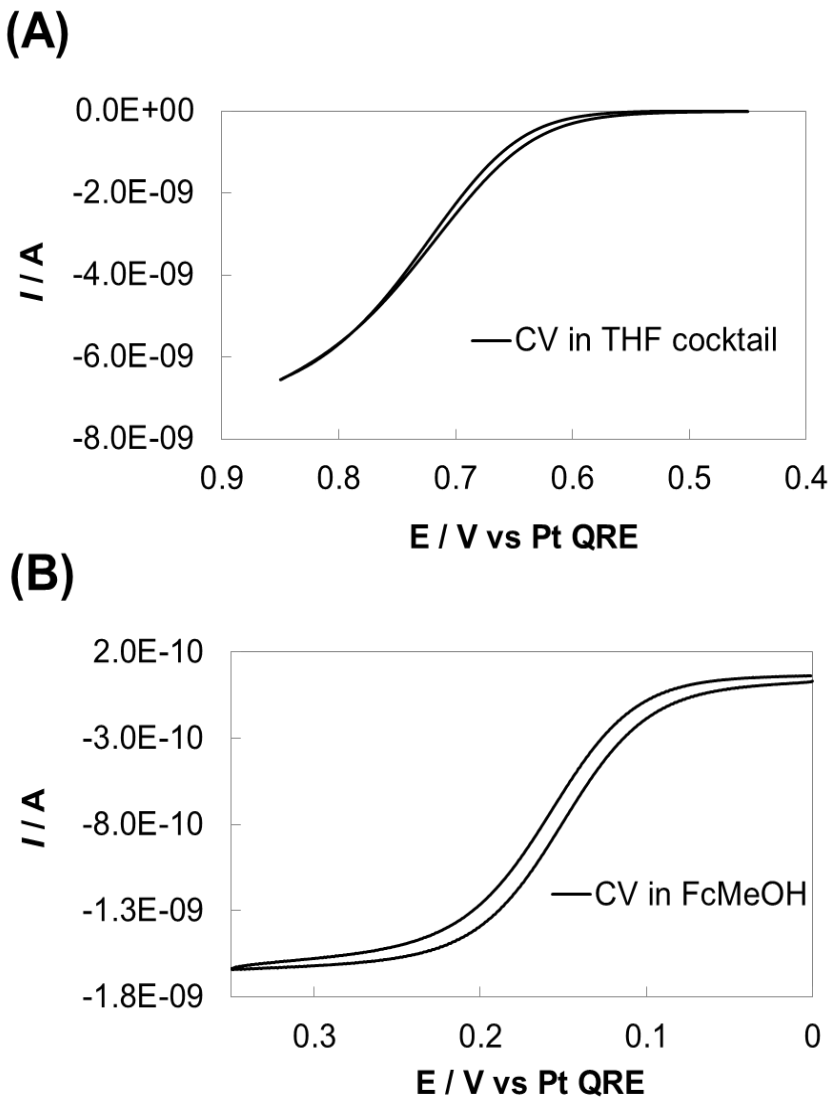

Supplementary Figure 2.5**.** (A) Voltammogram of Fc oxidation in the THF cocktail containing 6 mM Fc. (B) Voltammogram of FcMeOH oxidation using 6.5 μm radius Pt UME in 1 mM FcMeOH, 0.1 M KNO_3 solution. Scan rate was 25 mV/s.

7. More Electrochemical Measurements in Single-Entity Electrochemistry.

More data with NE250 and NE85 for the SEE measurements are shown in Figure S2.6. SEE was monitored at 0.85 v vs Pt QRE with 8 pM NE250 in Figure S2.5A. In Figure S5B, SEE measurement was obtaied with 8 pM NE85 at 1.0 V vs Pt QRE.

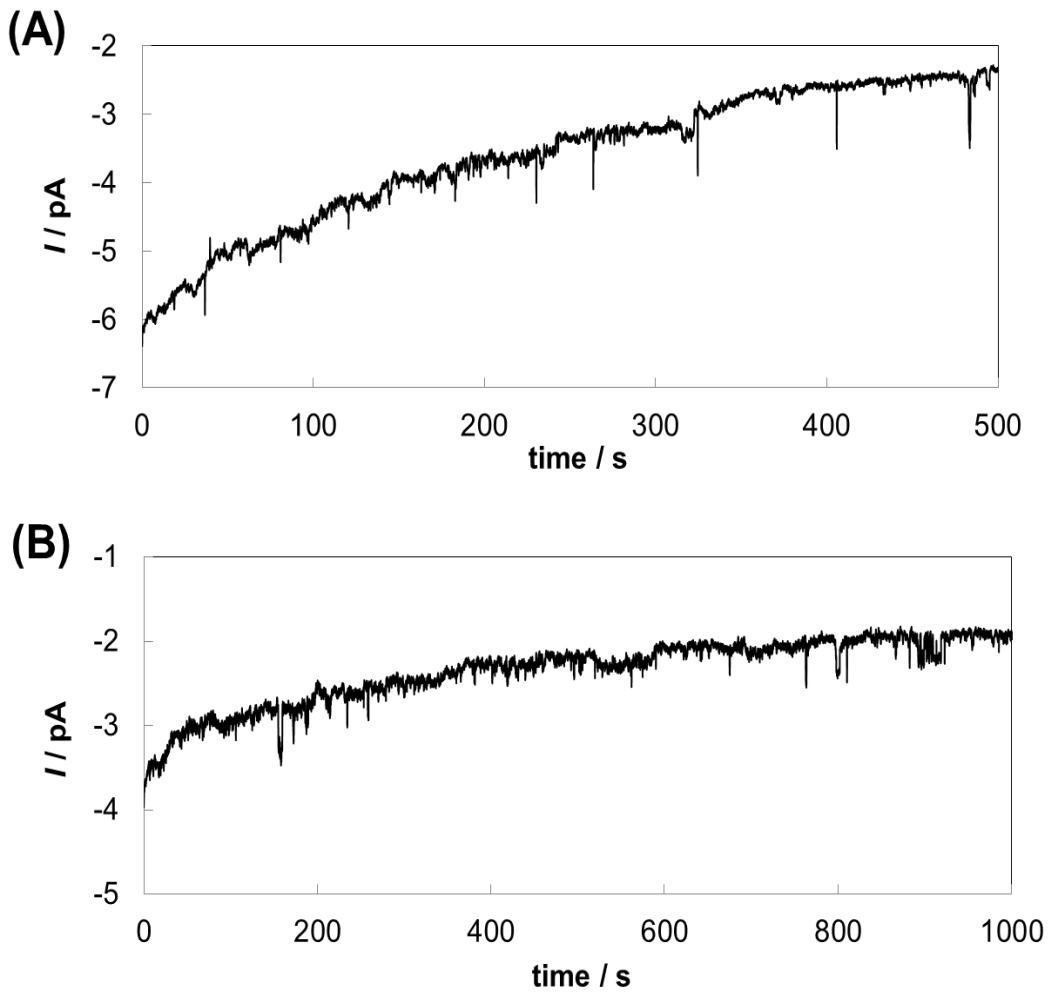

Supplementary Figure 2.6**.** (A) *i-t* curves of NE250 collisions at Pt UME under 0.85 V vs Pt QRE. 8 pM NE250 was added at zero time. (B) *i-t* curves of NE85 collisions at Pt UME under 1.0 V vs Pt QRE. 8 pM NE85 was added at zero time.

8. Fitting *i-t* Decay with Bulk Electrolysis Model

The collisional responses. *i-t* decay was fitted with bulk electrolysis model as below,[S9,S10]

$$i(t) = i_p e^{-\frac{mA}{V}t} \qquad \text{eq S3}$$

$$m = \frac{4D_{Fc}}{\pi r_c} \qquad \text{eq S4}$$

where, i_p (= 0.9 pA) is the initial peak current, t is the time (s), m is the mass-transfer coefficient, rc (=5.5 pm) and A (=9.49×10−19 cm^2) are a contact radius and area between an UME and a NE, respectively, V (= 2.65×10^{-23} cm^3 for 18.5 nm radius NE) is a NE volume, and D_{Fc} (= 1×10^{-7} cm2/s) is the diffusion coefficient of Fc in the castor oil inside a NE. In Figure S2.7, we show a good agreement between the experimental *i-t* curve (black solid lines) and the simulation (red open circles), thus validating bulk electrolysis within a ~38 nm diameter NE.

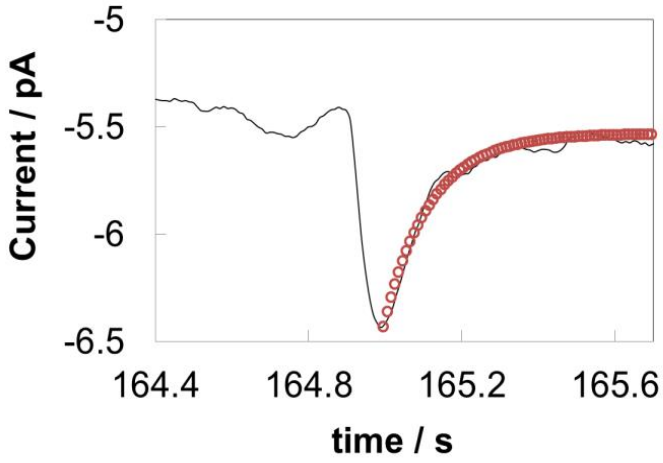

Supplementary Figure 2.7**.** *i-t* curve of a NE250 collision at Pt UME under 0.85 V vs Pt QRE, shown in Figure 2.2 C inlet. The experimental data is fitted with simulated *i-t* behavior for the first order homogeneous electrolysis reaction shown by red open circles.

S1. Kim, J.; Izadyar, A.; Nioradze, N.; Amemiya, S., Nanoscale Mechanism of Molecular Transport through the Nuclear Pore Complex as Studied by Scanning Electrochemical Microscopy, *J. Am. Chem. Soc.*, **2013**, 135, 2321-2329.

S2. Puri, S.R.; Kim, J., Kinetics of Antimicrobial Drug Ion Transfer at a Water/Oil Interface Studied by Nanopipet Voltammetry, *Anal. Chem.*, **2019**, in press.

S3. Karadag, A.; Yang, X.; Ozcelik, B.; Huang, Q., Optimization of Preparation Conditions for Quercetin Nanoemulsions Using Response Surface Methodology, *J. Agric. Food Chem.*, **2013**, *61* , p 2130–2139.

S4. Anton, N.; Vandamme, T.F., The universality of low-energy nano-emulsification, *Int. J. Pharm.*, **2009**, 377, 142–147.

S5. Nishimi, T.; Miller, C.A., Spontaneous emulsification of oil in aerosol-OT/water/hydrocarbon systems, *Langmuir*, **2000,** *16*, 9233-9241

S6. http://www.fuelspec.com/

S7. Cornut, R.; Lefrou, C., "A unified new analytical approximation for negative feedback currents with a microdisk SECM tip", *J. Electroanalytical. Chem.*, **2007**, 608, 59-66.

S8 . Kim, J.; Izadyar, A.; Shen, M.; Ishimatsu, R.; Amemiya, S., "Ion Permeability of the Nuclear Pore Complex and Ion-Induced Macromolecular Permeation as Studied by Scanning Electrochemical and Fluorescence Microscopy", *Anal. Chem.*, **2014**, 86, 2090-2098.

S9 . Kim, B.K.; Boika, A.; Kim, J.; Dick, J.E.; Bard, A.J., Characterizing Emulsions by Observation of Single Droplet Collisions- Attoliter Electrochemical Reactors, *J. Am. Chem. Soc.*, **2014**, 136, 4849-4852.

S10. Bard, A. J.; Faulkner, L. R., "Electrochemical Methods: Fundamental and Applications", 2004, 2nd Ed., John Wiley & Sons INC

APPENDIX 2: CHAPTER 3 SUPPORTING INFORMATION

IN SITU MEASURING PARTITION COEFFICENT AT INTACT NANOEMULSIONS: A NEW APPLICATIONS OF SINGLE ENTITY ELECTROCHEMISTRY

Hiranya Mawadala[1], Shashika Gunathilaka Sabaragamuwe[1], Jiyeon Kim[1]*

[1.] Department of Chemistry, University of Rhode Island, Kingston, RI, 02881

1. Experimental Section

Synthesis of Nanoemulsions.

To prepare NEs, 1.8 mg of KTFPB and 250.0 mg of F127 were dissolved in 3.0 mL of THF in the vial (Fisher Scientific, 8 DR) to form a homogeneous solution. Then, 8.8 μL of DOS was added to this solution. This THF cocktail was mixed for 1 hour using a vortex mixer (Fisher Scientific, Pittsburgh, PA) at a spinning speed of 3000 rpm. After mixing, a 0.1 mL aliquot from this mixed THF cocktail was forcefully injected into 4.0 mL of nanopure water in the vial (Fisher Scientific, 4 DR) during vortex mixing at a spinning speed of 4000 rpm, and then continuously vortex mixed for 2 min. This process was immediately repeated for another batch. The resulting 8 mL of nanopure water containing the THF cocktail was then combined and homogenized (Kinematica AG, Polytron system PT 10-35 GT, Switzerland) for 2 min at a rate of 4900 rpm. In this case, 8 mL is the minimum volume used to suppress froth formation during homogenization (with a 4 DR vial). After homogenization, the meniscus level of the resulting mixture was marked. Then, the solution was further purged with N_2 gas to fully evaporate THF for 1 hour under a flow rate of 40 psi. Finally, the meniscus level of solution was marked again. A volume reduction of roughly 2 mL was observed after the evaporation step. This final solution is a NE stock solution.

Measuring the Size and Zeta potential of Nanoemulsions.

NEs were characterized by carrying out the dynamic light scattering (DLS) experiment to measure the size, size distribution and ζ-potential using Zetasizer instrument (Malvern

Zetasizer Nano ZS, Malvern Instruments Inc., MA). Measurements were taken at 90° angle for the NEs. For the DLS sample preparation, 1.0 mL of NE stock solution was diluted with 3.0 mL of nanopure water, and a 1.0 mL aliquot of this diluted solution was taken to fill a DLS cuvette (Malvern DTS 1070, Malvern Instruments Inc., MA). DLS measurements were obtained using a Malvern Nano ZS at 25 °C.

Fabrication of Pt Ultramicroelectrode (UME) Electrode.

Pt UME (5 μm diameter) was fabricated using the model P-2000 (Sutter Instrument) CO_2- Laser capillary Puller. 25 μm dia. Pt wire (Goodfellow, annealed) was inserted in the borosilicate capillary (I.D. 0.2 mm, O.D. 1 mm, item No 9-000-2000, Drummond scientific company, Broomall, PA) and was pulled together with CO_2 laser puller. As-pulled Pt UME was milled by a homemade polisher to expose Pt disk resulting in an inlaid disk-shaped electrode. Then, the Pt UME was cleaned in piranha solution for 30s. The prepared Pt UME was also used under 30 % or higher relative humidity at 22~23 °C.

TEM measurements with Uranyless negative staining method.

The NEs were visualized with TEM (JEM-2100F, JEOL, MA) at 100 kV. First, specimens were prepared by depositing 3.0 μL of NE suspension on the carbon side of a 300 mesh Cu TEM grid with C/Formvar film (FCF-300, Electron Microscopy Sciences, Hatfield, PA) (NE suspension: 1.0 ml of NE stock sample was diluted with 3.0 ml of nanopure water). After 30 s of NE deposition step, remaining solvent was wicked with filter paper. Then, immediately the grid was immersed in a drop of Uranyless negative stain (Delta Microscopies, France) for 30 s. Uranyless negative stain offers a better contrast on the organic molecules by staining non-radioactive lanthanide mix. The excess stain was wicked using filter paper, and the grid was dried overnight at room temperature and ambient pressure prior to imaging.

2. Characterization of NEs by Dynamic Light Scattering (DLS)

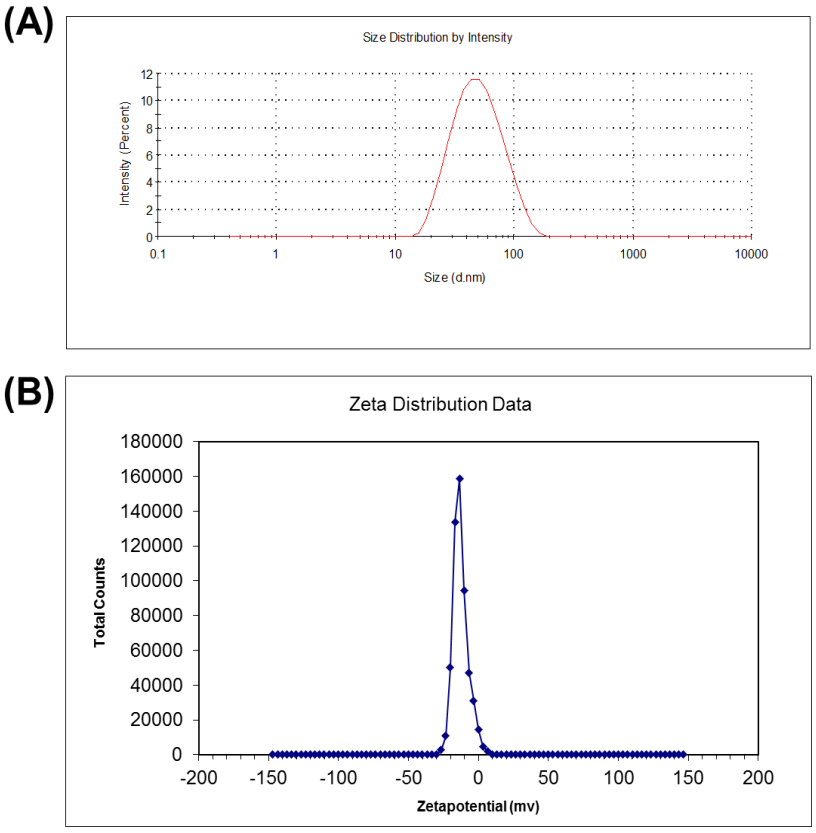

Supplementary Figure 3.1. DLS results of (A) Average diameter, 38 nm with polydispersity index (PDI) 0.15, (B) Average zeta potential, −15 mV.

3. Electrochemistry of 2-ABP in THF Cocktail Solution.

Based on the results in cyclic voltammetry with 2-ABP in THF cocktail solution, 0.85 V vs Pt QRE has been selected to perform the following SEE measurements. Note that 0.85V vs Pt QRE does not trigger the electropolymerization of 2-ABP, thus simplifying the electrochemical oxidation of 2-ABP during SEE measurements.

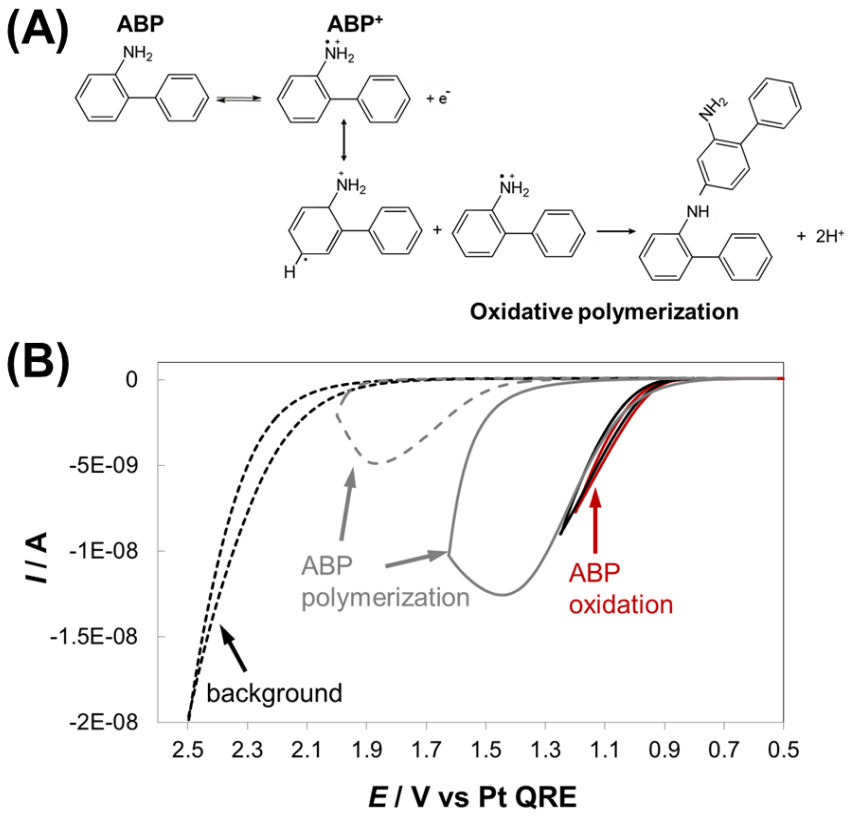

Supplementary Figure 3.2. (A) A mechanistic scheme of electrochemical oxidation of 2-ABP with one electron transfer, which can further undergo electropolymerization reaction. (B) Cyclic voltammograms of 2-ABP in THF cocktail solutions.

4. Fitting *i-t* Decay with Bulk Electrolysis Model.

This collisional response, *i-t* decay was fitted with bulk electrolysis model as below [S1,S2]

$$i(t) = i_p e^{-\frac{mA}{V}t} \quad (1)$$

$$m = \frac{4D_{ABP}}{\pi r_c} \quad (2)$$

where, i_p (= 0.23 pA) is the initial peak current, t is the time (s), m is the mass-transfer coefficient, r_c (=19 pm) and A (= 1.13×10^{-17} cm^2) are a contact radius and area between an UME and a NE, respectively, V (= 2.87×10^{-17} cm^3 for 19 nm radius NE) is a NE volume, and D_{ABP} (= 1×10^{-7} cm^2/s) is the diffusion coefficient of 2-ABP in the castor oil inside a NE determined by Stoke-Einstein equation. In Figure S3.3, we show a good agreement between the experimental *i-t* curve (black solid lines) and the simulation (red open circles), thus validating bulk electrolysis of 2-ABP inside a ~38 nm diameter NE.

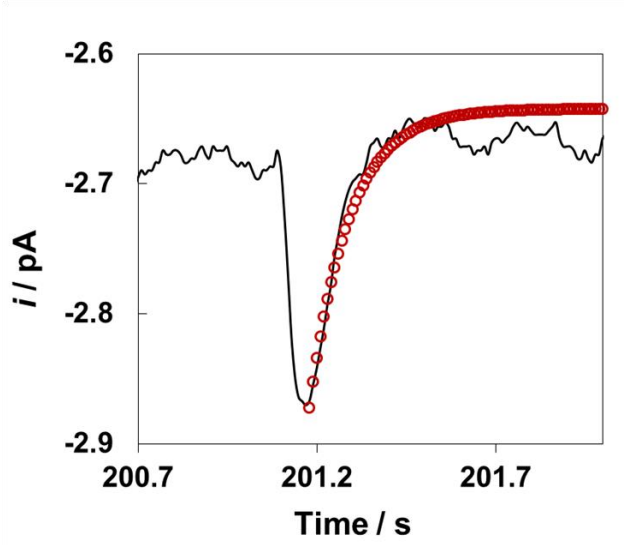

Supplementary Figure 3.3**.** *i-t* curve of a 2-ABP partitioned NE colliding onto Pt UME under 0.85 V vs Pt QRE, shown in Figure 3E inset. The experimental data is fitted with simulated *i-t* behavior for the first order homogeneous electrolysis reaction shown by red open circles.

5. Additional SEE data.

Additional SEE data is shown in Figure S3. With 80 fM NEs in the aqueous solution containing 1 nM ABP, a typical *i-t* curve was observed (Figure S4A). Using the eq (1) and the charges integrated from *i-t* curve, the concentration of 2-ABP in individual NEs was estimated, and the corresponding concentration distribution curve was constructed with a $C_{ABP,\ NE}$ peaked at 1.0 M. Note that the obtained current responses, i.e. the estimated $C_{ABP,\ NE}$ values (= 0.9 (± 0.5) M) are close to the limit of detection in our SEE measurements.

	8 pM NEs	0.8 pM NEs	80 fM NEs
V_{NE} (mL)	1.607×10^{-6}	1.607×10^{-7}	1.607×10^{-8}
V_{aq} (mL)	10.00	10.00	10.00
V_{total} (mL)	$V_{aq} + V_{NE}$	$V_{aq} + V_{NE}$	$V_{aq} + V_{NE}$
slope	6.217×10^{6}	6.169×10^{7}	6.111×10^{8}
P	1.420×10^{10}	7.490×10^{9}	3.480×10^{10}

Table S3.1. Experimental parameters for estimating a partition coefficient, *P*.

6. Molecular Simulation Results.

Quantum chemistry calculations were carried out using Spartan (Wavefunction Inc., Irvine, California, USA, 2014, 1.1.8 version). The molecules of 2-ABP (2-Aminobiphenyl) and DOS (bis(2-ethylhexyl)-sebacate) were built, and combinations of DOS molecules with 2-ABP molecules (model 1, 2, and 3 in Table S2) systems were geometrically equilibrated. Conformer distribution for geometrically equilibrated model 1, 2, and 3 was found using Molecular Mechanics, Merck Molecular Force Field (MMFF) calculation method. The most stable 100 structures were stabilized under Semi Empirical, PM3 method to find the most stable 20 structures with the least energy values. Thermodynamic parameters for DOS, 2-ABP, model 1, 2, and 3 structures were implemented with Hartree-Fock method, and all basis sets and preceding calculations were done with the Slater type functions applied in the Spartan program for both geometry optimization and thermodynamic energy values.

Molecule	$G°$/ kJ/mol	$\Delta G°$/ kJ/mol	β $(\exp(-\Delta G^0/RT))$
2-ABP	-1.336×10^6		
DOS	-3.403×10^6		
model 1 (one 2-ABP + one DOS)	-4.739×10^6	-11.70	1.12×10^2
model 2 (one 2-ABP + three DOS)	-1.155×10^7	-7026	*
model 3 (two 2-ABP + three DOS)	-1.289×10^7	-7555	*

Table S3.2. Calculated energies for models with 2-ABP and DOS molecules (*: too large to be defined).

S1. Kim, B.K.; Boika, A.; Kim, J.; Dick, J.E.; Bard, A.J., Characterizing Emulsions by Observation of Single Droplet Collisions- Attoliter Electrochemical Reactors, *J. Am. Chem. Soc.*, **2014**, 136, 4849-4852.

S2 . Bard, A. J.; Faulkner, L. R., "Electrochemical Methods: Fundamental and Applications", **2004**, 2nd Ed., John Wiley & Sons INC.

APPENDIX 3: CHAPTER 4 SUPPORTING INFORMATION

TOWARDS ULTRALOW DETECTION LIMITS OF AROMATIC TOXICANTS IN WATER USING PLURONIC NANOEMULSIONSAND SINGLE-ENTITY ELECTROCHEMISTRY

Shashika Gunathilaka Sabaragamuwe[1], Hiranya Madawala[1], Surendra Raj Puri[1], Jiyeon Kim[1]*

1. Department of Chemistry, University of Rhode Island, Kingston, RI, 02881

1. Characterization of NEs by Dynamic Light Scattering (DLS).

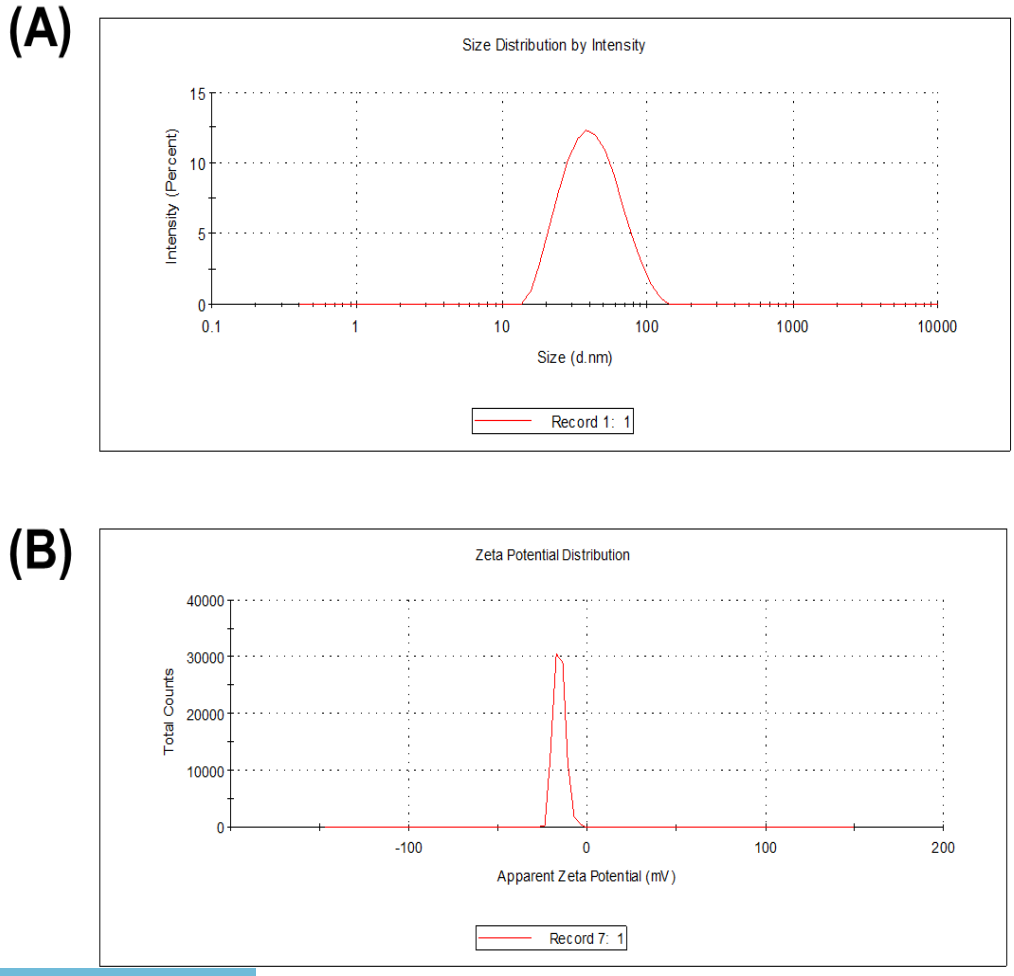

Supplementary Figure 4.1. DLS results of (A) Average diameter, 38 nm with polydispersity index (PDI) 0.17, (B) Average zeta potential, −17 mV.

2. Additional Experimental Data.

	8 pM NEs	0.8 pM NEs	80 fM NEs
V_{NE} (mL)	1.607×10^{-6}	1.607×10^{-7}	1.607×10^{-8}
V_{aq} (mL)	10.00	10.00	10.00
V_{total}(mL)	$V_{aq} + V_{NE}$	$V_{aq} + V_{NE}$	$V_{aq} + V_{NE}$

Table S4.1. Experimental parameters for estimating a partition coefficient, *P*.

3. Fitting *i-t* Decay with Bulk Electrolysis Model.[S1,S2]

$$i(t) = i_p e^{-\frac{mA}{V}t} \quad (1)$$

$$m = \frac{4D_{\mathrm{FcMeOH}}}{\pi r_c} \quad (2)$$

where, i_p (= 0.23 pA) is the initial peak current, t is the time (s), m is the mass-transfer coefficient, r_c (=19 pm) and A (= 1.13×10^{-17} cm^2) are a contact radius and area between an UME and a NE, respectively, V (= 2.87×10^{-17} cm^3 for 19 nm radius NE) is a NE volume, and D_{FcMeOH} (=1×10^{-7} cm^2/s) is the diffusion coefficient of FcMeOH in the castor oil inside a NE determined by Stoke-Einstein equation. In Figure S4.3, we show a good agreement between the experimental *i-t* curve (black solid lines) and the simulation (red open circles), thus validating bulk electrolysis of FcMeOH inside a ~38 nm diameter NE.

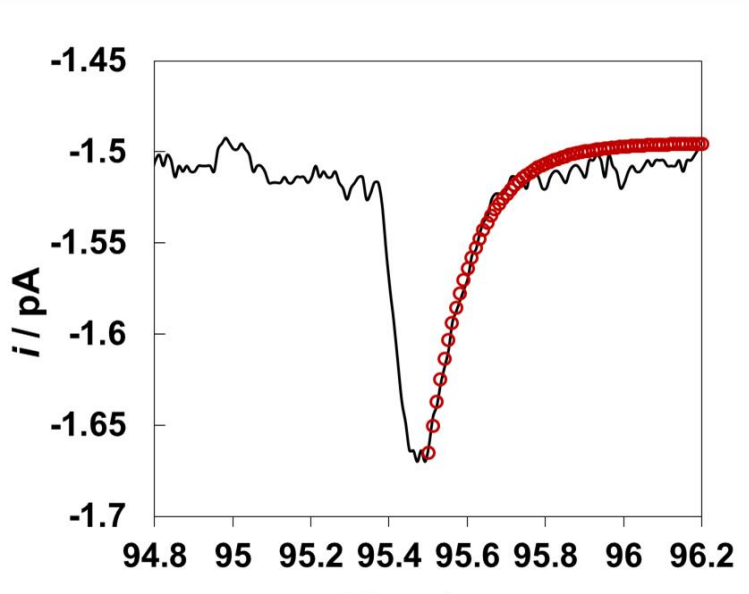

Supplementary Figure 4.2 i-*t* curve of a FcMeOH partitioned NE colliding onto Pt UME under 0.40 V vs Pt QRE, shown in Figure 4.2B inset (II). The experimental data is fitted with simulated *i-t* behavior for the first order homogeneous electrolysis reaction shown by red open circles.

4. Electrochemistry of 2-ABP in THF Cocktail Solution.

Based on the results in cyclic voltammetry with 2-ABP in THF cocktail solution, 0.85 V vs Pt QRE has been selected to perform the following SEE measurements. Note that 0.85V vs Pt QRE does not trigger the electropolymerization of 2-ABP, thus simplifying the electrochemical oxidation of 2-ABP during SEE measurements.

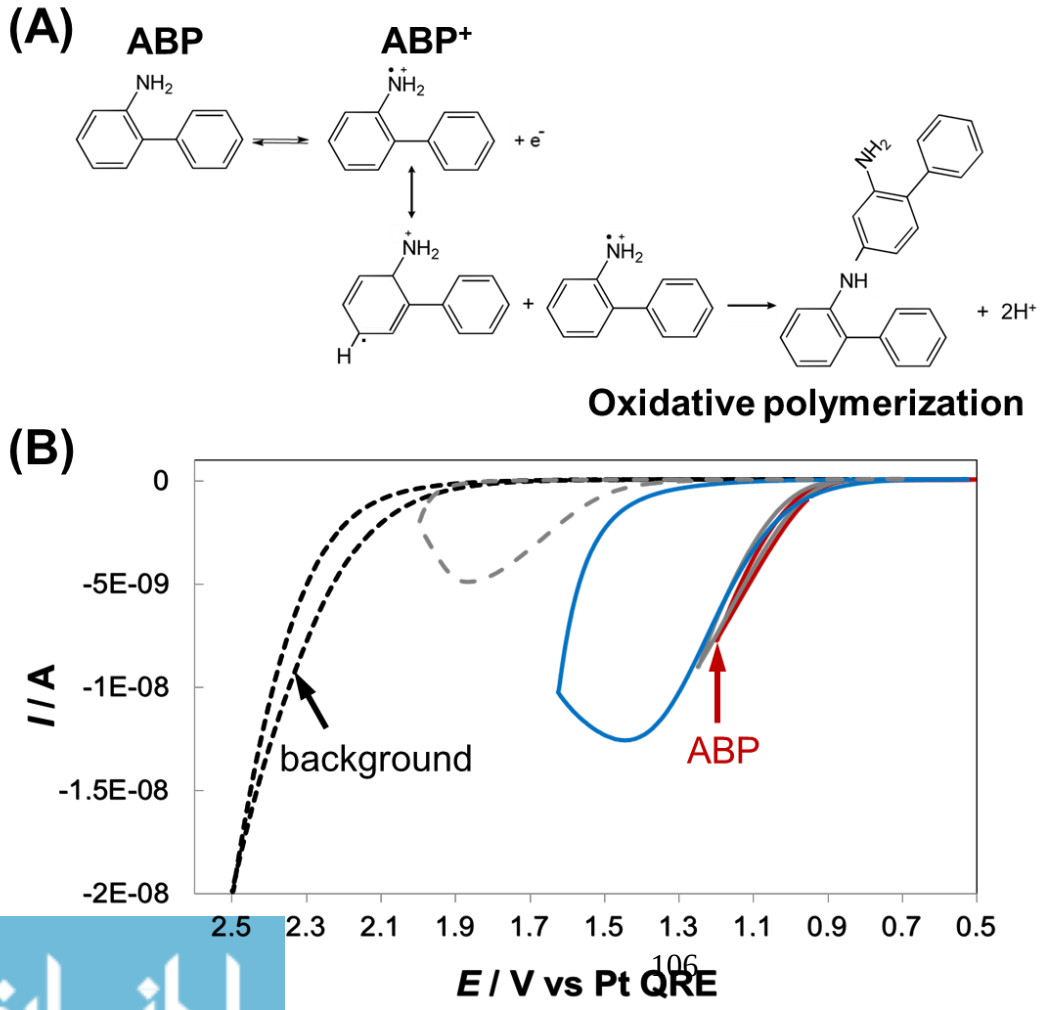

Supplementary Figure 4.3 (A) A mechanistic scheme of electrochemical oxidation of 2-ABP with one electron transfer, which can further undergo electropolymerization reaction. (B) Cyclic voltammograms of 2-ABP in THF cocktail solutions.

5. Calibration Curves for 2-ABP with 8 pM, 0.8 pM, 80 fM NEs.

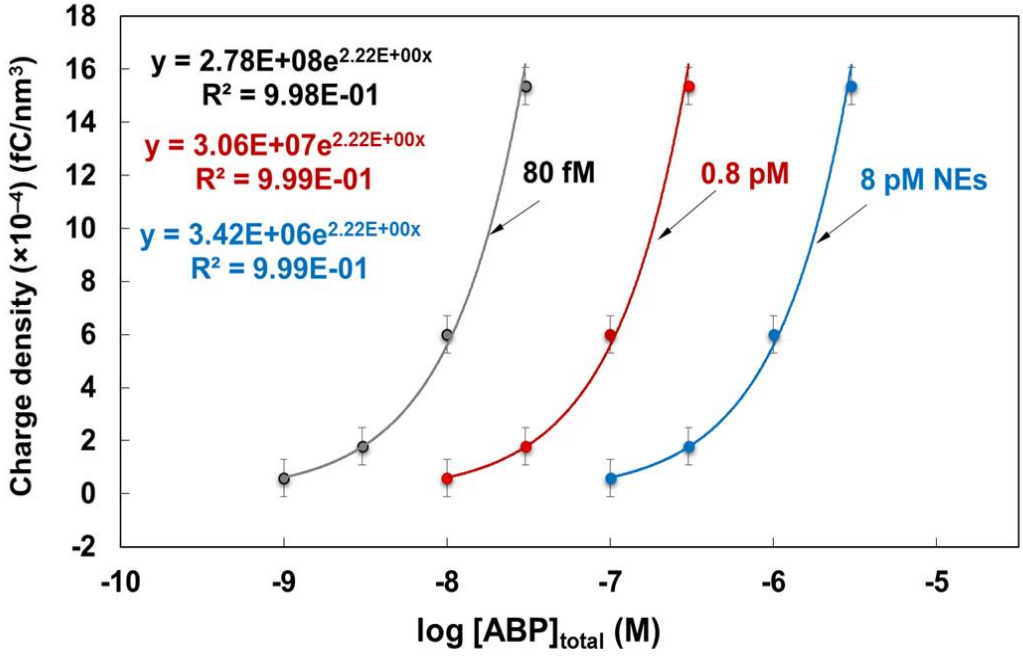

Supplementary Figure 4.4**.** Calibration curves for 2-ABP with 8 pM, 0.8 pM, 80 fM NEs, respectively. Calibration curves are plotted within the dynamic range in Figure 4.5C, where calibration equations are obtained by fitting with exponential functions.

S1. Kim, B.K.; Boika, A.; Kim, J.; Dick, J.E.; Bard, A.J., Characterizing Emulsions by Observation of Single Droplet Collisions- Attoliter Electrochemical Reactors, *J. Am. Chem. Soc.*, **2014**, 136, 4849-4852.
S2. Bard, A. J.; Faulkner, L. R., "Electrochemical Methods: Fundamental and Applications", **2004**, 2nd Ed., John Wiley & Sons INC.